

MODELS AND METHODS FOR BIRD STRIKE LOAD PREDICTIONS

A Dissertation by

Lakshmi S. Nizampatnam

M. S. in Aerospace Engineering, Wichita State University, 1999

Submitted to the Department of Aerospace Engineering
and the faculty of the Graduate School of
Wichita State University
in partial fulfillment of
the requirements for the degree of
Doctor of Philosophy

December 2007

© Copyright 2007 by Lakshmi S. Nizampatnam

All Rights Reserved

MODELS AND METHODS FOR BIRD STRIKE LOAD PREDICTIONS

The following faculty members have examined the final copy of this dissertation for form and content, and recommend that it be accepted in partial fulfillment of the requirement for the degree of Doctor of Philosophy with a major in Aerospace Engineering.

Walter J. Horn, Committee Chair

Klaus Hoffmann, Committee Member

Charles Yang, Committee Member

Jeff Dietiker, Committee Member

Hamid M. Lankarani, Committee Member

Accepted for the College of Engineering

Zulma Toro-Ramos, Dean

Accepted for the Graduate School

Susan K. Kovar, Dean

ACKNOWLEDGEMENTS

I wish to express my deep gratitude and appreciation to my advisor Dr. Walter J. Horn for his enthusiastic supervision, steady encouragement, insight and support throughout the course of this research work. I would like to thank him for his generous time in spite of his busy schedule.

I am also very grateful to Dr. Jeff Dietiker for his encouragement and numerous helpful discussions.

I also wish to thank Dr. Klaus A. Hoffmann, Dr. Charles Yang and Dr. Hamid M. Lankarani for serving on my committee and for accommodating my difficult schedule.

Finally, special thanks and appreciation go to a mentor and friend who offered helpful technical counsel in many discussions, and also provided steady encouragement and motivation.

ABSTRACT

Typical bird shapes used in numerical bird strike analyses include a number of primitive geometries, such as the right circular cylinder, hemi-spherical cylinder, sphere and ellipsoid. There are also some simplifying assumptions made regarding the modeling of the bird material. Yet, the open literature on the subject includes no comparative study to systematically investigate the effect of the projectile shape or bird model material on the accuracy of impact loads analyses. This research filled this gap by showing how various primitive projectile shapes, a more complex bird-like shape, and several homogeneous and heterogeneous material models affect the calculated impact loads. Comparisons to actual bird impact test data were provided, wherever possible, to validate these results.

The bird strike event is characterized by three important phases: shock compression, shock decay, and the establishment of a steady state condition. In addition to reproducing the entire pressure-time history, a rational numerical simulation of bird strike analysis should accurately replicate both the Hugoniot shock pressure and the steady state stagnation pressure. Since the bird is generally represented as a soft body material to model its hydrodynamic behavior, an accurate representation of the bird's equation of state is critical to predicting correct impact loads. In this research, the study of various homogeneous and heterogeneous bird materials depended on the use of accurate equation of state models for each material. Initially, two equations of state – representing the shock compression phase and the steady state compression phase – were studied. This approach follows that of previous research; but, the full 3-D numerical simulation requires a single equation of state to represent the entire impact event. Therefore, an equation of state that combined these two models was derived. Its validity was confirmed by comparing the analytical results from this equation of state with the results from

experimental tests. In addition, the effect of porosity in combination with this equation of state was investigated.

Additionally, the effects of oblique impact and target flexibility on the bird impact loads were investigated using the traditional, homogeneous bird torso model. Both of these factors acted to lower the Hugoniot shock pressures.

The exploration of multi-material bird models in this work began with the study of two different materials, randomly distributed throughout a simple, hemispherical-ended cylindrical bird model. This was followed by introducing high and low density regions in this bird torso model to include the effects of bones and lungs, respectively. Finally, this work studied a more complete, geometrically accurate bird model that included physical shapes and material properties to represent the head, neck, bone structure, lungs, and wings, in addition to the torso. The effect of these multi-material bird models on both the Hugoniot pressure and the steady state pressure is presented in this work.

TABLE OF CONTENTS

Chapter	Page
1. INTRODUCTION.....	1
1.1 Importance of the Bird Strike Problem	1
1.2 Uniqueness of Bird Strike Analysis	1
1.3 Initial Analytical Methods.....	2
1.4 Utility of Finite Element Codes	2
1.5 Bird Models.....	3
1.6 Shedding Light on the Newest Methods for Bird Strike Analysis.....	4
1.7 Contributions of this Work.....	5
1.8 A Brief Overview	7
2. BACKGROUND & LITERATURE REVIEW	9
2.1 Background	9
2.2 Bird Strike Testing	10
2.3 The Bird Strike Problem	12
2.4 The Bird.....	12
2.4.1 Substitute/Synthetic Bird.....	12
2.4.2 Shock Pressure	14
2.4.3 Shock Pressure Decay	15
2.4.4 Steady State Pressure	15
2.5 Numerical Models for Bird and Structure.....	16
2.6 Modeling Techniques.....	16
2.6.1 Target Structural Model	19
2.6.2 Analytical Bird Model.....	19
2.7 Contact/Impact interaction	20
2.8 Literature Review	20
3. GOVERNING EQUATIONS	34
3.1 Conservation of Mass.....	35
3.2 Conservation of Linear Momentum	36
3.2.1 Traction Boundary Condition.....	36
3.2.2 Displacement Boundary Condition	36
3.2.3 Contact Boundary Condition.....	36
3.3 Conservation of Angular Momentum	37
3.4 Conservation of Energy.....	37
3.5 Principle of Virtual Work.....	38
3.6 Finite Element Discretization.....	39

TABLE OF CONTENTS (continued)

Chapter	Page
3.7	Time Integration – Implicit vs. Explicit..... 41
3.7.1	Implicit Time Integration 42
3.7.2	Explicit Time Integration 42
3.8	Solution Strategy..... 43
4.	SPATIAL DISCRETIZATION MODEL FOR BIRD..... 45
4.1	Lagrangian Technique..... 47
4.2	Eulerian Technique 49
4.3	Arbitrary Lagrangian Eulerian (ALE) Technique..... 51
4.4	Smoothed Particle Hydrodynamics (SPH) Technique..... 54
5.	NUMERICAL METHOD..... 58
5.1	Central Difference Scheme for Explicit Time Integration..... 60
5.2	Mass Matrix, M..... 62
5.3	Solution Methodology..... 64
5.4	Strain Rate..... 65
5.4.1	Green Strain Tensor 65
5.4.2	Rate of Deformation Tensor..... 66
5.5	Stress Rate..... 67
5.5.1	Jaumann Rate 67
5.5.2	Treusdell Rate 68
5.5.3	Green-Nagdhi Rate..... 68
5.6	Stress Update..... 69
5.7	Computation of Pressure..... 69
5.8	Artificial Viscosity 73
5.9	Energy Balance 74
5.10	Typical Element Formulation in FEM 74
5.11	Hourglass Modes..... 79
6.	BIRD EQUATION OF STATE MODELS..... 81
6.1	Shock Equation of State 83
6.2	Steady State Equation of State 88
6.3	Impact Event Equation of State..... 90
7.	HOMOGENEOUS BIRD MODELS..... 92
7.1	Effect of Projectile Shape on a Rigid Target..... 94
7.2	Effect of Equation of State Models and Porosity..... 100

TABLE OF CONTENTS (continued)

Chapter	Page
7.3	Effect of Oblique Impact..... 103
7.4	Effect of Target Structure Flexibility..... 108
7.5	Conclusion..... 113
8.	HETEROGENEOUS BIRD MODELS 114
8.1	Randomly Distributed Multi-Material Bird 116
8.2	Multi-Material Bird with Lumps of High Density and Low Density Materials..... 117
8.3	Multi-Material Bird with a Realistic Bird Shape 121
8.3.1	Effect of Increasing the Density of Head and Neck Material 125
8.3.2	Effect of Increasing the Density of Bone Structure Material..... 130
8.3.3	Effect of Increasing the Density of Torso Material..... 133
8.3.4	Effect of Increasing the Density of Head and Neck Material on the Deformation of the Target..... 136
8.4	Conclusion..... 142
9.	CONCLUSIONS AND SUGGESTIONS FOR FUTURE WORK 144
9.1	Conclusions 145
9.2	Suggestions for Future Work 146
	LIST OF REFERENCES 148

LIST OF TABLES

Table	Page
2.1. Bird Strike Test Requirements	12

LIST OF FIGURES

Figure	Page
3.1. Undeformed (initial) and deformed (current) configurations of a body	35
3.2. Explicit time integration loop in LS-Dyna	44
4.1. Lagrangian description.....	47
4.2. Non-physical negative volume for an element of unit thickness	48
4.3. Eulerian description.....	50
4.4. Arbitrary Lagrangian Eulerian (ALE) description	52
4.5. Particle neighborhood for SPH particle, k	55
5.1. 8-Node Hexahedron element.....	75
5.2. Hourglass modes for a 2-D quadrilateral element.....	80
6.1. Variation of Hugoniot pressure with impact velocity for water.....	85
6.2. Effect of porosity on shock velocity	89
6.3. Effect of porosity on shock pressure	89
6.4. Pressure-volume relationship computed from shock equation of state.....	91
6.5. Pressure-volume relationship computed from steady state equation of state.....	91
7.1. Longitudinal-sectional particle geometry for numerical models of various projectile shapes a) Hemi-spherical cylinder, b) Right circular cylinder, c) Sphere and d) Ellipsoid	96
7.2. Instantaneous particle displacements for a cylindrical projectile at different times during impact with a rigid flat plate a) 0.0009 s, b) 0.0012 s, c) 0.0015 s and d) 0.0018 s.....	97
7.3. Instantaneous particle displacements for a spherical projectile at different times during impact with a rigid flat plate a) 0.0011 s, b) 0.0013 s, c) 0.0015 s and d) 0.0017 s.....	97
7.4. Instantaneous particle displacements for an ellipsoid projectile at different times during impact with a rigid flat plate a) 0.0006 s, b) 0.0009 s, c) 0.0012 s and d) 0.0015 s.....	98

LIST OF FIGURES (continued)

Figure	Page
7.5. Instantaneous particle displacements of a hemi-spherical projectile at different times during impact with a rigid flat plate a) 0.00068 s, b) 0.00096 s c) 0.00116 s and d) 0.00144 s	98
7.6. Effect of projectile shape on shock pressure for $z = 0.4$	99
7.7. Effect of projectile shape on steady state pressure for $z = 0.4$	99
7.8. Comparison of shock pressures a) Hugoniot or Shock equation of state, b) Isentropic equation of state, c) Impact event equation of state	104
7.9. Comparison of stagnation pressures a) Hugoniot or Shock equation of state, b) Isentropic equation of state, c) Impact event equation of state.....	105
7.10. Instantaneous particle displacements for impact obliquity of 45 degrees at different times during impact with a rigid flat plate a) 0.0 s, b) 0.0008 s, c) 0.00096 s, d) 0.0012 s and e) 0.00142 s	107
7.11. Instantaneous particle displacements for impact obliquity of 25 degrees at different times during impact with a rigid flat plate a) 0.0 s, b) 0.00068 s, c) 0.0012 s, d) 0.0013 s and e) 0.00168 s	107
7.12. Comparison of shock pressures for impact angle of 45 degrees	109
7.13. Comparison of shock pressures for impact angle of 25 degrees	109
7.14. Instantaneous particle displacements for normal impact at different times during impact with a flexible flat plate of thickness 1 mm a) 0.00052 s, b) 0.0006 s, c) 0.0008 s, d) 0.001 s, e) 0.0012 s, f) 0.0014 s, g) 0.0016 s, h) 0.0018 s, i) 0.002 s, j) 0.0024 s, k) 0.0028 s and l) 0.0032 s	111
7.15. Instantaneous particle displacements for normal impact at different times during impact with a flexible flat plate of thickness 5 mm a) 0.00052 s, b) 0.0006 s, c) 0.0008 s, d) 0.001 s, e) 0.0012 s, f) 0.0014 s, g) 0.0016 s, h) 0.0018 s, i) 0.002 s, j) 0.0024 s, k) 0.0028 s and l) 0.0032 s	112
8.1. Instantaneous particle displacements for a randomly distributed multi-material projectile ($z = 0.2$ & $z = 0.3$) at different times during impact with a rigid flat plate a) 0.0 s, b) 0.00075 s, c) 0.00116 s, d) 0.00152 s, e) 0.002 s and f) 0.00255 s.....	118

LIST OF FIGURES (continued)

Figure	Page
8.2. Instantaneous particle displacements for a randomly distributed multi-material projectile ($z = 0.4$ & $z = 0.3$) at different times during impact with a rigid flat plate a) 0.0 s, b) 0.00075 s, c) 0.00116 s, d) 0.00152 s, e) 0.002 s and f) 0.00255 s.....	119
8.3. Comparison of shock pressures of multi-material birds of random distribution of two distinct materials within the bird torso with respect to Wilbeck's experimental tests and theory.....	120
8.4. Multi-material bird model with high density lumps for bones and low density lumps for lungs	120
8.5. Instantaneous particle displacements for a multi-material projectile with high density and low density lumps at different times during impact with a rigid flat plate a) 0.0 s, b) 0.0009 s, c) 0.00126 s, d) 0.00186 s, e) 0.00186 s (cross-sectional view) and f) 0.00271 s.....	122
8.6. Comparison of shock pressures for multi-material birds with high density lumps for bone structure and low density lumps for soft tissue and lungs ($z = 0.8$) within the bird torso ($z = 0.6$)	123
8.7. Multi-material bird model with a realistic bird shape.....	123
8.8. Instantaneous particle displacements for a multi-material projectile at different times during impact with a rigid flat plate a) 0.0 s, b) 0.0009 s, c) 0.00133 s and d) 0.00182 s.....	126
8.9. Instantaneous particle displacements for a multi-material projectile at different times during impact with a rigid flat plate (continued from Figure 8.8) a) 0.0022 s, b) 0.0025 s, c) 0.0031 s and d) 0.0035 s.....	127
8.10. Time history of maximum pressure for the multi-material bird with 30% porosity ($z = 0.3$) for the head and neck material.....	128
8.11. Time history of maximum pressure for the multi-material bird with 10% porosity ($z = 0.1$) for the head and neck material.....	128
8.12. Time history of maximum pressure for the multi-material bird with no porosity ($z = 0.0$) for the head and neck material	129
8.13. Comparison of maximum pressures generated from the impact of various parts of the three multi-material bird models.....	129

LIST OF FIGURES (continued)

Figure	Page
8.14. Time history of maximum pressure for the multi-material bird with 10% porosity ($z = 0.1$) for the bone material.....	131
8.15. Time history of maximum pressure for the multi-material bird with no porosity ($z = 0.0$) for the bone material	132
8.16. Effect of an increase of the density of the bone material on the maximum pressures generated from the impact of various parts for the three multi-material bird models	132
8.17. Time history of maximum pressure for the multi-material bird with 50% porosity ($z = 0.5$) for the torso material.....	134
8.18. Time history of maximum pressure for the multi-material bird with 40% porosity ($z = 0.4$) for the torso material.....	135
8.19. Effect of an increase in the density of the torso material on the maximum pressures generated from the impact of the bird torso for the three multi-material bird models investigated.....	135
8.20. Instantaneous particle displacements for a multi-material projectile with $z = 0.3$ for the head and neck, at different times during impact with a flexible flat plate a) 0.0 s, b) 0.0008 s, c) 0.0013 s and d) 0.002 s.....	138
8.21. Instantaneous particle displacements for a multi-material projectile with $z = 0.3$ for the head and neck, at different times during impact with a flexible flat plate (continued from Figure 8.20) a) 0.024 s, b) 0.00287 s, c) 0.0032 s and d) 0.0037 s	139
8.22. Instantaneous particle displacements for a multi-material projectile with $z = 0.0$ for the head and neck, at different times during impact with a flexible flat plate a) 0.0 s, b) 0.00078 s, c) 0.00134 s and d) 0.00199 s.....	140
8.23. Instantaneous particle displacements for a multi-material projectile with $z = 0.0$ for the head and neck, at different times during impact with a flexible flat plate (continued from Figure 8.22) a) 0.0024 s, b) 0.00287 s, c) 0.0032 s and d) 0.00371 s	141
8.24. Effect of an increase of the density of the head and neck material on target deflection for the multi-material bird.....	142

LIST OF ABBREVIATIONS / NOMENCLATURE

<u>Abbreviation</u>	<u>Definition</u>
1-D	One-Dimensional
2-D	Two- Dimensional
3-D	Three- Dimensional
ALE	Arbitrary Lagrangian Eulerian
BC	Boundary Condition
CFD	Computational Fluid Dynamics
CFL	Courant-Friedricks-Lewy
CPU	Central Processing Unit
DOF	Degree of Freedom
EOS	Equation of State
FAA	Federal Aviation Administration
FAR	Federal Aviation Regulations
FEM	Finite Element Method/Model
NM	Nodal Masses
psi	Pounds per Square Inch
SPH	Smoothed Particle Hydrodynamics

LIST OF SYMBOLS

<u>Symbol</u>	<u>Definition</u>
A	Area
\mathbf{B}, B_{ij}	Strain displacement matrix
\mathbf{C}, C_{ijkl}	Material tangent modulus tensor
\mathbf{D}, D_{ij}	Rate of deformation tensor
\mathbf{E}, E_{ij}	Green or Green-Lagrangian strain tensor
E	Total internal energy
\mathbf{F}, F_i	Nodal force vector
\mathbf{F}, F_{ij}	Deformation gradient tensor
I	Impulse
J	Determinant of Jacobian between spatial and material coordinates
\mathbf{L}, L_{ij}	Velocity gradient tensor
L	Length of the bird
\mathbf{M}	Mass matrix
N_I	Interpolation function
N	Total number of elements in the computational domain
\mathbf{Q}, Q_{ij}	Transformation matrix
\mathbf{R}, R_{ij}	Orthogonal rotational matrix
R	Gas constant

LIST OF SYMBOLS (continued)

<u>Symbol</u>	<u>Definition</u>
\mathbf{S}, S_{ij}	Second Piola-Kirchhoff stress tensor
T	Duration of impact
\mathbf{U}, U_{ij}	Right stretch tensor
V	Volume
\mathbf{W}, W_{ij}	Vorticity or spin tensor
W	Interpolating kernel
X_1, X_2, X_3	Cartesian coordinates in the reference configuration
\mathbf{a}, a_i	Acceleration vector
\mathbf{b}, b_i	Body force vector
c_o	Isentropic wave velocity
\mathbf{d}, d_i	Displacement vector
e	Specific internal energy
\dot{f}	Material time derivative of a field variable, f
$f_{,x}$	Spatial derivative of a field variable, f with respect to independent spatial variable, x
h	Smoothing length
m	Mass
\mathbf{n}, n_i	Unit normal vector
n	Number of Gauss integration points domain
p	Pressure

LIST OF SYMBOLS (continued)

<u>Symbol</u>	<u>Definition</u>
p_c	Pressure at the center of the impact zone
p_H	Hugoniot pressure / shock pressure
q	Shock viscosity
r	Radial distance from the center of the impact region
\mathbf{s}, s_{ij}	Component of deviatoric stress tensor
\mathbf{t}, t_i	Traction vector
t	Time
\mathbf{v}, v_i	Velocity vector
$\dot{\mathbf{v}}, \dot{v}_i$	Acceleration vector
v_s	Velocity of shock
w	Velocity of the reference domain in the ALE formulation
x_1, x_2, x_3	Cartesian coordinates in the current configuration
z	Amount of porosity
Γ	Boundary of the domain
$\boldsymbol{\Omega}, \Omega_i$	Angular velocity vector
δ_{ij}	Kronecker delta
$\delta\pi$	Virtual work
$\dot{\boldsymbol{\epsilon}}, \dot{\epsilon}_{ij}$	Strain rate tensor
γ	Ratio of specific heats for air

LIST OF SYMBOLS (continued)

<u>Symbol</u>	<u>Definition</u>
ν	Non-dimensional length
ν	Poisson's ratio
ρ	Density
σ, σ_{ij}	Cauchy stress tensor
$\sigma^{\nabla G}$	Green-Nagdhi rate of Cauchy stress tensor
$\sigma^{\nabla J}$	Jaumann rate of Cauchy stress tensor
$\sigma^{\nabla T}$	Treusdell rate of Cauchy stress tensor
ω	Highest natural frequency of the computational domain
ξ, η, ζ	Isoparametric coordinates
<u>Subscript/Superscript</u>	<u>Definition</u>
0	Initial state
1	Condition ahead of shock
2	Condition behind shock
C	Consistent
H	Hugoniot
P	Projectile
S	Shock
T	Target
d	Deviatoric component

LIST OF SYMBOLS (continued)

<u>Subscript/Superscript</u>	<u>Definition</u>
ext	External
i	Instantaneous
int	Internal
m	Mean component
r	Radial
s	Shock
s	Steady state
α, β	Contact surfaces

CHAPTER 1

INTRODUCTION

1.1 Importance of the Bird Strike Problem

A bird strike incident is one of the most dangerous threats to flight safety, and it can have tragic consequences, especially for small general aviation airplanes. Though rarely catastrophic, bird strikes cause significant economic loss for all aviation, estimated at over \$1 billion worldwide every year [1]. FAA airworthiness regulations require that an aircraft be designed to successfully complete a flight after an impact with a standard-size bird. These standards/regulations ensure that aircraft designers bird-proof the forward-facing components of the aircraft – such as windshields and windows, aircraft engines and leading edge structures – before the aircraft is certified for flight.

The common method of bird-proofing a new airplane design is to build and test, then redesign and test again. After the successful test of a prototype according to certification requirements, further testing with higher impact velocities is often carried out to determine the actual limits of the structure. Achieving a low-weight, bird-proof design may require several extensive and difficult experimental iterations of the test structure. Consequently, numerical techniques in tandem with computer modeling have become irreplaceable design tools in the development of lightweight bird-proof structures on tight development schedules and reasonable budgets.

1.2 Uniqueness of Bird Strike Analysis

A bird strike event is characterized by loads of high intensity and short duration. The duration of the forcing function for bird impact loading is typically in the range of milli-seconds. During impact, both the airplane structure (target) and the bird (projectile) undergo high,

inelastic strain rates and large deformations. A complex interaction exists between the impact energy and deformation of the bird and the resulting response of the structure. It is important to account for this strong, dynamic coupling between the bird and structure. In addition, a bird strike event can involve multiple impacts of the bird. For example, after striking a wing leading edge or engine inlet, the bird could penetrate the structure and strike internal structural components, such as a wing spar or a fuselage bulkhead.

1.3 Initial Analytical Methods

Bird strike simulation is inherently complex due to the number of variables involved, which include material characteristics of the bird, bird size (weight), bird velocity, bird orientation, and high strain rates of the materials, as well as the interaction between the dynamic loads at impact and the structural response. Much work has been carried out to analyze the response of both the bird and the target structure during impact. Early work used force-impulse models and semi-empirical equations to simulate the overall impact force during a bird-strike event. Although these early methods are often based on momentum conservation, they fail to account for the complex structural interaction that occurs between the bird and the target. In most cases, these simple force-impulse models cannot predict the details affecting the level of local damage imposed on a target.

1.4 Utility of Finite Element Codes

Finite element codes have the capability to accurately represent the complex geometry of the impacted structure and the bird, as well as the transient loading of a bird impact event. Nonlinearity should be included in the analytical model due to the presence of high strain rates, large deformations, and inelastic strains. In addition, the analysis should have the capability to include subsequent penetration of the bird inside the airframe following the initial hit.

Several commercial, nonlinear explicit codes based on FEM (Finite Element Method) are currently available to develop efficient (low weight), bird-proof structures. Currently, highly detailed models of the bird and the target structure can be built using a variety of spatial discretization modeling approaches; and the simulations may be performed using various solution strategies, including a pure Lagrangian, pure Eulerian, Arbitrary Lagrangian Eulerian (ALE), and Smooth Particle Hydrodynamics (SPH) approaches. Each of these numerical techniques has relative advantages and disadvantages.

1.5 Bird Models

A very important part of bird strike analysis is choosing the appropriate numerical model of the bird. Included in this modeling exercise is the selection of the shape and material of the bird. The shape generally varies between the following primitive geometries: right circular cylinder, hemi-spherical cylinder and ellipsoid [2-4]. Extensive experimental tests conducted by Wilbeck and Rand [5] concluded that a bird behaves essentially like a fluid upon impact, thus spreading the impact load. In addition, these experimental studies, carried out with a range of bird sizes (weight), showed that there are two principal components of the bird impact loading: the characteristic Hugoniot or shock pressure pulse, and the steady state pressure. Therefore, any numerical simulation should include both of these components in the prediction of impact loads. However, due to the lack of modeling capabilities, early numerical work ignored the effects of the Hugoniot pressure. With the current state-of-the-art in numerical simulation, numerical models are now able to predict both the Hugoniot and the steady state pressures in a single simulation.

Due to the non-homogeneity of the bird material, researchers were faced with the difficulty of non-repeatable test results. This led to an effort to find a substitute homogenous

bird material that can simulate the bird impact behavior and produce impact loads much like a real bird. It had been found that bird projectile response depends on material density and not on material strength. Several experimental studies were conducted with wax, foam, emulsions, and gelatin as substitute materials for birds. The conclusions from these studies indicated that soft material substitutes that have the specific gravity of water produced loading profiles that were very similar to that of birds. Gelatin, with the specific gravity of water, closely reproduced the behavior of a real bird; thus, gelatin is one of the extensively used substitute bird materials in both experimental tests and in numerical simulations. It should be noted that while substitute birds can be used for developmental work, they cannot be used for certification tests.

Recently, attempts were made by McCallum and Constantinou [6] to model the bird with physical dimensions equivalent to the Canadian goose. Analyses with this new bird model indicated that the target surface may get pre-stressed from the initial impact of the head and neck, prior to the impact of the torso, which may have significant consequence on the initiation of target failure. Though their results were not complete, this multi-material bird study indicated that inclusion of the long neck and head, along with the torso, might be a necessary feature for accurately predicting the impact load profiles and subsequent damage resulting from impacts with large birds.

1.6 Shedding Light on the Newest Methods for Bird Strike Analysis

In spite of the availability of a wide variety of commercial numerical codes for bird strike simulation, there is little publicly accessible information on their underlying numerical methods. The reason is that most of the current generation of commercial codes were initially developed in U.S. defense laboratories. Consequently, any published reports on the numerical methods are in the form of restricted reports at government labs, mostly inaccessible to the general public.

While many of the developers of these codes have gone on to develop commercial codes, the commercial codes have proprietary restrictions. As a result, these codes are being used with little or no practical understanding of their analytical or numerical limitations.

In 1991, Benson [7] published a detailed review of the general methods for Lagrangian and Eulerian hydrocodes, thereby shedding the first public light on the basis for the methods used in commercial codes for impact analyses. However, Benson's work remains obscure due to the arcane terminology. Consequently, even though these methods are understood by a small group of software developers, they still appear to be entirely unknown to the user community.

1.7 Contributions of this Work

An extensive bird strike literature survey by the author produced no published work that explained the utility and limitations of hydrocode analysis methods as they apply to bird strike events. In the current work, an effort was made to bridge this consequential gap by including a detailed summary of the hydrocode methods used in bird strike analysis.

Typical bird shapes used in numerical analyses vary among several primitive geometries, as mentioned before. An extensive literature review did not uncover any comparative study that systematically investigated the effect of the projectile shape on the impact loads generated. This work filled this need by providing a comparative analysis of common projectile shapes on the impact loads.

A bird is described as a "soft body" material because the stresses generated during a bird strike are well beyond the strength of the bird, but are generally below the strength of the target material. Since the bird behaves like a fluid upon impact, the impact loads can be computed from an equation of state if the viscosity is neglected. Using the appropriate equation of state is critical to predicting accurate impact loads. Wilbeck [8], in his one-dimensional hydrodynamic

theory for bird impact analysis, proposed independent equations of state for the shock phase and for the steady state phase. The validity of these independent equations of state for simulating the full impact event was investigated. In addition, an equation of state was derived for use in the three-dimensional numerical analysis that serves all phases of an impact event. Its validity for predicting bird impact loads was confirmed through comparative analysis with the previously mentioned equations of state as well as with the available experimental results.

A substitute bird material that is very popular with researchers consists of a homogeneous mixture of 90% water and 10% air. However, an analytical material with just 10% porosity substantially over-estimates the Hugoniot pressures compared to those obtained from experimental results with real birds. It was thought that increasing the material porosity might provide a more accurate estimate of the Hugoniot pressures. Therefore, in this work the effect of porosity of the bird material on impact loads was investigated, and a more suitable porosity of 30% - 40% is recommended.

In the above work, the bird model was based on a traditional, homogeneous bird torso; and the impact path was perpendicular to a rigid target. The effects of both impact obliquity and target flexibility were briefly examined, as well. As expected, these factors lowered the magnitude of the Hugoniot pressures.

McCallum and Constantinou [6] published an important work that is the only published effort to examine the effects of a more complex multi-material model. However, they used the same equation of state to represent all the different materials in their multi-material bird, and that equation of state was not appropriate for soft body materials. Consequently, their results did not produce the characteristic, sharp Hugoniot peak in their analytical pressure history plots.

In this research, the use of more rigorous multi-material bird models for predicting bird impact loads was investigated. Three types of models were investigated to explore the effects of heterogeneous material models for a bird. First, a bird model was built with two discrete materials having different densities and equations of state. These two materials were randomly distributed throughout the bird torso. A second bird model was investigated that has a torso made up of three fully separate constituents – a traditional “bird” material consisting of a homogeneous mixture of water and air, high density lumps to represent the main bone structure, and low density lumps to represent soft tissue and lungs. Finally, a third multi-material bird model was created that had a more realistic bird shape. It had the characteristic features of a real bird, such as head, neck, torso, bones, lungs and wings. The material properties of the various parts of this multi-material model are distinct in that each has its own density value (different from the other materials) and an associated equation of state.

1.8 A Brief Overview

Chapter 2 provides an extensive summary of the research work in the field of bird strike analysis. This review includes bird models that range in sophistication from simple force-impulse models, based on empirical equations, to highly complex, 3-dimensional bird models. Chapter 3 presents the fully 3-dimensional governing equations for bird strike impact analysis, and a brief review of time-marching techniques. Chapter 4 presents various spatial discretization modeling options for the numerical bird. A brief theoretical review is presented for the following four techniques: pure Lagrangian, pure Eulerian, Arbitrary Lagrangian Eulerian (ALE), and Smooth Particle Hydrodynamics (SPH).

The SPH approach is chosen for the bird model because, unlike the other modeling methods, the SPH method is free from the numerical difficulties associated with the large

deformations inherent to the problem of bird strikes. Thus, a detailed summary of the SPH equations is also provided. Chapter 5 presents the mathematical details of the underlying numerical method. Chapter 6 includes the derivations of the bird material equation of state models. Chapter 7 presents the results from the homogeneous bird models. Chapter 8 presents the results from the heterogeneous bird models. Chapter 9 presents the conclusions of this work and suggestions for future research in the field of bird strike analysis.

CHAPTER 2

BACKGROUND & LITERATURE REVIEW

2.1 Background

Many external airframe components are susceptible to collisions with birds, particularly during the critical takeoff and landing phases. In order to assure minimum safety standards in cases of bird impacts, international airworthiness standards require that airplane tests be conducted to demonstrate certain basic capabilities specified in terms of structural resistance and allowable degradation in flying qualities.

The size of the birds used for testing is set forth by the certification authorities. Different weight birds are specified for windshields, wings, empennage, and engines. The standards for the leading edge of a flying surface dictate that the bird should not cause critical structural damage to the load-carrying structural members directly interior to the leading edge skin. The airworthiness standards for the windshields of a business jet require that the windshield transparencies and frames be capable of sustaining the impact of a 4 lb bird at maximum cruise velocity (typically 250 knots – the maximum permitted airspeed below 10,000 ft), with no serious penetration. Jet engine certification requires the demonstration of maintaining a certain level of thrust after an encounter with a flock of small birds, or the safe shut down of an engine after ingesting a single large bird.

One might marvel that birds are able to know which part of an airplane to strike, depending on their weight. The answer, of course, is that no other part of aircraft regulations so clearly shows the basic nature of safety regulations – that they are based primarily on what is technically achievable by the existing state-of-the-art. While flying surfaces can survive an 8 lb bird impact with relatively little weight penalty, a windshield thick enough to withstand an 8 lb

bird would be excessively heavy and have unacceptable optical characteristics. Consequently, 4 lb birds are used for windshield requirements, and the resulting level of safety has been satisfactory.

The final designs and acceptance of bird resistant components are typically dependent on testing. Analyses are permitted without verification tests in occasional instances where structure very similar to the current structure that is being certified has been cleared through tests. Therefore, the typical method of bird-proofing an airplane is to build and test, then redesign and test again.

2.2 Bird Strike Testing

Bird strike tests are done in accordance with FAR Parts 25 and 33, as shown in Table 2.1. These tests once involved the shooting of a live chicken of appropriate weight at the article to be certified. It is easy to imagine that the cleanup effort following each test was substantial. For simplicity, sanitary, aesthetic, and repeatability reasons, it is now permitted to use cleaned and dressed chickens instead of live birds.

A bird-cannon is used to shoot the chicken at the target structure. The cannon is a tube, usually 5 -10 inches in diameter, connected to a large compressed air source. High air pressures are not needed, since even 40 psi, for example, will accelerate the bird to several hundred meters per second in a very short distance. Inside the cannon, the bird is loosely placed in a cylindrical, open-ended carrier, called a “sabot,” that conforms to the shape of the tube and acts as a seal. The lightweight sabot greatly improves repeatability of the output speeds. It separates from the bird before impact.

A typical windshield test program involves several bird shots at various points on each windshield and frame. The goal is to show that pilots will not be injured by the bird, windshield

fragments, or broken airframe or interior parts; and that the damaged structure and windshield will continue to hold cabin pressure following a bird strike event. High speed cameras (10,000 – 20,000 frames per second) are placed inside and outside the cockpit to capture the details of any failure. At actual playback speeds, the outside video of a successful bird shot shows nothing but sabot fragments fluttering down and some condensation vapor emanating from the cannon. At slow playback speeds, the replay shows the fluid behavior of the bird, high local deflections of the windshield, and rather large amplitude impact waves and reflections rippling throughout the forward fuselage.

Wing shots are targeted at inboard and outboard leading edges. The typical goal is to show that the bird does not penetrate the main load-carrying spars and no fuel cells are damaged so as to cause fuel leakage. Splitter plates (in the form of a span-wise triangular box) are often placed inside the leading edge skins to deflect the bird and reinforce the leading edge structure.

Empennage shots are targeted at several span-wise locations along the leading edges of the vertical fin and stabilizer, where vulnerabilities resulting from impact damage are expected to be the highest. The typical goal of these tests is to show that the bird does not penetrate the main load-carrying spars. Similar to wing leading edges, the empennage leading edges often contain splitter plates inside the skins to deflect the bird and to reinforce the leading edge structure.

Engine bird strike tests include the investigation of the damage effects on engine operations as well as on fan disk integrity. Engine operation tests must show that the engine will continue to produce at least 75% thrust for 5 minutes after ingesting a flock of small or medium weight birds, as shown in Table 2.1. Fan integrity tests must demonstrate that the engine does not catch fire or disintegrate after being struck by a single, 4 lb bird.

Table 2.1

Bird Strike Test Requirements

Aircraft Component	Bird Weight	FAR Section
Windshields and Frames	4 lb	25.775 (b), 25.775 (c)
Wing Leading Edges	4 lb	25.571(e)(1)
Empennage Leading Edges	8 lb	25.631, 25.571(e)(1)
Engine – Inlet Lip	4 lb	25.571(e)(1)
Engine – Fan Integrity	4 lb	33.77, 25.571(e)(1)
Engine – Continued Operation	Up to 16 of 3 oz birds	33.77, 25.571(e)(1)
	Up to 8 of 1.5 lb birds	

These experimental proof tests are expensive, and are often difficult to perform with the necessary accuracy and repeatability. The build and test procedures are quite expensive due to the high tooling cost associated with each design iteration until the tests are successfully completed. These costs, as well as the aggressive requirements to reduce design cycle time while minimizing the structural weight, make the possibilities of bird strike design and certification through analysis alone a very attractive proposition. Improved design methodologies, based on better analytical simulation procedures, will result in significantly shorter design cycles, and a reduced number of expensive, experimental proof tests.

2.3 The Bird Strike Problem

The bird strike problem includes three principal elements – the bird, the structure, and their dynamic impact interaction.

2.4 The Bird

2.4.1 Substitute/Synthetic Bird

The main technical limitation to using real birds in tests is the issue of repeatability of results, primarily due to the non-homogeneity of bird material. This non-repeatability makes it very challenging to validate test results. Various researchers have studied wax, foam, emulsions

and gelatin as the material for a substitute bird. Artificial birds cannot be used for certification tests, but can be used for design and development. Wilbeck and Rand [5] conducted a very comprehensive testing program to develop a substitute, synthetic bird model, and their results will be discussed at a later point in this chapter.

Any substitute bird model should be capable of replicating the load-time history of an actual bird impact event. Projectile impact behaviors can be categorized as a function of increasing impact speed as follows: elastic, plastic, hydrodynamic, sonic, or explosive [9]. Of these, hydrodynamic behavior is considered to be most representative of bird impact, as described below.

At typical bird impact velocities, a bird behaves as a “soft body” because its internal stresses greatly exceed its material ultimate strength, but are well below the target material ultimate strength. For these reasons, the bird impact process has been successfully modeled by hydrodynamic theory [9,10,11]. Peterson and Barber [12] concluded that birds essentially behave like a fluid during an impact; birds do not bounce; and impact duration is approximately that of the bird “squash-up” time. The “squash-up” time is given by

$$T = \frac{L}{v_0} \quad (2.1)$$

where T is the duration of impact (squash-up time), L is the length of the bird, and v_0 is the initial impact velocity. In these impact events, the bird mass and material density, and not its material strength, determine the projectile response.

The three stages of the hydrodynamic loading of the bird are the initial high shock pressure, shock pressure decay and the steady state pressure.

2.4.2 Shock Pressure

The pressure onset from the first instant of impact is so high that a shock wave is generated at the bird/impacted structure's interface. The pressure in the shock region for subsonic velocities can be represented by the water hammer equation given by

$$p = \rho_0 c_0 v_0 \quad (2.2)$$

where ρ_0 is the initial density, c_0 is the isentropic wave velocity in uncompressed material and v_0 is the velocity of the bird material. As the impact velocity increases beyond subsonic range, a modified version of the water hammer equation is used to obtain the Hugoniot pressure, or shock pressure, generated at the interface as the shock wave propagates into the bird and is given by

$$p_H = \rho_0 v_s v_0 \quad (2.3)$$

where v_s is the velocity of shock in the bird material.

Both equation (2.2) and (2.3) are only valid for a perfectly rigid target. Compliant materials, such as an aircraft transparency, absorb energy in various forms, including kinetic energy, elastic strain energy and through plastic deformation. For compliant materials, the above equation was modified by Wilbeck and Rand [5] to include the compliant effects. This equation is given by

$$p_c = \rho_P v_{SP} v_0 \left[\frac{\rho_T v_{ST}}{\rho_P v_{SP} + \rho_T v_{ST}} \right] \quad (2.4)$$

where p_c is the pressure at the center of the impact zone, and the subscripts P and T represent projectile and target. The shockwave velocities v_{SP} and v_{ST} for the projectile and the target can be computed from the linear Hugoniot equation

$$v_s = s v_0 + c_0 \quad (2.5)$$

where s and c_0 depend on the material.

2.4.3 Shock Pressure Decay

The shock pressure loading decreases with time and also with distance from the center of the impact region. Previous experimental studies [13] shown that the radial pressure distribution is given by

$$p_r = p_c e^{-\frac{Kr}{R(t)}} \quad (2.6)$$

where p_c is obtained from equation (2.4), K is a constant, r is the radial distance from the center of the impact region, and $R(t)$, a function of time, is the maximum contact radius at time t .

The length of this high pressure event is on the order of tens of milli-seconds. This is followed by a pressure release wave traveling towards the center of the impact zone, eventually attaining an approximate steady state.

2.4.4 Steady State Pressure

The stagnation pressure on the impacted surface during this steady state is given by

$$p_s = k\rho_0 v_0^2 \quad (2.7)$$

and is independent of bird shape. The steady state pressure is usually taken as 10-30% of the peak Hugoniot shock pressure at the center of the impact region, based on experimental studies [13]. For an incompressible fluid, $k = \frac{1}{2}$; but for most materials density increases with pressure, and as a result, k may approach a value of 1.

Wilbeck and Rand [5] conducted an extensive test program with substitute birds of various materials and shapes. They concluded that a real bird can be accurately modeled analytically by a mixture of 85-90 volume percent water and 10-15 percent of air, with slightly increased density for water of 1.06 g/cm³.

For testing purposes, they recommended that a gelatin bird with 15 % porosity (to account for the voids in real birds) represents a real bird accurately. They also found that a substitute analytical/synthetic bird will be more accurate if it is modeled as a cylinder with hemi-spherical ends and a length-to-diameter ratio approximately the same as the bird being modeled.

2.5 Numerical Models for Bird and Structure

During the preliminary design phase, a soft body loading model involving simple impact force calculations can be used to obtain a rapid assessment of design parameters, such as leading edge thickness. This type of loading model is based on the change in average momentum or on empirical formulas, such as those presented in [14]. These empirical methods provide the overall magnitude of the impact, but do not predict the details of the damage caused by the complex interaction between the bird and the aircraft.

To improve on these empirical methods, numerical dynamic analysis codes based on finite elements methods have been developed to represent the complex geometry of both the impacted structure and the bird, in order to model the principal features of the transient impact loads. Structural and material nonlinearities are included in many of the more sophisticated analytical models to account for high strain rates, large deformations, and inelastic strains. The key requirements for bird strike analysis procedures are: the bird model which includes the principal physical features of the bird such as shape, size, aspect ratio and an appropriate constitutive model for the bird; the structural model of the impacted surface; and an accurate representation of the contact/impact interaction between the bird and the impacted structure.

2.6 Modeling Techniques

The finite element simulations may incorporate various solution strategies such as the following: pure Lagrangian approach, Eulerian approach, Arbitrary Lagrangian Eulerian (ALE)

approach, and Smooth Particle Hydrodynamics (SPH) approach. Each of these numerical techniques has distinct advantages and disadvantages.

At first, due to the lack of better alternatives, the Lagrangian bird model became the established international standard for bird strike analysis using numerical bird models with finite element methods. In this approach, both the bird and the impacted structure are modeled independently, with an incompressible fluid material, such as water, describing the bird behavior. The dynamic response of the impacted structure was captured with an elastic-plastic-strain-rate dependent material law.

Solid materials are usually represented using a Lagrangian formulation because of its efficient tracking techniques and ability to incorporate complex material models. In the Lagrangian formulation, however, the mesh is embedded in the structure; and as the structure distorts, the mesh undergoes undesirable distortions that negatively affect the accuracy of the results, especially when used in problems such as bird strike analysis where the bird undergoes severe distortions. Very well known negative volume errors and hour-glass modes occur due to the mesh entangling. These situations can be handled with adaptivity/re-zone methods or by imposing a plastic strain threshold limit to erode the highly distorted elements. However, erosion results in loss of accuracy as it removes strain energy from the model. In addition, adaptivity and remeshing procedures are computationally expensive.

In the Eulerian formulation, just as in most computational fluid dynamics (CFD) problems, the mesh is fixed in space, and the material moves through the mesh. Since the mesh is fixed in space, it does not undergo any undesirable distortions that affect the accuracy of the results. The main drawback of this method is the high solution times due to the fact that the mesh needs to encompass the material location at the current time and a void region around it to

include the location of the material (as the material moves through the mesh) at a future instant in time. Additional effort is necessary to maintain interfaces and to limit numerical diffusion arising from flux transportation. In addition, to describe solid behavior, the solid stress tensor and the history of the material must be transported from cell to cell.

Improvements in the simulation of fluid-structure interaction provided more advanced and realistic bird models such as the Arbitrary Lagrangian Eulerian (ALE) and the Smoothed Particle Hydrodynamics (SPH) methods. Both ALE and SPH methods allow the simulation of bird fluid spreading (subsequent to the impact) into isolated substructures. Both methods offer substantial improvements in numerical stability over a pure Lagrangian formulation, with respect to effects like hour-glassing or unrealistic negative volumes in discrete elements.

Arbitrary Lagrangian Eulerian (ALE), as the name suggests, is a combination of both the Lagrangian and Eulerian formulations, and allows for “automatic rezoning”. It is particularly well-suited for fluid-structure interaction problems. In the single material ALE solver, the nodes on the boundaries and material interfaces are strictly Lagrangian, and thus restrict the material flow into or out of the ALE domain. Multiple material ALE formulation allows the flow of material from cell to cell.

Smoothed Particle Hydrodynamics (SPH) is a meshless formulation, and thus completely avoids the problems such as element distortions and hour-glass modes. SPH is based on Lagrangian formulation, and is developed initially for astrophysical problems. In the SPH formulation, the bird is discretized into large number of interacting masses. Since it is based on Lagrangian formulation, it allows for efficient tracking of material deformations and history dependent behavior. The main drawback of the SPH model is its relatively high CPU times; however, it is highly robust numerically. SPH is more efficient than the Euler mesh because

only the region where the material exists at the current time is modeled; and at the same time it does not suffer from mesh distortions like a pure Lagrangian mesh, since SPH is meshless. Because of these advantages, the SPH technique is becoming increasingly popular among the bird strike research community.

These modeling techniques are explained in greater detail in Chapter 4.

2.6.1 *Target Structural Model*

Due to the high strain rates involved, the model of the impacted structure must include a suitable plasticity model to capture the material and geometric nonlinearities. Typically, a Lagrangian model with an appropriate plasticity model might be appropriate to model the impacted structure.

2.6.2 *Analytical Bird Model*

Choosing a suitable bird model is an important factor in the bird strike analysis problem. The bird model with its chosen material and shape, must be capable of reproducing the same impact forces and stresses as a real bird. The high degree of deformation calls for a geometric nonlinear calculation procedure, such as, the Eulerian or Lagrangian formulation of continuum mechanics. The main limitation of many bird models is that a substitute, homogeneous bird model cannot accurately simulate the complex, nonhomogeneous structure of the real bird body.

Analytical bird models vary widely between researchers, with differences in material, shape, density and aspect ratio. In early bird strike research, the shock wave and the associated Hugoniot pressure in the bird are neglected; and for the calculation of stagnation pressure, the bird is assumed to be a series of incompressible fluid jets, connected in parallel. In later work, the representation of Hugoniot pressure is accomplished by the use of a simple equation of state that accounts for compressibility effects.

Major factors affecting the numerical bird model are bird size/weight, shape, and aspect ratio, in addition to an appropriate equation of state model. For engine bird strike simulations, both bird velocity and orientation should be taken into consideration. The impact velocity for other airplane components is assumed to be the aircraft velocity, and the bird velocity is considered to be negligible.

2.7 Contact/Impact interaction

The contact/impact interaction at the bird/structure interface must be included through a suitable contact algorithm. Constraint-based and penalty-based algorithms are the two most widely used techniques. The constraint-based methods consume some kinetic energy, and therefore, do not preserve the total energy of the system as well as the penalty-based techniques.

Next, the extensive literature review carried out for this work is presented. In most cases, the following summary uses the words of the referenced papers, in order to best state the work of those authors. Quotation marks are not used, but the material should be understood to come directly from the cited papers.

2.8 Literature Review

A number of nonlinear finite element codes such as MAGNA, MARC, NONSAP-M, DYNA 3-D, PW/WHAM, PAM-CRASH, ABAQUS, MSC-DYTRAN, LS-DYNA have been used by various authors to predict the nonlinear structural response due to a bird strike event. These codes vary in the degree of sophistication of the bird loading model. MARC, MAGNA, and NONSAP-M treat the projectile load as an incompressible fluid jet impinging on the impacted structure.

Niering [15] modeled the bird shape with DYNA 3-D finite elements and various homogeneous material laws representative of fluid “stagnation” pressures. He found that using certain bird shapes produced several strong, artificial shock waves upon impact. Also, using a bird material model that did not include the effects of viscosity, produced maximum pressures at the rim of the impact areas instead of at the centers of the impact zones. However, high values of viscosity resulted in numerical instabilities. In metal parts, the strain caused by Hugoniot pressure was negligible, whereas the damage caused by stagnation pressure was quite substantial. Nevertheless, Niering concluded that the Hugoniot pressure might cause initial damage and reduction in strength of the impacted structure, which could affect the magnitude of the damage done by the subsequent stagnation pressure.

Vasko [16] studied the component damage resulting from bird impact on a fan blade. Vasko modeled the bird and the impacted structure independently using LS-Dyna with the Lagrangian approach. As is typical for fan blade studies, the bird strike analysis was carried out in two sequential steps. The first step included the determination of the stresses and the ensuing deformation resulting from a pre-imposed angular velocity to the blade. This was followed by a transient bird strike analysis in which the results from the first step were prescribed as initial conditions. An elastic-plastic-strain-rate dependent material law was used for the impacted structure. The bird was modeled as an ellipsoid with solid elements and material properties very similar to water. The blade was modeled with plate elements of varying thickness. The total extent of the damage associated with the impact event was correlated with the experimental results.

Hörmann et al. [17] performed selective deterministic simulations, including bird strikes on composite and metallic horizontal tailplanes of an airliner, using the Lagrangian and Arbitrary

Lagrangian Eulerian (ALE) approaches for the bird. The impacted structure was modeled using finite elements based on a Lagrangian formulation. The bird was modeled as a cylinder with hemi-spherical ends. For the ALE approach, both the bird and the control volume of the surrounding air were meshed.

Hörmann et al. [17] observed that the Lagrangian model for the bird, consisting of solid elements, experienced very large element distortions, which in turn, artificially stiffened the bird, thus resulting in a more localized failure of the target. The bird model with ALE formulation was softer and the target deformation was less localized, and spread over a greater area. The resultant velocity of the impacted structure was not influenced by the bird strike.

Bird impact and foreign object damage on fan and compressor blades was analyzed by Storace et al. [18]. They compared the results of their analyses with experimental results. The transient response of the blades due to bird impact was obtained using the NOSAPM finite element code. NOSAPM is a modified version of NONSAP [19], a nonlinear structural analysis program, capable of very detailed analyses employing 3D elements. The modified version, NOSAPM incorporates an interactive bird-loading model, which treats the bird impact event as a fluid dynamic process, with the bird impact modeled as a fluid jet impinging on an arbitrarily shaped three-dimensional deformable surface. The jet impact problem was treated as a quasi-steady, potential flow by ignoring the initial shock resulting from the Hugoniot pressure. Thus the complex impact problem was reduced to the problem of solving the Laplace equation. NOSAPM has the capabilities to model the geometric nonlinearities resulting from large deformations as well as the material nonlinearities resulting from the elasto-plastic behavior characteristic of a foreign object impact event. NOSAPM is also capable of addressing local effects, as well as the gross structural damage resulting from an impact. The bird was modeled

as a right circular cylinder. The inelastic material behavior was modeled with a bilinear stress-strain curve.

For experimental testing, Storace et al. [18] used a cylindrical substitute bird made of micro-balloon/gelatin material. Comparison of the experimental results with the results obtained from the nonlinear NOSAPM analysis showed good agreement between the displacements and strains.

A Smoothed Particle Hydrodynamics (SPH) model of the bird was used by Anghileri et al. [20] to investigate the effect of bird strike on the composite intake of a turbofan engine. Since the external skin panels of the nacelles were made of composite materials, a series of experimental tests were carried out on thin-walled cylinders and on test specimens resembling static test specimens to investigate the behavior of the composite material subjected to dynamic loading. These experimental results were correlated with the corresponding numerical models by using a variety of material models available in LS-Dyna 970 [21]. The various parameters of these material models were calibrated to obtain a good agreement between the numerical and experimental results. These tests demonstrated that the dynamic behavior of the composite material had a significant effect on the dominant failure mechanism of the event. With this prior knowledge of dynamic behavior of composite materials, a numerical model of the composite turbofan intake was modeled with 4-noded shell elements. The SPH model of the bird had the shape of a rugby ball, and consisted of 1500 SPH particles. The interaction between the bird and the composite intake was defined using the nodes to surface contact algorithm of LS-Dyna 970. Anghileri et al. reported that their numerical model reproduced the failure mechanism of the experimental test.

A series of tests were carried out by Anghileri et al. [2] to develop an understanding of the characterization of a numerical bird model with reference to the impact of a bird against the intake of a turbofan engine. The test procedure involved launching 4 lb chickens at a velocity of 265 knots onto a target inclined at 30 deg. Anghileri et al. [2] optimized the various parameters that define the numerical bird, such as, aspect ratio, shape, density of the bird material etc. They concluded that a rugby ball shape is the optimal shape for a numerical bird, and unlike other tests with real birds, they reported that these tests were repeatable.

Anghileri et al. [2] used LSTC/LS-Dyna [22] in their investigation of various types of bird models. Specifically, they investigated Lagrangian, Eulerian, Arbitrary Lagrangian Eulerian (ALE), Smoothed Particle Hydrodynamics (SPH), and Nodal Masses (NM) methods. All the birds were modeled as a water projectile in the shape of a rugby ball (with a length of 20 cm and diameter of 10 cm). For the constitutive law, the null material of LSTC/LS-Dyna was used, and Grüneisen's equation of state was included. Their experiments yielded the following conclusions with respect to the numerical bird models: The Lagrangian bird model gave accurate results if the bird was not highly deformed. However, for a highly distorted bird mesh following impact and penetration, the Lagrangian model produced highly erroneous results and long solution times – if the simulation did not result in an abnormal termination. The authors reported that the inclusion of a failure criterion to erode the highly distorted elements had an adverse effect on the correlation of the Lagrangian model with the tests results.

Both Eulerian and Arbitrary Lagrangian Eulerian (ALE) models lacked the sharp edges seen in the experiments. In addition, it was noticed that the Eulerian bird *trembled* when crossing the Eulerian mesh, and the ALE bird had an unreasonable amount of stretching at the end of the simulation. The correlation of both the Eulerian and ALE bird models with the

experimental tests was poor. Anghileri et al. [2] suggested that a bird model with a refined mesh might improve the accuracy of the results in both Eulerian and ALE cases, but that would increase the already long solution times associated with these two models.

The Nodal Masses (NM) model of the bird resulted in an unrealistic behavior, due to the lack of any interaction between the nodal masses. The introduction of a dissipation mechanism, such as the inclusion of damping in the contact algorithm (at the interface between the impacted surface and the bird), resulted in a more realistic behavior of the bird. In addition, it improved the stability of the solution, improved the accuracy of the results and reduced the solution time.

The Smoothed Particle Hydrodynamics (SPH) bird model behaved very similar to the Nodal Masses model, but yielded more realistic results. In particular, the scattering of SPH particles was very similar to what was seen in experimental tests. Both the SPH and the refined Nodal Masses bird models produced good correlations with the experimental results, and both required very low CPU times. Increasing the viscous damping coefficient improved the stability of the solution and eliminated the spurious spikes in the contact force due to the Lagrangian/SPH coupling. Based on the above advantages and disadvantages, Anghileri et al. [2] concluded that the SPH bird model was the most reliable in reproducing the detailed dynamics of the bird strike event.

The ALE and SPH methods were used by Frischbier and Kraus [3] to predict the impact loading and response of the front stage of a high pressure compressor in the event of bird ingestion. They found that, compared to the conventional Lagrangian formulation, both ALE and SPH methods offered substantially high numerical stability. They also concluded that the SPH method was more accurate than the ALE formulation. The inaccuracies in the ALE model resulted from the fact that the bird slurry progressed too far into the low pressure compressor.

The bird strike resistance of the leading edge slats of the Eurofighter 2000 (EF-2000) wing was investigated by Rueda et al. [4] using the explicit integration commercial code PAM-CRASH [23]. The model included adaptive meshing capability with the Johnson-Cook material model, which is a strain-rate dependent plasticity model. The Johnson-Cook model is given by

$$\sigma_n = \sigma_y \left[1 + p^{-1} \ln \left(\frac{\varepsilon'}{D} \right) \right] \quad (2.8)$$

where:

σ_n = yield stress at an effective strain rate of ε'

σ_y = yield stress at a strain rate of D

ε' = effective strain rate

p, D = material parameters.

The transient, nonlinear analysis included geometric nonlinearities resulting from the large deformations, material nonlinearities resulting from elastic-plastic behavior, and the frictional nonlinearities resulting from the contact interaction at the interface between the bird and the impacted structure.

The effect of a wide range of parameters, such as, the bird mass, bird velocity, sequences of impact at various locations and at different slat configurations, were studied. The bird was modeled as an ellipsoid and a cylinder, with an equivalent mass of water, using the Lagrangian formulation. Reduced integration and hour glass control were used to eliminate the inaccuracies resulting from excessive distortions of the bird model. The slats were modeled using 4-noded shell elements, with reduced integration for hour-glass control. A damage/failure model was included to eliminate the elements that reached a pre-set level of plastic strain. The bird material was treated as an ideal fluid, with a linear equation of state. The authors reported that the bird

slid in the outboard direction, producing an oblong dent in the skin due to the sweepback of the leading edge. As a result, the area of the leading edge skin interacting with the bird tended to change over the length of the impact event.

With regards to the shape of the numerical bird model, Rueda et al. [4] concluded that at relatively high impact speeds, the shape of the bird model was immaterial, as long as the mass and length were maintained. They also concluded that if the effects of strain rate were neglected in the analysis, unrealistically high levels of spurious damage would be predicted by the analysis. For high speed bird impacts, the internal forces of the bird were less important than the inertia forces resulting from the bird mass. Therefore, the correct representation of bird mass was an important factor in the bird model. An accurate representation of bird compressibility is necessary, because the material compressibility of the bird determines the time history of the interaction forces between the bird and the impacted structure. Representing the bird as an equivalent mass of water was conservative in that birds are actually composed of approximately 67% water. It was noted that an increased level of compressibility would result in a “softer” impact, and thus a “longer” impact event, thereby reducing the interaction force at each instant.

Jain and Ramachandra [24] investigated the response of a centrifugally stiffened blade subjected to a bird impact. They used the commercially available MSC-DYTRAN [25], an explicit finite element code with hydrodynamic coupling. The bird was modeled as a hydrodynamic cylindrical projectile, with a length-to-diameter ratio of 2, and with the density of water. The bird was modeled with brick elements in an Eulerian mesh, and the blade disc geometry was modeled using a Lagrangian mesh with Belytschko-Tsay shell elements. At the interface between the bird and the blade, Arbitrary-Lagrange-Euler coupling was defined. The

authors reported good correlation with experimental results. They also noted that the bird impact load resulted in a transient axial force in the forward direction on the blade.

Anghileri and Bisagni [26] proposed a new bird finite element model consisting of only nodes with added lumped masses and initial velocity. This new bird model, being meshless, would neglect the bird deformation, and thus eliminate the issues of numerical instability arising from the extreme deformations that the bird elements undergo in a Lagrangian bird model during the impact process. The new bird model was used to investigate the multiple bird impact case for a civilian aircraft turbofan inlet. The entire problem was solved using the pure Lagrangian approach. This new bird model was compared to a bird model using on an equation of state, based on the Brockman model.

The Brockman model is a polynomial equation of state based on a hydrodynamic, isotropic, non-viscous constitutive law given by

$$p = C_0 + C_1\mu + C_2\mu^2 + C_3\mu^3 \quad (2.9)$$

where C_1 , C_2 , and C_3 are linear, quadratic and cubic models of compressibility, C_0 is a constant, and μ is the non-dimensional parameter given by

$$\mu = \left(\frac{\rho}{\rho_0} \right) - 1 \quad (2.10)$$

where ρ_0 and ρ are the initial density and the actual density, respectively.

Anghileri and Bisagni [26] reported that the new meshless lumped mass model required some calibration, but otherwise produced results that agreed well with the Brockman model, and was well suited for the analysis involving multiple impacts phenomena. In addition, the CPU time required for the new meshless model was about 1/10th of the CPU time required for the Brockman model.

Baughn and Graham [13] compared the results of a bird strike simulation on an aircraft canopy material with experimental results on test coupons obtained from air cannon impact tests. They used ABAQUS, a general purpose finite element code, which utilizes the updated Lagrangian approach for a nonlinear solution sequence. Based on previously published results, it was assumed that the impact would result in large displacements and rotations, but not in large plastic strains. For impact testing, a rubber ball was used to simulate the bird. They observed that the rubber ball, with a specific gravity between 1 and 2, resulted in large displacements and rotations, but not in large plastic strains. Since an actual bird behaves like a water jet, the projectile was treated as an inviscid fluid with zero shear strength, and the target was treated as an elastic-plastic material.

The loading of the finite element model included only the steady state pressure, and it was assumed to be equal to 10% of the peak shock pressure at the center of the impact region. Equation (2.6), which is repeated here, was used for computing the radial pressure decay from the impact center.

$$p_r = p_c e^{-\frac{Kr}{R(t)}} \quad (2.6)$$

The value of $R(t)$ was changed with each time step, and the value of K was taken as 6.4 to meet the far field boundary condition of insignificant pressure at the maximum radius. The model used isoparametric brick elements, each with 27 nodes. Baughn and Graham [13] observed that the boundary conditions at the ends of the test specimens had a significant effect on the results. It was noted that the impact loads induced both bending and tension in the specimen. Changing the model end conditions from fixed constraints to include a certain degree of tensile flexibility resulted in a much better agreement with the experimental centerline displacement history. Highest stresses occurred at the end restraints, however, elements slightly

inward from the ends were the first to experience high stresses. The authors concluded that for the impact loads studied, there was little plastic deformation, and therefore, large strain capability was not needed.

A nonlinear explicit finite element program, DYNA-3D, was used by Boroughs [27] to provide guidance in the design of a one-piece windshield for the Learjet 45. The various problems that could arise during bird-shot testing include “punch through” at the initial impact point, detachment of the windshield adjacent to the support structure, separation of the windshield from the support structure, and pull through of the attachment fasteners. The windshield configuration has a one-piece transparency on the right and left sides of the crew section, and was fabricated from laminated polycarbonate material consisting of an outer glass ply, a urethane interlayer, a polycarbonate ply, a urethane middle layer, another polycarbonate ply, a second urethane interlayer and an inner face ply of acrylic to resist scratching and discoloring. Each ply and each interlayer was modeled using 8-node solid elements and the supporting structure was modeled using beam and shell elements. Polycarbonate plies were refined to include two layers of solid elements to alleviate hourglass problems. The material for solid elements was modeled as elastic-plastic with linear strain hardening. The load was modeled using a time varying pressure determined from linear impulse and momentum equations given by

$$P = \frac{I}{\sum At} \quad (2.11)$$

and the impulse I is given by

$$I = mv \quad (2.12)$$

where A is the area of the finite element mesh under the bird imprint at any given time increment t , and m is the mass of the bird.

Martin [28, 29], in his pursuit of an engineering solution to the complex issue of bird impact on fan-blades, enhanced the capabilities of WHAM by adding a method to predict the effect of a soft body impact. WHAM is an explicit, nonlinear, transient finite element solution procedure with plate elements. Martin introduced a spherical fluid element to transfer the projectile loads to the impacted structure through momentum exchange. The Hugoniot pressure effect and the viscosity effect were neglected. The spherical fluid element can only expand or contract. The internal pressure due to the change in the volume of the fluid element is given by

$$p = \beta \ln\left(\frac{V_0}{V_i}\right) \quad (2.13)$$

where β is the bulk modulus, V_0 is the initial volume, and V_i is the instantaneous volume. The resulting force on the impacted structure at the area of contact is given by

$$F = 3\pi\beta(R_0^2 - R_i^2)\ln\left(\frac{R_0}{R_i}\right) \quad (2.14)$$

where R_0 is the initial radius and R_i is the instantaneous radius, which depends on the distance to the neighboring fluid elements, and is given by

$$R_i = \frac{1}{n}\left(\frac{D_1}{2} + \frac{D_2}{2} + \dots + \frac{D_n}{2}\right) \quad (2.15)$$

where D_i is the distance from the i th neighbor and n is the total number of neighbors.

The soft body projectile was formed by the closely packed spherical fluid elements, and to compensate for the loss of mass due to the presence of voids between the spherical elements, the density of the fluid was increased.

The modified version of WHAM is called PW/WHAM, and is in fact, a primitive form of the more advanced, current state-of-the-art meshless methods. Martin observed that the fluid elements tended to “stiffen” with increasing deflection, and also tended to “bounce-off” of the

target. This problem was alleviated by introducing an energy depletion mechanism based on a variable bulk modulus. Martin [28, 29] used PW/WHAM to predict the effect of soft body impact on a simple flat plate, a blade-like tapered flat plate, and the fan-blade of a fighter engine. In all cases, the structure was modeled with constant strain triangular elements. Viscous damping was applied to the structural elements to attain the final deflected shape with reduced solution times. Martin reported a good correlation with experimental results in all cases.

One of the recent and more advanced studies on the effect of bird shape in numerical simulations of bird strikes was carried out by McCallum and Constantinou [6]. They compared the results of a traditional, homogeneous, hemi-spherical cylindrical bird model to a more detailed bird model having multi-material parts. They observed that the target became pre-stressed from the initial impact of the head and neck, prior to the impact of the bird torso. Traditional bird models consider only the torso, and ignore the effect of the neck, head, and wings. Consequently, they are incapable of simulating the pre-stress effect of head and neck impact, which may have important consequences for damage initiation and failure of the target.

The effect of small birds may be adequately simulated using a simpler model, consisting of only the homogeneous torso of the bird, which is typical for almost all bird models to date. However, in the case of a large bird, such as a Canadian goose, such a primitive model may not be adequate, since its wings and neck contribute to the total mass of the bird and play a critical role by pre-stressing the target.

It is prohibitively difficult to experimentally replicate a large bird like a Canadian goose with its neck extended. Fortunately, numerical simulation is a useful tool for analyzing such physically uncontrollable situations. The importance of the mass and the length of the neck

should not be ignored, as they contribute to increasing the duration of impact. Other large birds present similar difficulties.

CHAPTER 3

GOVERNING EQUATIONS

Simulating the collision of a bird with a flight vehicle is a highly nonlinear problem that involves both kinematic nonlinearities and material nonlinearities due to high strain rates, large deformations, and inelastic strains. Additional complications arise due to the inherent coupling between the impact loads and the response of the target structure.

One of the pioneering works in the field of bird strike analysis was carried out by Wilbeck [8, 10], who proposed that hydrodynamic theory could be applied to any projectile material during an impact event when the stresses in the projectile greatly exceed the projectile material strength. He was successful in demonstrating that these projectile materials, referred to as “soft body” materials, can be considered to behave as fluids because of their negligible material strength. As a first step in the application of the hydrodynamic theory, Wilbeck decoupled the impact loads from the target response by assuming the target structure to be rigid, and then included the effects of target flexibility. Some of the details of Wilbeck’s theory were discussed in Chapter 2.

The above-mentioned method estimated the impact loading using 1-D shock relations in the shock regime, and by solving the 1-D compressible Bernoulli equation for the steady flow regime. However, today's computer technology permits routine economical solutions of the fully non-linear 3-D governing equations with contact conditions. The following section introduces the fully non-linear 3-D governing equations, namely, conservation of mass, conservation of linear momentum, conservation of angular momentum, and conservation of energy [22, 30, 31].

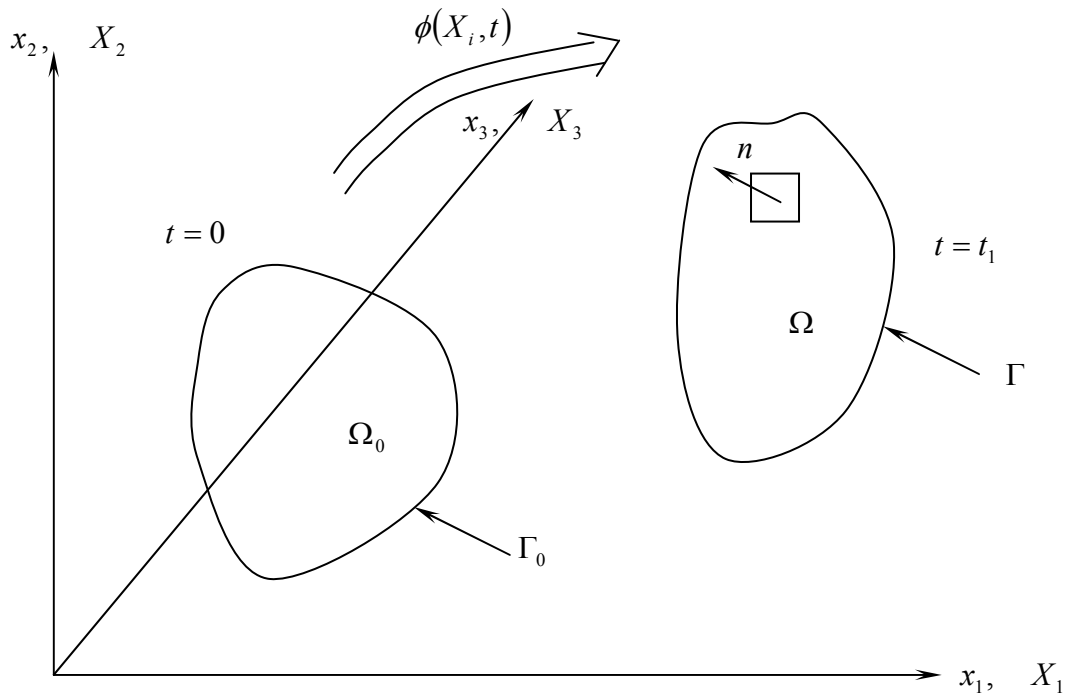


Figure 3.1. Undeformed (initial) and deformed (current) configurations of a body.

3.1 Conservation of Mass

The conservation of mass equation can be stated as

$$\rho J = \rho_0 \quad (3.1)$$

where ρ_0 and ρ are the densities in the initial and current configurations, respectively, and J is the Jacobian determinant, which is equal to the determinant of the deformation gradient \mathbf{F} given by

$$F_{ij} = \frac{\partial x_i}{\partial X_j}. \quad (3.2)$$

In the above equation, x_i is the current position of a point, and X_i represents the location of the point in the original or reference frame. Both i and j range from 1 to 3 for 3-D.

In a numerical computation procedure, the current density value ρ is computed based on the principle of conservation of mass, using the known initial density ρ_0 .

3.2 Conservation of Linear Momentum

The conservation of linear momentum can be stated as

$$\sigma_{ij,j} + \rho b_i = \rho \dot{v}_i \quad (3.3)$$

under the appropriate boundary conditions.

In the above equation, σ_{ij} is the Cauchy stress, b_i is the applied body force per unit mass, and v_i is the velocity in the current configuration. The dot above v_i represents the material time derivative.

The applicable boundary conditions can take the following three forms:

3.2.1 Traction Boundary Condition

The traction boundary condition can be written as

$$\sigma_{ij} n_j = t_i \quad (3.4)$$

where t_i are the components of the traction vector, and n_j are the components of the surface normal.

3.2.2 Displacement Boundary Condition

The displacement boundary condition takes the following form:

$$x_i(X_i, t) = D_i(t) \quad (3.5)$$

where D_i are the components of the enforced displacement vector.

3.2.3 Contact Boundary Condition

At the contact surface, the displacement components of the two contacting surfaces must satisfy the constraint given by

$$(x_i^\alpha - x_i^\beta)n_i^\alpha \leq 0 \quad (3.6)$$

where the superscripts α and β refer to the two contacting surfaces.

In the above equation, when the constraint is an equality, the normal component of the tractions on the contacting surfaces must be equal and opposite. This condition can be written as

$$\sigma_{ij}^\alpha n_i^\alpha n_j^\alpha - \sigma_{ij}^\beta n_i^\beta n_j^\beta = 0. \quad (3.7)$$

3.3 Conservation of Angular Momentum

In the absence of body couples, conservation of angular momentum simply states that the Cauchy stress tensor is symmetric, that is,

$$\sigma_{ij} = \sigma_{ji}. \quad (3.8)$$

3.4 Conservation of Energy

The conservation of energy equation is used to compute the internal energy e which is used in the equation of state to obtain the pressure-density relationship of a given material. The conservation of energy can be written as

$$\rho \dot{e} = \sigma_{ij} \dot{\epsilon}_{ij} + \rho b_i v_i \quad (3.9)$$

where $\dot{\epsilon}_{ij}$ is the strain rate tensor.

The strain rate is the same as the deformation rate D_{ij} . The deformation rate D_{ij} is obtained from the velocity gradient L_{ij} . The velocity gradient L_{ij} is defined as

$$L_{ij} = \frac{\partial v_i}{\partial x_j}. \quad (3.10)$$

The velocity gradient L_{ij} can be split into a symmetric component D_{ij} and a skew-symmetric component W_{ij} as follows:

$$D_{ij} = \frac{1}{2}(L_{ij} + L_{ji}) \quad (3.11)$$

$$W_{ij} = \frac{1}{2}(L_{ij} - L_{ji}). \quad (3.12)$$

W_{ij} is also known as the vorticity or spin tensor.

3.5 Principle of Virtual Work

The weak form of a governing equation automatically includes the traction boundary conditions, also known as the natural boundary conditions. The principle of virtual work is the weak form of the equation of conservation of linear momentum along with the traction, displacement and contact discontinuity boundary conditions. The linear momentum equation along with the prescribed boundary conditions is called the generalized momentum balance. The weak form of the generalized momentum balance can be written as follows:

$$\int_V (\sigma_{ij,j} + \rho b_i - \rho \dot{v}_i) \delta x_i dV + \int_{\Gamma_1} (t_i - \sigma_{ij} n_j) \delta x_i dS - \int_{\Gamma_\alpha} (\sigma_{ij}^\alpha n_i^\alpha n_j^\alpha - \sigma_{ij}^\beta n_i^\beta n_j^\beta) \delta x_k^\alpha n_k^\alpha dS = 0 \quad (3.13)$$

where δx_i are arbitrary test functions and can be interpreted as the virtual displacement field.

δx_i must vanish everywhere except where the enforced displacement conditions exist. dS in the above equation refers to the area of a differential segment.

Using integration by parts, the first term in the above equation $\int_V \sigma_{ij,j} \delta x_i dV$ can be written as

$$\int_V \sigma_{ij,j} \delta x_i dV = \int_V [(\sigma_{ij} \delta x_i)_{,j} - \sigma_{ij} \delta x_{i,j}] dV. \quad (3.14)$$

By applying the Gauss's divergence theorem, the first term on the right hand side of equation (3.14) can be written as,

$$\int_V (\sigma_{ij} \delta x_{i,j}) dV = \int_{\Gamma_1} \sigma_{ij} n_j \delta x_i dS + \int_{\Gamma_\alpha} (\sigma_{ij}^\alpha n_i^\alpha n_j^\alpha - \sigma_{ij}^\beta n_i^\beta n_j^\beta) \delta x_k^\alpha n_k^\alpha dS. \quad (3.15)$$

Using equation (3.15), the principle of virtual work now becomes

$$\delta \pi = \int_V \sigma_{ij} \delta x_{i,j} dV + \int_V \rho a_i \delta x_i dV - \int_V \rho b_i \delta x_i dV - \int_{\Gamma_1} t_i \delta x_i dS = 0 \quad (3.16)$$

where a_i is the acceleration.

3.6 Finite Element Discretization

In the previous sections the various fundamental conservation principles were introduced. Of these, the equations of conservation of mass and energy are scalar equations. The equation of conservation of angular momentum forces the Cauchy stress tensor to be symmetric in the absence of body couples, which reduces the number of independent components of stress from nine to six. The law of conservation of linear momentum in 3-D consists of three partial differential equations. The finite element method can be used to solve these partial differential equations.

The finite element method discretizes a continuous, geometrically complex domain into a finite number of simple, discrete elements. These elements are interconnected at element corners, called nodes, over a topological map known as a mesh. Interpolation functions, or shape functions, are built on this mesh. Various quantities of interest, such as displacement, stress, and strain are then tracked through time over the discrete elements, while ensuring inter-element compatibility.

The displacement, velocity and the acceleration fields over each element can be approximated in terms of discretized nodal values as

$$\begin{aligned}
x_i^{(e)}(x,t) &= N_J(x)x_{iJ}(t) \\
v_i^{(e)}(x,t) &= N_J(x)v_{iJ}(t) \\
a_i^{(e)}(x,t) &= N_J(x)a_{iJ}(t)
\end{aligned}
\tag{3.17}$$

where N_J are the known shape functions and are functions of position only. x_{iJ} , v_{iJ} , and a_{iJ} are the unknown nodal displacement, velocity and acceleration components, respectively.

Similarly, the arbitrary test functions δx_i within an element can be written as

$$\delta x_i^{(e)}(x,t) = N_J(x)\delta x_{iJ}(t) \tag{3.18}$$

where δx_{iJ} are arbitrary and independent.

The form of the shape functions N_J depend upon the type of element formulation chosen to model a given structure.

Now, the total virtual work $\delta\pi$ for the continuous domain of interest can be written as a sum of the individual contributions from the discretized elements, as below:

$$\delta\pi = \sum_{e=1}^N \delta\pi^e \tag{3.19}$$

where N is the total number of the discrete elements in the domain. Since the original domain is continuous, the displacement field x_i must be continuous across the boundaries of the discrete elements unless inherent discontinuities exist in the domain.

With the approximations above, the only unknowns are the discrete nodal values of X_{iJ} , which are functions of time only. Therefore, the solution of the partial differential equations over the complex domain becomes much simpler, because the problem now involves solving ordinary differential equations over the discretized domain.

Introducing the above approximations into equation (3.16) results in the following:

$$\sum_{e=1}^N \left[\int_V \sigma_{ij} N_{K,j} dV + \int_V \rho N_K N_L a_{iL} dV - \int_V \rho b_i N_K dV - \int_{\Gamma_1} t_i N_K dS \right] \delta x_{iK} = 0. \quad (3.20)$$

Since the test functions δx_{iK} are arbitrary, the coefficient of δx_{iK} in the above equation must vanish. This leads to the following equation:

$$\sum_{e=1}^N \left[\int_V \sigma_{ij} N_{K,j} dV + \int_V \rho N_K N_L a_{iL} dV - \int_V \rho b_i N_K dV - \int_{\Gamma_1} t_i N_K dS \right] = 0. \quad (3.21)$$

This condition yields one semi-discrete equation of motion for each unconstrained nodal degree of freedom in the domain.

Equation (3.21) can be rewritten in a compact matrix form as follows:

$$\mathbf{M}_{KL} \mathbf{a}_{iL} = \mathbf{F}_{iK}^{ext} - \mathbf{F}_{iK}^{int} \quad (3.22)$$

where \mathbf{M}_{KL} is the mass matrix given by

$$M_{KL} = \sum_{e=1}^N \int_V \rho N_K N_L dV. \quad (3.23)$$

\mathbf{F}_{iK}^{int} and \mathbf{F}_{iK}^{ext} are the internal and external nodal force vectors given by

$$F_{iK}^{int} = \sum_{e=1}^N \int_V \sigma_{ij} N_{K,j} dV \quad (3.24)$$

and,

$$F_{iK}^{ext} = \sum_{e=1}^N \left[\int_V \rho b_i N_K dV + \int_{\Gamma_1} t_i N_K dS \right]. \quad (3.25)$$

3.7 Time Integration – Implicit vs. Explicit

The semi-discrete set of equations of motion given by equation (3.22) can now be solved as a function of time by first fully discretizing the given equations utilizing finite-difference approximations for time derivatives, and then marching through time to solve the set of

equations at incremental values of time. There are two different types of temporal solutions available, namely, an implicit time integration procedure and an explicit time integration procedure.

3.7.1 *Implicit Time Integration*

When implicit time integration is adopted for solving the finite difference formulation of equation (3.22), more than one unknown appears in each equation. Consequently, implicit time integration requires the solution of a set of simultaneous equations at each time step. Therefore, implicit solution procedures are computationally intensive. However, unlike the explicit time integration procedure discussed later, most implicit time integration schemes are unconditionally stable. As a result, much larger time steps can be chosen for each iteration, and therefore, require shorter solution times. However, opting for too large a time step degrades the solution accuracy due to the increased truncation errors associated with the finite difference formulation.

In addition, the size of the time step may also be limited by issues related to convergence for those problems with a high-degree of nonlinearity. In general, the time step size for an implicit integration is taken to be about the same as that for an explicit integration in order to satisfy the accuracy requirements [32]. In addition, it is reported that the cost of an implicit time step is ten to thousand times more expensive than an explicit time step [33]. Since each implicit time step is computationally more intensive compared to an explicit time step, the use of implicit integration is limited.

3.7.2 *Explicit Time Integration*

In explicit time integration procedures, only one unknown appears in each finite difference equation at each time step. This eliminates the need to assemble a set of simultaneous equations at each time step since each individual equation can be solved independently.

Therefore, the computational effort necessary in explicit procedures is much less than that associated with the implicit solution procedures. However, a major drawback of the explicit solution schemes is the limitation on the size of the time step. This is due to the fact that the computed response for explicit solvers grows unbounded if the size of the time step is not restricted. Therefore, the explicit time integration procedures are conditionally stable; that is, the size of the time step is limited by the stability criterion known as the Courant-Friedricks-Lewy (CFL) criterion [32]. According to the CFL criterion for linear problems, the time step Δt for explicit integration is given by

$$\Delta t \leq \frac{2}{\omega} \quad (3.26)$$

where ω is the highest natural frequency of the computational mesh.

For nonlinear problems, the time step Δt is typically determined from

$$\Delta t \leq \frac{kl}{c} \quad (3.27)$$

where l is the minimum mesh dimension and c is the velocity of sound. The value of k is generally chosen to be between 0.6 and 0.9.

3.8 Solution Strategy

Many successful commercial finite element codes are currently available for analyzing highly non-linear transient problems where contact plays an important role. Many of these codes are used by various researchers, and have been proved to be accurate and adequate for many classes of problems. Furthermore, most of these codes include various modeling options for both the impacted structure and the impactor (the bird in this case). In addition, they contain numerous material models, and equation of state formulations. Therefore, instead of developing yet another code for this work, a well-benchmarked, commercially available, general purpose

finite element code – LS-Dyna – was selected for solving the bird strike problem. The temporal integration procedure used for this work was LS-Dyna’s explicit time integration solver. The general explicit time integration loop in LS-Dyna is reproduced in Figure 3.2 from [22].

The element formulations and the corresponding shape functions used for modeling the target structure can be found in the LS-Dyna theory manual [22]. The modeling techniques and the element formulations used to represent the bird model are explained in detail in the next chapter.

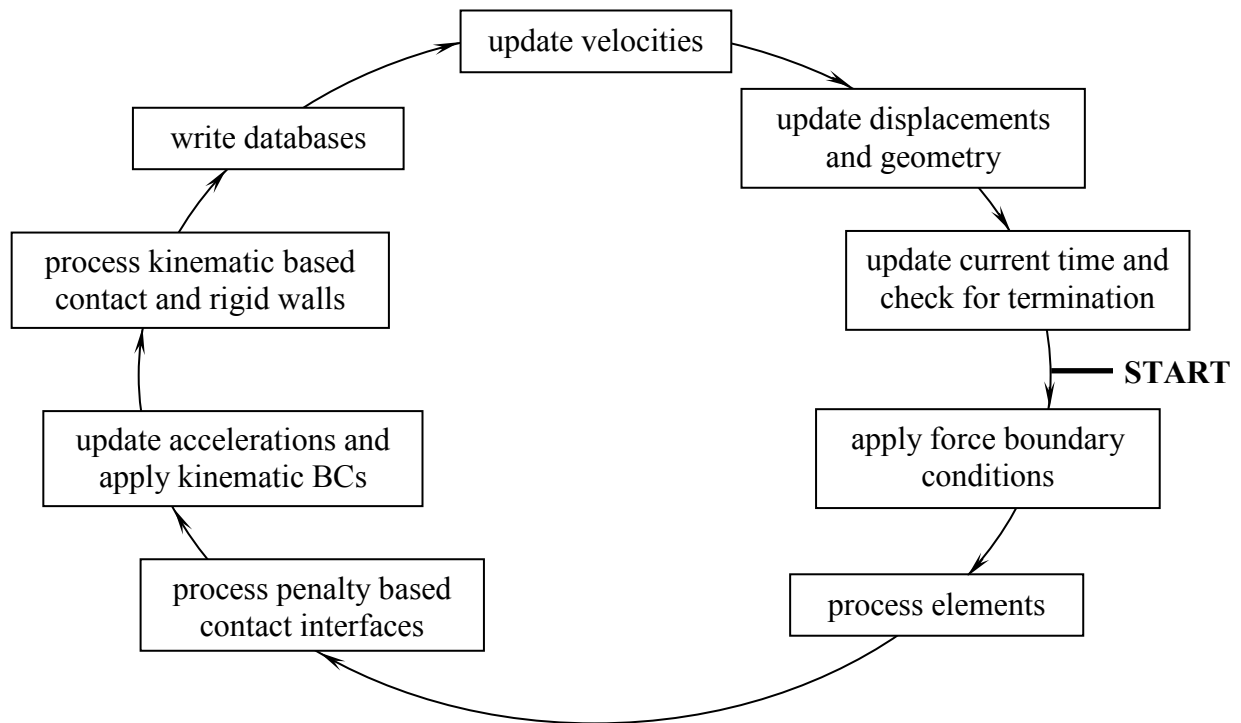


Figure 3.2. Explicit time integration loop in LS-Dyna.

CHAPTER 4

SPATIAL DISCRETIZATION MODEL FOR BIRD

The impact of a bird with an aircraft is an example of a class of problems associated with the impact of a "soft" projectile with a much larger (greater mass), stiffer, and stronger body. The soft body projectiles are highly deformable upon impact and tend to flow over the target, essentially behaving very much like a fluid, thereby spreading the impact load over a large area of the target surface, relative to the frontal area of the projectile. An accurate prediction of the response of the target to the impact is very dependent upon an accurate representation of these bird impact loads on the target structure. Consequently, selecting an appropriate spatial discretization model to represent the bird in numerical simulation is a crucial part in the simulation. There are several leading numerical techniques for the spatial discretization of the bird, each with different advantages. These are briefly reviewed in this section in order to choose the most satisfactory modeling technique that accurately captures the soft body impact phenomena.

Most of the early researchers, for lack of other suitable alternatives, depended on the Lagrangian technique to model both the bird and the target structure in the simulation of a bird strike event. However, Lagrangian elements for the bird proved unsatisfactory, because the bird behaves hydrodynamically, undergoing severe deformations upon impact. The consequent severe distortions in the Lagrangian elements of the bird resulted in several difficulties, such as a necessity for an extremely small time step size and negative element volumes.

Current-generation numerical discretization techniques can be divided into various categories based on spatial and temporal discretization procedures. Temporal discretization methods, also known as time marching techniques, were briefly discussed in Chapter 3. In

general, the candidate spatial discretization techniques can be sub-divided into Lagrangian, Eulerian, Arbitrary Lagrangian Eulerian (ALE), and various types of meshless methods. Of these, the Lagrangian technique is most commonly used in solid mechanics, and the Eulerian method is preferred by the fluid dynamics community, although these techniques are not entirely limited to these fields. However, in problems involving two different physical media, such as fluid-structure interaction problems, there is usually no single technique that fully suits the modeling requirements of the two distinct physical media.

This is where the remaining two methods – the Arbitrary Lagrangian Eulerian (ALE) and the meshless, or particle methods – have an advantage. Both of these methods offer the ability to optimally model each distinct medium using a technique that best suits only that medium, and they then couple all the different media temporally and spatially in a single simulation. The Arbitrary Lagrangian Eulerian (ALE) method is preferred for the fluid-structure interaction problems where the structural part is modeled using the Lagrangian technique and the fluid is modeled using the Eulerian technique. Meshless methods are also used for fluid-structure interaction problems, especially where severe shape distortions make the Lagrangian mesh inadequate. Of the meshless methods, only the Smoothed Particle Hydrodynamics (SPH) technique is presented here, since it is the method chosen for this work. The SPH technique is based on the Lagrangian framework; but by being meshless, it has been found to be highly capable for modeling large deformation, impact problems.

A brief outline of the Lagrangian, Eulerian, and the Arbitrary Lagrangian Eulerian (ALE) techniques is presented next. The SPH technique is found to be suitable for large distortion problems and it links easily with the standard finite element models. Thus it is chosen for the spatial discretization of the bird model of the current work. Consequently, the foundation of the

methodology for the Smoothed Particle Hydrodynamics (SPH) technique is presented in greater detail.

4.1 Lagrangian Technique

The Lagrangian technique is mainly used for solving problems related to solid mechanics. In this technique, the numerical mesh is attached to the structure. In other words, the structure itself is divided into discrete finite elements, forming the finite element mesh. Therefore, the mesh moves with the structure as shown in Figure 4.1.

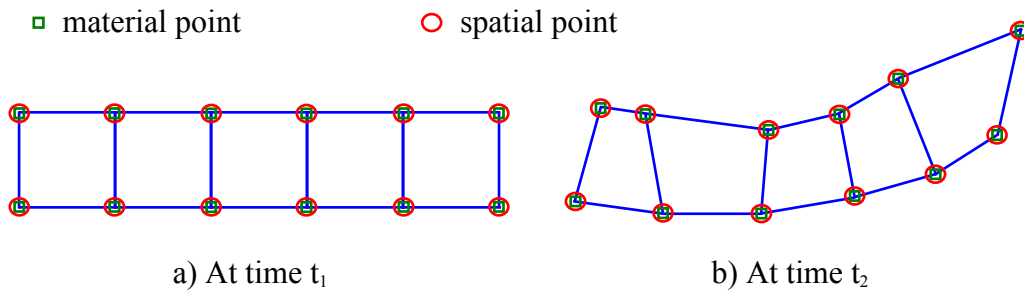


Figure 4.1. Lagrangian description.

Lagrangian-based numerical solvers are generally easier to implement than the Eulerian solvers, because the spatial points of the Lagrangian mesh coincide with the material points of the body being modeled. Consequently, the convective terms normally present in the Eulerian solvers are absent from the Lagrangian formulation. The convective or flux terms result from the relative motion of material from one cell to another with respect to the computational grid. Lagrangian solvers offer simpler treatment of the boundaries, since both the material interfaces and the free surfaces move with the mesh. Likewise, since the mesh is embedded in the structure, the material properties at any point in the structure can be readily tracked. In addition, it is relatively easy to implement complex material models when the Lagrangian solver is

employed, and the time history of material behavior can be easily maintained; since it is contained in the original cell.

On the other hand, since the mesh of the Lagrangian solver forms an integral part of the structure, the deformations and distortions of the structure are reflected in the mesh. Inaccuracies are introduced into the numerical approximations as the mesh distorts. In addition, for an explicit solver the time step for any given iteration is determined by the smallest element dimension of the entire computational domain. Consequently, in case of severe distortions, the time step for a given iteration becomes extremely small, often rendering the computations impractical. Furthermore, severe mesh tangling results in notorious, non-physical negative volumes (see Figure 4.2) in the numerical solver due to the elements folding over themselves.

Several choices exist for dealing with the mesh tangling problems that stem from severe distortions. These include element erosion, adaptive remeshing/rezoning, and “small-strain” simplifications.

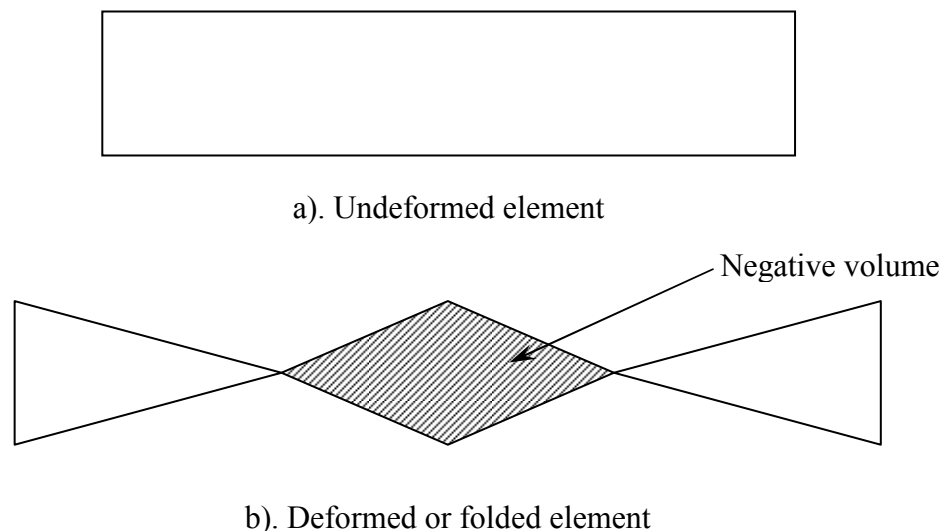


Figure 4.2. Non-physical negative volume for an element of unit thickness.

For element erosion, the distorted elements are deleted from the mesh by imposing a plastic strain limit. Deleting elements that exceed a pre-imposed plastic strain threshold value resolves both negative volumes and time step decrement issues. However, deleting these elements also removes mass and strain energy from the structure, thus violating both conservation of mass and conservation of energy principles. Furthermore, it has been reported that element erosion at the contact-impact interface introduces additional complications [34].

Adaptive remeshing/rezoning, or adaptivity, involves re-meshing the region of severe mesh tangling. This additional step, in addition to increasing the solution time, involves the complex remapping of all the solution variables from the original distorted mesh to the new “regular” mesh. This mapping procedure often increases the numerical errors associated with the approximations. Apart from the increased computational expense, remeshing may not even be possible in some 3-D cases. Frequent rezoning might also diffuse the material time history as well as material boundaries. This technique works best for cases that need few remeshing steps.

Some researchers, for example [35], used the “small-strain” simplification to overcome the negative volumes and extremely small time step issues associated with the Lagrangian approach. The “small-strain” option simply omits updating the Jacobian matrix at each time step, thus ignoring the large structural distortions that might manifest as unrealistic negative volumes. However, the “small-strain” option is not suitable for problems that involve extreme deformations/distortions, such as with the bird strike problem.

4.2 Eulerian Technique

In the Eulerian technique the mesh is basically treated as a control volume. Therefore, the computational grid is fixed in space and the material passes through the mesh as illustrated in Figure 4.3. Since the computational grid is fixed in space, by definition, there is no undesirable

mesh distortion, even if the material passing through it undergoes severe deformation. In addition, an Eulerian technique completely avoids the difficulties associated with the time step reduction required by the type of highly deformed domains encountered by the Lagrangian technique, when used in explicit time integration solutions. Therefore, the Eulerian technique is better suited for problems where predominantly large distortions exist. The Eulerian solver allows the movement of free surfaces and material interfaces through the mesh.

Consequently, a cell in the Eulerian mesh may contain more than one material, and the Eulerian solver can easily handle multiple materials in one cell. The Eulerian technique is typically used in the numerical solution of fluid dynamics problems.

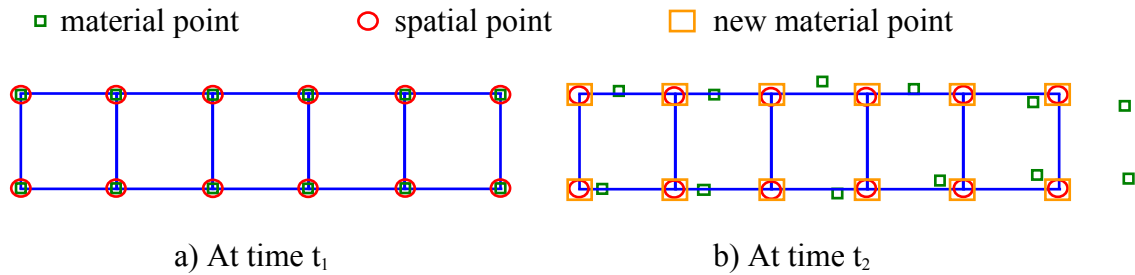


Figure 4.3. Eulerian description.

Since the mesh in the Eulerian technique is fixed in space, the computational domain should encompass not only the region where the material currently exists, but also additional void space to represent the region where material may exist at a later time of interest. This does not pose a problem for fluid dynamics simulations where the primary region of interest is in the vicinity of a fixed body, such as an airfoil. On the contrary, in structural analyses, especially in impact analyses, attention is focused on an object that is in motion. Therefore, use of the Eulerian technique for structural analysis requires a much larger computational domain than the

Lagrangian technique, where the mesh is fixed to the body and thus eliminates the need to model the void space.

Another difficulty associated with the Eulerian technique for structural impact analyses is in keeping track of the material behavior history. In order to maintain the history, the solid stress and strain tensors must be transported from cell to cell, requiring the need for sophisticated techniques to track the material properties.

In the Eulerian technique, since free surfaces and material interfaces are allowed to move through the mesh, these tend to diffuse throughout the computational grid unless special provisions are made to locate them at each time step. One option to limit the diffusion of free surfaces and material interfaces is to resort to preferential transport of materials [32], where calculations for each material at the interface are handled separately.

Furthermore, most Eulerian solvers are based on low-order difference schemes which have built-in sources of error, such as numerical dispersion and numerical dissipation, due to truncation of the Taylor series approximations. These numerical errors can be minimized by resorting to higher-order differencing schemes, but this comes at the expense of increased computational effort.

All the above-mentioned difficulties with the Eulerian technique for structural analyses tend to increase the number of computations required per cell when compared to the Lagrangian technique. In addition, Birnbaum et al. [36] report that the Eulerian technique requires a finer mesh than the Lagrangian technique for the same level of accuracy.

4.3 Arbitrary Lagrangian Eulerian (ALE) Technique

A number of engineering problems, such as fluid-structure interaction problems, exist where neither of the two classical numerical discretization techniques describes both the fluid

parts and the structure parts of the domain adequately. For the numerical simulation of such problems, a technique that combines the best features of purely Lagrangian and Eulerian approaches, while circumventing their inherent disadvantages, is available. The Arbitrary Lagrangian Eulerian (ALE) technique, also known as the mixed Lagrangian Eulerian method, is one such approach. In the ALE technique, in addition to the spatial and material domains associated with the Eulerian and Lagrangian representations, respectively, a reference domain is introduced to treat the computational mesh. The reference domain, as shown in Figure 4.4, is independent of the material particles, similar to the spatial domain in the Eulerian technique, however, it can also move arbitrarily with a velocity w independent of the spatial domain.

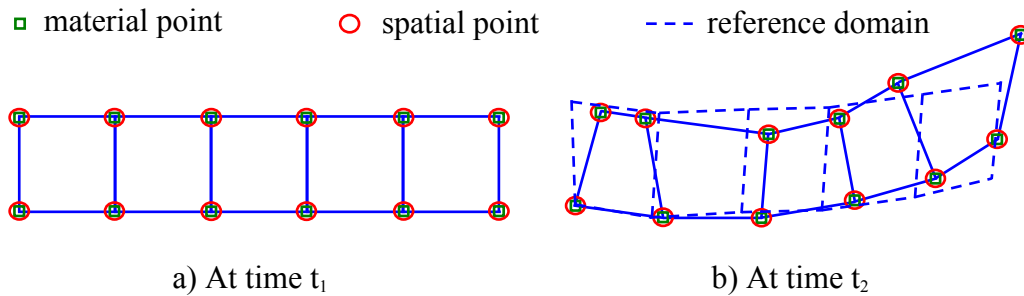


Figure 4.4. Arbitrary Lagrangian Eulerian (ALE) description.

When $w = 0$, the ALE domain becomes an Eulerian domain; and when $w = v \neq 0$, where v is the velocity of the material particles, then the ALE domain becomes a Lagrangian domain. The reference frame corresponds to the ALE domain when $w \neq v \neq 0$.

In general, the material derivative, or total time derivative, of a 1-D function $f(x, t)$ that appears in all the fundamental fluid dynamics and aerodynamics formulations can be written as

$$\frac{df}{dt} = \frac{\partial f}{\partial t} + u \frac{\partial f}{\partial x} \quad (4.1)$$

where $\frac{\partial f}{\partial t}$ represents the local part and $u \frac{\partial f}{\partial x}$ represents the convective part of the material derivative.

From the Lagrangian view point, since there is no relative velocity between the mesh and the material, the convective part disappears. However, for the Eulerian view point, because the material flows through a fixed mesh, the variable u in the convective part will be replaced by the velocity of the material v . In case of the ALE equations, the variable u is equal to the relative velocity between the material and the mesh, and is replaced by $v - w$. Therefore, in order to use the ALE technique, the governing differential equations must be to be modified to include the effect of an arbitrary velocity of the referential domain.

Typically, there are two potential ways of solving the modified ALE equations [37 - 41]. One way is to solve the fully coupled ALE equations. The disadvantage with this method is that it can only handle a single material in an element. The second method of solving the ALE equations involves dividing each solution step into two sequential phases. This approach, known as the operator split approach, performs a Lagrangian step first, in which the material is moved with the mesh; and this is followed by a second step in which the solution is mapped from the Lagrangian domain to the reference domain. This operator split approach simplifies solving the fully coupled governing equations by breaking them into two sets, which are then solved sequentially. Thus, the Lagrangian and the Eulerian steps are carried out individually, independent of each other, unlike the case of the fully coupled equations. In general, the algorithms for the operator split approach are computationally more economical and more robust than those for solving the fully coupled equations. However, some accuracy might be lost due to the decoupling of the governing equations. Furthermore, most advection algorithms, used for the second step, tend to smooth out the sharp gradients in the solution.

4.4 Smoothed Particle Hydrodynamics (SPH) Technique

The Smoothed Particle Hydrodynamics (SPH) technique is a Lagrangian based, meshless technique. It was first introduced in the field of astrophysics to deal with fluid masses moving arbitrarily in three-dimensional space [42 - 44]. Since the SPH method is a purely Lagrangian technique, it can be easily linked to finite element solutions based on the Lagrangian formulation. In addition, due to the absence of a mesh connecting the individual particles, the SPH technique can handle problems involving large deformations, with greater ease. In the SPH method, the continuum is treated as a random set of particles that interact with each other. SPH is a technique that has foundations in the interpolation theory, and allows any function to be expressed in terms of the values of the same function at a set of disordered points that makeup the continuum [44]. Spatial derivatives of various field variables are computed using kernel estimates, in the absence of regular connectivity between the particles found in methods that use a mesh.

In the SPH technique, each particle has a mass assigned to it [43]. Field variables of a particle are computed through interpolation of the neighboring particles. A particle is considered a neighbor when it falls within the smoothing length of another particle.

The integral interpolant of any function $f(\mathbf{x})$ can be written as

$$f(\mathbf{x}) = \langle f(\mathbf{x}) \rangle = \int f(\mathbf{x}')W(\mathbf{x} - \mathbf{x}', h)d\mathbf{x}' \quad (4.2)$$

where W is an interpolating kernel or smoothing function, \mathbf{x} is the 3-D position vector, $d\mathbf{x}'$ is a volume, and h is the smoothing length. It has been shown that the above approximation has accuracy of the order of $h^2\nabla^2 f$ [45].

The interpolating kernel W is similar to a weight function, and must satisfy the following two conditions:

$$\int W(\mathbf{x} - \mathbf{x}', h) d\mathbf{x}' = 1 \quad (4.3)$$

$$\lim_{h \rightarrow 0} W(\mathbf{x} - \mathbf{x}', h) = \delta(\mathbf{x} - \mathbf{x}'). \quad (4.4)$$

The interaction between the random set of particles is weighted by the interpolating kernel W .

For numerical computations, the discrete kernel approximation of $\langle f(\mathbf{x}) \rangle$ can be written as

$$\langle f(\mathbf{x}) \rangle = \sum_{k=1}^N m_k \frac{f_k}{\rho_k} W(\mathbf{x} - \mathbf{x}_k, h) \quad (4.5)$$

where \mathbf{x}_k is the centroid of a particle k with mass m_k and density ρ_k . N is the number of particles that fall within the smoothing length. In the above formulation, each particle is assumed to be a small volume element. Figure 4.5 shows the particle neighborhood for particle k as a circle of radius $2h$. Within this circular neighborhood, it is usually assumed that there is one SPH particle for an approximate spacing of the parameter h .

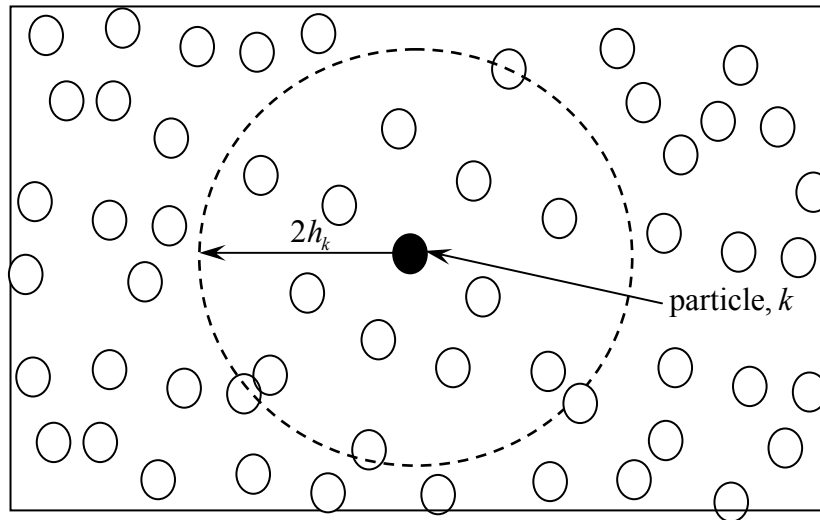


Figure 4.5. Particle neighborhood for SPH particle k .

In the SPH methodology, the spatial gradient ∇f is obtained from

$$\nabla f(\mathbf{x}) = \sum_{k=1}^N m_k \frac{f_k}{\rho_k} \nabla W(\mathbf{x} - \mathbf{x}_k, h). \quad (4.6)$$

However, Monaghan [44] suggests the following form for ∇f for improved accuracy:

$$\nabla f(\mathbf{x}) = \frac{1}{\rho} (\nabla(\rho f) - f \nabla \rho). \quad (4.7)$$

Note that the above formulation is obtained from the product rule of differentiation.

Similarly, the divergence of velocity $\nabla \cdot \mathbf{v}$ can be written as

$$\nabla \cdot \mathbf{v} = \frac{1}{\rho} (\nabla \cdot (\rho \mathbf{v}) - \mathbf{v} \cdot \nabla \rho). \quad (4.8)$$

The discrete kernel approximation of $\nabla \cdot \mathbf{v}$, now follows from equation (4.6):

$$(\nabla \cdot \mathbf{v})_i = \frac{1}{\rho_i} \sum_{k=1}^N (\mathbf{v}_k - \mathbf{v}_i) \cdot \nabla_i W_{ik} \quad (4.9)$$

where $\nabla_i W_{ik}$ refers to the gradient of W taken with respect to particle i .

Now, using the definitions presented above, the conservation equations of continuum mechanics can be written in the SPH formulation [46] as follows:

Continuity or conservation of mass:

$$\frac{d\rho_i}{dt} = \sum_{k=1}^N m_k (\mathbf{v}_k - \mathbf{v}_i) \cdot \nabla_i W_{ik} \quad (4.10)$$

Conservation of linear momentum:

$$\frac{d\mathbf{v}_i}{dt} = - \sum_{k=1}^N m_k \left(\frac{\boldsymbol{\sigma}_i}{\rho_i^2} + \frac{\boldsymbol{\sigma}_k}{\rho_k^2} \right) \cdot \nabla W_{ik} \quad (4.11)$$

Conservation of energy:

$$\frac{dE_i}{dt} = - \sum_{k=1}^N m_k (\mathbf{v}_k - \mathbf{v}_i) \cdot \left(\frac{\boldsymbol{\sigma}_i}{\rho_i^2} \right) \cdot \nabla W_{ik}. \quad (4.12)$$

The value of the interpolating kernel, or the smoothing function W varies in the neighborhood shown in Figure 4.5 of an SPH particle k . The value of W is at its maximum when $h \rightarrow 0$, and rapidly falls off as the boundary of the neighborhood is approached. In other words, interpolating kernel W has a compact support. The most common interpolating kernel used is the B-spline. The values of W based on the B-spline are

$$W(\nu, h) = \frac{1}{\pi h^3} \begin{cases} \left(1 - \frac{3}{2}\nu^2 + \frac{3}{4}\nu^3\right) & 0 < \nu < 1 \\ \frac{1}{4}(2 - \nu)^3 & 1 < \nu < 2 \\ 0 & \text{otherwise} \end{cases} \quad (4.13)$$

where $\nu = \frac{|\mathbf{x}_j - \mathbf{x}_k|}{h}$.

Smoothing length h varies during the course of a computation to ensure the availability of enough particles in the neighborhood of SPH particle k . Smoothing length h is a function of spatial dimension and time. It is computed from

$$\frac{dh}{dt} = \frac{1}{h} \nabla \cdot \mathbf{v} . \quad (4.14)$$

The SPH formulation was integrated into the LS-Dyna code by Lacombe [46]. Neighbor search is an important part of the SPH formulation. In LS-Dyna, the bucket sort algorithm is used to accomplish this task.

The SPH technique is becoming increasingly popular among bird strike researchers because numerical problems like mesh distortion do not exist when a structure is modeled with the SPH method. References [47, 48] are some examples of the previous work that used the SPH technique.

CHAPTER 5

NUMERICAL METHOD

Spatial and temporal resolution is an important aspect of numerical simulation of large deformation, finite strain, transient impact problems such as bird strike analyses. Most of the current-generation commercial computer codes used for bird strike simulation have their roots in the early codes developed for analyzing the impact problems associated with military aircraft. The foundations for these numerical codes, known as hydrocodes or wavecodes, were developed in the early 1960s through 1980s in U.S. defense laboratories. These hydrocodes have certain similarities to the Eulerian codes used in computational fluid dynamics (CFD) analyses. Both hydrocodes and the Eulerian codes make use of an equation of state relating the internal energy to pressure, volume and density of the material. The main difference with hydrocodes is that they take the material strength into account, similar to structural analysis codes. In contrast to the structural analysis codes, however, hydrocodes divide the Cauchy stress tensor σ_{ij} into the deviatoric stress component s_{ij} and the hydrostatic stress component p . The Cauchy stress tensor is decomposed into deviatoric and hydrostatic stress components to account for the plastic deformation of the material modeled with the hydrocodes. That is, most plasticity theories postulate that the plastic behavior of a material is independent of the hydrostatic stress component, and thus primarily depends on the deviatoric stress component.

In 3-D cartesian coordinates, the Cauchy stress tensor, in the absence of body couples, can be written as

$$[\boldsymbol{\sigma}] = \begin{bmatrix} \sigma_{xx} & \sigma_{xy} & \sigma_{xz} \\ \sigma_{xy} & \sigma_{yy} & \sigma_{yz} \\ \sigma_{xz} & \sigma_{yz} & \sigma_{zz} \end{bmatrix} = [\boldsymbol{\sigma}]_d + [\boldsymbol{\sigma}]_m \quad (5.1)$$

where $[\sigma]_d$ is the deviatoric part, and $[\sigma]_m$ is the hydrostatic or mean stress part; and these are given by:

$$[\sigma]_d = \begin{bmatrix} \sigma_{xx} - \sigma_m & \sigma_{xy} & \sigma_{xz} \\ \sigma_{xy} & \sigma_{yy} - \sigma_m & \sigma_{yz} \\ \sigma_{xz} & \sigma_{yz} & \sigma_{zz} - \sigma_m \end{bmatrix} = s_{ij} \quad (5.2)$$

and

$$[\sigma]_m = \begin{bmatrix} \sigma_m & 0 & 0 \\ 0 & \sigma_m & 0 \\ 0 & 0 & \sigma_m \end{bmatrix} \quad (5.3)$$

where σ_m is the mean stress given by:

$$\sigma_m = \frac{\sigma_{xx} + \sigma_{yy} + \sigma_{zz}}{3} = -p \quad (5.4)$$

and p is the hydrostatic pressure.

None of these details about the specific computational methods for hydrocodes are explicit in the open literature. Most developers of these hydrocodes, including the developers of the LS-Dyna code, later consolidated them into commercial software. Owing to their early development in defense laboratories, most information about the underlying computational methods is buried in the archives of government laboratories in the form of restricted reports, most of which are still inaccessible to the general public 40 years after their development. At the same time, commercial codes such as LS-Dyna have proprietary restrictions in place to protect their trade secrets.

In addition, most published bird strike work uses in-house codes or commercial codes that are publicly available – such as LS-Dyna, PAM-CRASH, MSC-DYTRAN, PW/WHAM, ADINA, MARC, MAGNA, all of them equally opaque to the user. Consequently, most of these

technical papers say nothing about the computational techniques, or even mention their use of hydrocode methods. Instead, they simply state the various modeling options pertaining to the software that was used for the numerical simulation [2 – 4, 15 – 17, 20, 24, 35, 49 – 59]. Indeed, for an analyst intending to understand the fundamentals of the underlying computational method, very few references are available; and those references remain obscure because their terminologies are unfamiliar to bird strike analysts. In particular, an analyst is highly unlikely to associate the term, “hydrocode”, with the problem of bird strike analysis. Fortunately, a thorough search of the literature on impact analysis turned up an important paper by Benson [7], who worked on the LS-Dyna codes, that contains an elaborate and detailed overview of the computational methods for the Lagrangian and Eulerian hydrocodes.

This chapter provides key details of the numerical method used in this work. While the methodology presented here may not exactly match that of the proprietary LS-Dyna software used for this research, it is representative of the state-of-the-art at the time when the current LS-Dyna codes were written, and is a close approximation that aids the understanding of the fundamentals of the numerical method. Most of the content of the current chapter follows the published work of Benson [7] with additional details from other references that will be noted. Only the computational methods relevant to the Lagrangian technique are included here, because both the impacted structure and the bird models are based on the Lagrangian formulation.

5.1 Central Difference Scheme for Explicit Time Integration

LS-Dyna uses the explicit central difference method of second-order accuracy to advance the solution in time. Central difference approximation of any function f can be obtained from the Taylor series approximation. The Taylor series approximation of any function f at times $t + \Delta t$ and $t - \Delta t$ can be written as follows:

$$f(t + \Delta t) = f(t) + \Delta t \frac{\partial f}{\partial t} + \frac{(\Delta t)^2}{2!} \frac{\partial^2 f}{\partial t^2} + \frac{(\Delta t)^3}{3!} \frac{\partial^3 f}{\partial t^3} + (\text{H.O.T.}) \quad (5.5)$$

$$f(t - \Delta t) = f(t) - \Delta t \frac{\partial f}{\partial t} + \frac{(\Delta t)^2}{2!} \frac{\partial^2 f}{\partial t^2} - \frac{(\Delta t)^3}{3!} \frac{\partial^3 f}{\partial t^3} + (\text{H.O.T.}). \quad (5.6)$$

Using equations (5.5) and (5.6), the value of a function at times t^n and t^{n+1} can be written as follows:

$$f^n = f^{n+\frac{1}{2}} - \frac{\Delta t^{n+\frac{1}{2}}}{2} f_{,t}^{n+\frac{1}{2}} + \frac{\left(\Delta t^{n+\frac{1}{2}}\right)^2}{2!} f_{,tt}^{n+\frac{1}{2}} - \frac{\left(\Delta t^{n+\frac{1}{2}}\right)^3}{3!} f_{,ttt}^{n+\frac{1}{2}} + (\text{H.O.T.}) \quad (5.7)$$

$$f^{n+1} = f^{n+\frac{1}{2}} + \frac{\Delta t^{n+\frac{1}{2}}}{2} f_{,t}^{n+\frac{1}{2}} + \frac{\left(\Delta t^{n+\frac{1}{2}}\right)^2}{2!} f_{,tt}^{n+\frac{1}{2}} + \frac{\left(\Delta t^{n+\frac{1}{2}}\right)^3}{3!} f_{,ttt}^{n+\frac{1}{2}} + (\text{H.O.T.}). \quad (5.8)$$

In the above equations, the subscript $[,t]$ refers to differentiation with respect to time.

Now, subtracting equation (5.7) from equation (5.8), we obtain,

$$f^{n+1} = f^n + \Delta t^{n+\frac{1}{2}} f_{,t}^{n+\frac{1}{2}} + (\text{H.O.T.}). \quad (5.9)$$

Equation (5.9) is second-order accurate, since the terms neglected in the approximation are of third-order and higher.

Note that in the Lagrangian hydrocodes the time step Δt is not fixed, but is variable, and hence the need for a superscript that refers to the specific time level on Δt . Recall that in the Lagrangian technique, the mesh is attached to the structure and deforms with the structure. Therefore, in order to meet the CFL criteria for stability of the explicit time integration scheme as explained in Chapter 3, the size of time step should be continuously adjusted as the mesh deforms.

The time step $\Delta t^{n+\frac{1}{2}}$ appearing in the above equations is defined by the following:

$$\Delta t^{n+\frac{1}{2}} = t^{n+1} - t^n. \quad (5.10)$$

In addition, the following expressions for Δt^n and $t^{n+\frac{1}{2}}$ will be used throughout this chapter:

$$\Delta t^n = t^{n+\frac{1}{2}} - t^{n-\frac{1}{2}} \quad (5.11)$$

$$t^{n+\frac{1}{2}} = \frac{1}{2}(t^{n+1} + t^n). \quad (5.12)$$

Now, using equation (5.9), the displacement \mathbf{d} at time level $n+1$ can be written as

$$\mathbf{d}^{n+1} = \mathbf{d}^n + \Delta t^{n+\frac{1}{2}} \mathbf{v}^{n+\frac{1}{2}}. \quad (5.13)$$

Using the same procedure, the velocity \mathbf{v} can be obtained from

$$\mathbf{v}^{n+\frac{1}{2}} = \mathbf{v}^{n-\frac{1}{2}} + \Delta t^n \mathbf{a}^n. \quad (5.14)$$

Notice that the velocity \mathbf{v} is staggered in time, or is computed at the mid-points of the time intervals.

The acceleration \mathbf{a} is computed from equation (3.22), which is repeated below for convenience.

$$\mathbf{M}_{KL} \mathbf{a}_{iL} = \mathbf{F}_{iK}^{ext} - \mathbf{F}_{iK}^{int} \quad (3.22)$$

The external forces \mathbf{F}_{iK}^{ext} may be specified as a function of nodal displacements and time.

The internal forces \mathbf{F}_{iK}^{int} can be evaluated from the strain-displacement equations and the constitutive equations.

5.2 Mass Matrix, \mathbf{M}

As was explained in Chapter 3, if the time integration scheme is explicit, then the solution does not require solving a set of simultaneous equations. This statement is true provided the mass matrix \mathbf{M} used in the explicit time integration is diagonal. However, in finite element

formulations based on the weak form, the mass matrix \mathbf{M} is computed using the same shape functions as those used in the formulation of the nodal displacements. Such a mass matrix, computed based on shape functions is called a consistent mass matrix, and is given by

$$\mathbf{M}_C = \int_V \rho \mathbf{N}^T \mathbf{N} dV \quad (5.15)$$

where V is volume.

The consistent mass matrix is not diagonal, and this leads to equations of motion that contradict Newton's second law due to the fact that when $M_{ij} \neq 0$, the mass at node i causes acceleration at node j [30]. In addition, a non-diagonal mass matrix results in coupled equations in equation (3.22), which are computationally "expensive" to solve. Therefore, it is computationally beneficial to use a diagonal approximation to the non-diagonal, consistent mass matrix. Such a diagonal mass matrix is known as a lumped mass matrix. There is no general procedure for formulating a lumped mass matrix. Various researchers used formulas with varying degree of simplicity, one of which is

$$M_{\alpha i \beta j} = \delta_{\alpha \beta} \delta_{ij} \frac{1}{n} \sum_A M_A. \quad (5.16)$$

In equation (5.16), the mass of an element A is M_A . αi refers to the i th displacement component of node α , and βj refers to the j th displacement component of node β . n refers to the total number of nodes of element A , and the summation includes only the elements that have the node α in their definition.

Another method of computing the diagonal lumped mass matrix is given by

$$M_{ii}^D = \sum_j M_{ij}^C \quad (5.17)$$

where the summation is over the entire row of the consistent mass matrix M_{ij}^C .

Yet another variation in the computation of the diagonal lumped mass matrix is given below:

$$M_{ii}^D = \int_{X_a}^{X_b} \rho_0 N_i \left(\sum_j N_j \right) A_0 dX = \int_{X_a}^{X_b} \rho_0 N_i A_0 dX. \quad (5.18)$$

The above equation uses the fact that the sum of the shape functions over an element must equal to 1.

5.3 Solution Methodology

The general solution procedure, or numerical algorithm, for a typical Lagrangian hydrocode is presented in this section. Some of the steps will be discussed in detail in following sections.

1. Initialize the solution procedure by applying the initial conditions.
2. Knowing the stress, pressure, hourglass forces, and artificial shock viscosity in each element at time t^n , compute the forces.
3. Knowing the nodal force matrix and nodal mass matrix, compute the nodal accelerations \mathbf{a}^n at time t^n .
4. Integrate the nodal accelerations \mathbf{a}^n to compute the mid-point nodal velocities from

$$\mathbf{v}^{n+\frac{1}{2}} = \mathbf{v}^{n-\frac{1}{2}} + \Delta t^n \mathbf{a}^n.$$

5. Compute the nodal displacements \mathbf{d}^{n+1} at time level $n+1$ by integrating the velocities

$$\text{using } \mathbf{d}^{n+1} = \mathbf{d}^n + \Delta t \frac{1}{2} \mathbf{v}^{n+\frac{1}{2}}.$$

6. Compute the rate of deformation and other strain rate measures $\dot{\boldsymbol{\epsilon}}^{n+\frac{1}{2}}$ from the velocities

$$\mathbf{v}^{n+\frac{1}{2}}.$$

7. Compute the stresses at time level $n + 1$ by integrating the constitutive model for strength from t^n to t^{n+1} .
8. Compute the artificial shock viscosity and the hourglass forces from the velocities $\mathbf{v}^{n+\frac{1}{2}}$.
9. Update the internal energy based on the work done from t^n to t^{n+1} .
10. Compute the pressure at $n + 1$ from the equation of state knowing the density and energy at $n + 1$.
11. Update the time step size taking the CFL stability criterion into consideration.
12. Advance the time, and return to step 2.

5.4 Strain Rate

In nonlinear continuum mechanics, the strain measure must include the rigid body motion of the body under consideration in addition to the usual deformations of linear elasticity. Therefore, any strain measure used in nonlinear continuum mechanics must vanish for rigid body rotation. Belytschko [30] proves that the strain measure used in linear elasticity fails to meet this requirement and predicts non-zero strain during rigid body rotation, and thus gives non-zero stresses in rigid body rotation.

Many strain measures are proposed by various researchers for use in nonlinear continuum mechanics. The rate of deformation tensor D_{ij} introduced in Chapter 3 is one such measure. Another strain measure that is typically used in many Lagrangian hydrocodes is the Green or the Green-Lagrange strain tensor E_{ij} .

5.4.1 Green Strain Tensor

The Green strain tensor \mathbf{E} is defined by

$$ds^2 - dS^2 = 2d\mathbf{X} \cdot \mathbf{E} \cdot d\mathbf{X}, \quad (5.19)$$

or in tensor formulation

$$dx_i dx_i - dX_i dX_i = 2dX_i E_{ij} dX_j. \quad (5.20)$$

In the above equations, ds and dS refers to a vector length of an infinitesimal line segment in the current and reference configurations, respectively; and similarly, dx_i and dX_i refer to the same vector in the current and reference configurations.

Therefore, the Green strain tensor \mathbf{E} measures the difference in the square of the length of an infinitesimal line segment in the current and the reference configurations. The Green strain tensor \mathbf{E} can also be written [30] as

$$\mathbf{E} = \frac{1}{2}(\mathbf{F}^T \cdot \mathbf{F} - \mathbf{I}), \quad (5.21)$$

or in tensor notation

$$E_{ij} = \frac{1}{2}(F_{ik}^T F_{kj} - \delta_{ij}). \quad (5.22)$$

Recall that \mathbf{F} or F_{ij} refers to the deformation gradient given by

$$F_{ij} = \frac{\partial x_i}{\partial X_j}. \quad (5.23)$$

5.4.2 Rate of Deformation Tensor

Recall that the definition of the rate of deformation tensor \mathbf{D} which was first introduced in Chapter 3, is

$$D_{ij} = \frac{1}{2}(L_{ij} + L_{ji}) \quad (5.24)$$

where the velocity gradient \mathbf{L} is defined as

$$L_{ij} = \frac{\partial v_i}{\partial x_j}. \quad (5.25)$$

The rate of deformation tensor is also called the velocity strain.

5.5 Stress Rate

Similar to the different strain measures used for nonlinear continuum mechanics, we need to define a new set of stress rates for use in nonlinear continuum mechanics. Consider the following Cauchy stress tensor in a rotated coordinate system,

$$\sigma_{ij}^* = Q_{ik} \sigma_{kl} Q_{lj} \quad (5.26)$$

where \mathbf{Q} is the transformation matrix.

In the above equation, the Cauchy stress tensor σ_{ij} follows the tensor transformation law.

Now, if we take material time derivative of the rotated Cauchy stress tensor σ_{ij}^* we obtain

$$\dot{\sigma}_{ij}^* = \dot{Q}_{ik} \sigma_{kl} Q_{lj} + Q_{ik} \dot{\sigma}_{kl} Q_{lj} + Q_{ik} \sigma_{kl} \dot{Q}_{lj}. \quad (5.27)$$

In the above equation, the material time derivative of a rotated Cauchy stress tensor includes the time derivatives of the transformation matrix \mathbf{Q} . Therefore, the material time derivative of a rotated Cauchy stress tensor does not transform properly or objectively. A modification to the stress rate is needed to make it frame invariant. Such a stress rate is called an objective stress rate, or a frame-invariant stress rate. An objective stress rate inherently accounts for the rigid body rotation.

Three different objective stress rates are frequently used in Lagrangian hydrocodes.

These include the Jaumann rate, the Truesdell rate and the Green-Nagdhi rate.

5.5.1 Jaumann Rate

The Jaumann rate of the Cauchy stress is given by

$$\sigma^{\nabla J} = \frac{D\sigma}{Dt} - \mathbf{W} \cdot \sigma - \sigma \cdot \mathbf{W}^T, \quad (5.28)$$

or in tensor formulation

$$\sigma_{ij}^{\nabla J} = \frac{D\sigma_{ij}}{Dt} - W_{ik}\sigma_{kj} - \sigma_{ik}W_{kj}^T \quad (5.29)$$

where \mathbf{W} in the above equations is the vorticity or the spin tensor, given by

$$W_{ij} = \frac{1}{2}(L_{ij} - L_{ji}). \quad (5.30)$$

Therefore, the material rate for the Cauchy stress tensor $\boldsymbol{\sigma}$ has contributions from the rate of change due to material response; and that due to the rigid body rotation as given below [30]:

$$\frac{D\boldsymbol{\sigma}}{Dt} = \boldsymbol{\sigma}^{\nabla J} + \mathbf{W} \cdot \boldsymbol{\sigma} + \boldsymbol{\sigma} \cdot \mathbf{W}^T = \underbrace{\mathbf{C}^{\alpha J} : \mathbf{D}}_{\text{material}} + \underbrace{\mathbf{W} \cdot \boldsymbol{\sigma} + \boldsymbol{\sigma} \cdot \mathbf{W}^T}_{\text{rotational}} \quad (5.31)$$

where \mathbf{C} is the material tangent modulus tensor.

5.5.2 Treusdell Rate

The Treusdell rate is given by

$$\boldsymbol{\sigma}^{\nabla T} = \frac{D\boldsymbol{\sigma}}{Dt} - (\nabla \cdot \mathbf{v})\boldsymbol{\sigma} - \mathbf{L} \cdot \boldsymbol{\sigma} - \boldsymbol{\sigma} \cdot \mathbf{L}^T. \quad (5.32)$$

The Treusdell rate is obtained by differentiating the Cauchy stress expressed in terms of the second Piola-Kirchhoff stress tensor \mathbf{S} which is given by

$$\mathbf{S} = J\mathbf{F}^{-1} \cdot \boldsymbol{\sigma} \cdot \mathbf{F}^{-T}. \quad (5.33)$$

5.5.3 Green-Nagdhi Rate

The Green-Nagdhi rate is given by

$$\boldsymbol{\sigma}^{\nabla G} = \frac{D\boldsymbol{\sigma}}{Dt} - \boldsymbol{\Omega} \cdot \boldsymbol{\sigma} - \boldsymbol{\sigma} \cdot \boldsymbol{\Omega}^T \quad (5.34)$$

where $\boldsymbol{\Omega}$ is the angular velocity vector given by

$$\boldsymbol{\Omega} = \dot{\mathbf{R}} \cdot \mathbf{R}^T. \quad (5.35)$$

The Green-Nagdhi rate is obtained by differentiating the expression for Cauchy stress expressed in terms of the rotated Cauchy stress, also known as the corotational Cauchy stress $\hat{\boldsymbol{\sigma}}$ given by

$$\hat{\boldsymbol{\sigma}} = \mathbf{R}^T \cdot \boldsymbol{\sigma} \cdot \mathbf{R} . \quad (5.36)$$

The orthogonal rotation matrix \mathbf{R} appearing in the above equation, can be obtained by applying the polar decomposition theorem to the deformation gradient tensor \mathbf{F} as follows

$$\mathbf{F} = \mathbf{R} \cdot \mathbf{U} \quad (5.37)$$

where \mathbf{U} is a symmetric tensor. Therefore, $\mathbf{R}^{-1} = \mathbf{R}^T$ and $\mathbf{U} = \mathbf{U}^T$.

5.6 Stress Update

After computing the stress rate, the stress tensor at time level $n + 1$ can be updated by using the following equation:

$$\sigma_{ij}^{n+1} = \sigma_{ij}^n + \dot{\sigma}_{ij}^{n+\frac{1}{2}} \Delta t^{n+\frac{1}{2}} . \quad (5.38)$$

Using the Jaumann stress rate, the above equation can be rewritten as

$$\sigma_{ij}^{n+1} = \sigma_{ij}^n + C_{ijkl} \dot{\epsilon}_{ij}^{n+\frac{1}{2}} \Delta t^{n+\frac{1}{2}} + r_{ij}^n \quad (5.39)$$

where

$$r_{ij}^n = \left(\sigma_{ip}^n w_{pj}^{n+\frac{1}{2}} + \sigma_{jp}^n w_{pi}^{n+\frac{1}{2}} \right) \Delta t^{n+\frac{1}{2}} . \quad (5.40)$$

Both equations (5.39) and (5.40) follow from equation (5.31).

5.7 Computation of Pressure

In Lagrangian hydrocodes, the pressure is computed from an equation of state. The equation of state is a thermodynamic relationship between pressure, the density (or relative volume) and internal energy (or temperature). Therefore, pressure can be expressed as

$$p = p(V, E) = p(V, T) . \quad (5.41)$$

The energy computation treats the work associated with the deviatoric part of the stress vector separately from that associated with the pressure. In addition, the contribution from the shock viscosity q is separated into its deviatoric and mean components.

It may be recalled that the stress tensor in hydrocodes is divided into the deviatoric and the hydrostatic components as below:

$$\sigma_{ij} = s_{ij} - \delta_{ij}p \quad (5.42)$$

where s_{ij} and p are the deviatoric and the pressure, respectively. The negative sign in front of pressure p in equation (5.42) is due to the fact that pressure is positive in compression, and Cauchy stress is positive in tension.

The term δ_{ij} appearing in equation (5.42), is the kronecker delta, given by

$$\delta_{ij} \equiv \begin{cases} 0 & \text{for } i \neq j \\ 1 & \text{for } i = j \end{cases} \quad (5.43)$$

Also, the strain rate tensor $\dot{\varepsilon}_{ij}$ can be written as

$$\dot{\varepsilon}_{ij} = \dot{\varepsilon}'_{ij} + \frac{1}{3}\delta_{ij}\text{tr}(\dot{\varepsilon}_{ij}) \quad (5.44)$$

where $\dot{\varepsilon}'_{ij}$ is the deviatoric part of strain rate and $\frac{1}{3}\delta_{ij}\text{tr}(\dot{\varepsilon}_{ij})$ is the mean strain rate.

The mean strain rate can also be expressed as

$$\frac{1}{3}\delta_{ij}\text{tr}(\dot{\varepsilon}_{ij}) = \frac{(\Delta\dot{V})}{V} \quad (5.45)$$

where V is volume and $\Delta\dot{V}$ is rate of change of volume.

Similarly, the artificial shock viscosity q can be written as

$$q = q' + \frac{1}{3}\delta_{ij}\text{tr}(q) \quad (5.46)$$

where q' is the deviatoric part and $\frac{1}{3}\delta_{ij}\text{tr}(q)$ is the mean shock viscosity.

Using the above equations, the rate of total internal energy per unit volume can be written as

$$\rho\dot{e} = \sigma_{ij}\dot{\epsilon}_{ij} = \left(s_{ij} - \delta_{ij}p + q' + \frac{1}{3}\text{tr}(q)\delta_{ij} \right) \left(\dot{\epsilon}'_{ij} + \frac{1}{3}\text{tr}(\dot{\epsilon}'_{ij})\delta_{ij} \right). \quad (5.47)$$

The above equation can be simplified by using equation (5.45) as follows:

$$\dot{E} = V(s_{ij} + q')\dot{\epsilon}'_{ij} + \left(\frac{1}{3}\text{tr}(q) - p \right) (\Delta\dot{V}) \quad (5.48)$$

where \dot{E} is the rate of total internal energy.

Now, the total internal energy E at time level $n+1$ can be computed from

$$E^{n+1} = E^n + \dot{E}^{n+\frac{1}{2}}\Delta t^{n+\frac{1}{2}} \quad (5.49)$$

which can be written as

$$E^{n+1} = E^n + \Delta t^{n+\frac{1}{2}} V^{n+\frac{1}{2}} \left(s_{ij}^{n+\frac{1}{2}} + q'^{n+\frac{1}{2}} \right) \dot{\epsilon}'_{ij}{}^{n+\frac{1}{2}} + \left(\frac{1}{3}\text{tr}(q^{n+\frac{1}{2}}) - p^{n+\frac{1}{2}} \right) \Delta V^{n+\frac{1}{2}} \quad (5.50)$$

where

$$\begin{aligned} V^{n+\frac{1}{2}} &= \frac{1}{2}(V^{n+1} + V^n), & s_{ij}^{n+\frac{1}{2}} &= \frac{1}{2}(s_{ij}^{n+1} + s_{ij}^n), \\ q'^{n+\frac{1}{2}} &= \frac{1}{2}(q'^{n+1} + q'^n), & q^{n+\frac{1}{2}} &= \frac{1}{2}(q^{n+1} + q^n), \\ p^{n+\frac{1}{2}} &= \frac{1}{2}(p^{n+1} + p^n). \end{aligned} \quad (5.51)$$

Recall that the strain rates $\dot{\epsilon}$ are computed at $n + \frac{1}{2}$ based on the velocity vector \mathbf{v} which is

computed at $n + \frac{1}{2}$.

In equation (5.50), in order to calculate E^{n+1} we first need to know p^{n+1} , which is also a function of E^{n+1} . Therefore, equation (5.50) is implicit in energy. Equation (5.50) can be rewritten such that all known contributions to energy at time level $n + 1$ are grouped into an intermediate energy term \tilde{E} as follows:

$$E^{n+1} = \tilde{E} - \frac{1}{2} \Delta V^{n+\frac{1}{2}} p^{n+1} (E^{n+1}, \rho^{n+1}). \quad (5.52)$$

Most equations of state, typically are linear in internal energy. Therefore, p^{n+1} can be written as

$$p^{n+1} = A^{n+1} + B^{n+1} E^{n+1} \quad (5.53)$$

which leads to the following expression for p^{n+1} :

$$p^{n+1} = \frac{A^{n+1} + B^{n+1} \tilde{E}}{1 + \frac{1}{2} \Delta V^{n+\frac{1}{2}} B^{n+1}}. \quad (5.54)$$

Now, using the value of p^{n+1} , the energy E^{n+1} can be updated from equation (5.52).

A difficulty arises when the equation of state is not a linear function in internal energy. In such a case, a one-step iteration is used to compute an intermediate pressure value p^{*n+1} from the following expression:

$$p^{*n+1} = p(\rho^{n+1}, \tilde{E}). \quad (5.55)$$

Now the internal energy E^{n+1} is updated from equation (5.52), by substituting p^{*n+1} for p^{n+1} .

Using the computed value of E^{n+1} , the pressure p^{n+1} is updated from equation (5.55) by

replacing \tilde{E} with E^{n+1} .

5.8 Artificial Viscosity

In Lagrangian hydrocodes, an artificial viscous term q is added to the pressure in both the momentum and energy equations to treat shock waves. Inclusion of a viscous term q automatically smears the shock discontinuities, and eliminates weak, numerical (non-physical) solutions that may exist in the presence of shocks. VonNeumann and Richtmyer [60] first introduced the following form for the viscous term in 1-D numerical calculation of hydrodynamic shocks:

$$q = C_0 \rho (\Delta x)^2 \left(\frac{\partial v}{\partial x} \right)^2 \quad (5.56)$$

where C_0 is a non-dimensional constant and Δx is the mesh spacing.

It can be seen that the artificial viscosity term is quadratic in strain rate. This viscous term is added in the compression region, and is set to zero everywhere else.

Typically, most hydrocodes include a linear term in addition to the quadratic term shown in equation (5.56), resulting in

$$q = C_0 \rho (\Delta v)^2 + C_l a \rho \Delta v \quad (5.57)$$

where C_l is another non-dimensional constant and a is the local speed of sound.

In multi-dimensional problems, LS-Dyna defines the artificial viscous term q as follows:

$$\begin{aligned} q &= \rho l (C_0 l \dot{\epsilon}_{kk}^2 - C_l a \dot{\epsilon}_{kk}) & \text{for } \dot{\epsilon}_{kk} < 0 \\ q &= 0 & \text{for } \dot{\epsilon}_{kk} \geq 0 \end{aligned} \quad (5.58)$$

where $\dot{\epsilon}_{kk} = \text{tr}(\dot{\epsilon}_{ijk})$, and l is the characteristic length, equal to the square root of the area in 2-D, and the cubic root of the volume in 3-D. The default values of the non-dimensional constants, C_0 and C_l , are 1.5 and 0.06, respectively.

5.9 Energy Balance

Energy balance must be checked in nonlinear finite element codes in order to detect instabilities that develop in the solutions. In linear elasticity, instabilities in the solution are obvious because they grow unbounded. In nonlinear finite element solutions, however, there are phenomena that can mask the instabilities. One such numerical phenomenon, “arrested instability,” was reported by Belytschko [61]. This instability results from geometric stiffening in an elastic material, which leads to local exponential growth in internal loads, causing local plastic behavior, which effectively softens the material. This softening of the material reduces the local wave speed, which restabilizes the solution. However, displacements are over-predicted in such cases, and the error in the solution will not be found unless an energy balance is conducted. These instabilities are detected by an energy balance check because they generate spurious energy that violates the law of conservation of energy.

The energy conservation is satisfied when the following condition is met [30]:

$$|W_{\text{kinematic}} + W_{\text{internal}} - W_{\text{external}}| \leq \varepsilon \max(W_{\text{kinematic}}, W_{\text{internal}}, W_{\text{external}}) \quad (5.59)$$

where the allowable threshold level of ε is on the order of 10^{-2} .

Note that in computational continuum mechanics, energy balance depends on the chosen numerical algorithm. Recall that in Lagrangian hydrocodes, the internal energy is centered at time t^n , but the velocity, and thus the kinetic energy, are centered at time $t^{n+\frac{1}{2}}$. Therefore, the total energy balance is only an approximation, rather than exact.

5.10 Typical Element Formulation in FEM

In this section, the element formulation of a typical element in the finite element method is presented. Specifically, a 3-dimensional, 8-node hexahedron, isoparametric element, shown in Figure 5.1, was chosen because of the simplicity of its formulation.

Node	ξ	η	ζ
1	-1	-1	-1
2	1	-1	-1
3	1	1	-1
4	-1	1	-1
5	-1	-1	1
6	1	-1	1
7	1	1	1
8	-1	1	1

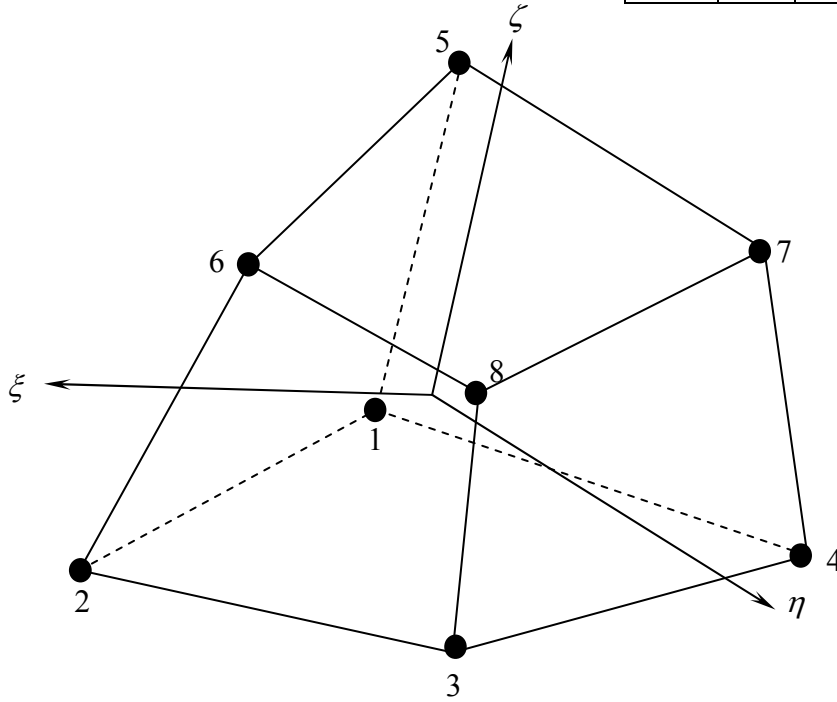


Figure 5.1. 8-Node hexahedron element.

In FEM, when the same interpolation formulas are used to define both the geometric and displacement shape functions, the resulting element formulation is referred to as an isoparametric formulation. The isoparametric coordinates, ξ , η , and ζ in Figure 5.1, range in value from -1 to +1. The shape functions ϕ_j for the 8-node hexahedron element are given by

$$\phi_j = \frac{1}{8}(1 + \xi\xi_j)(1 + \eta\eta_j)(1 + \zeta\zeta_j) \quad (5.60)$$

where ξ_j , η_j , and ζ_j are the nodal values of ξ , η , and ζ , respectively, and equal to ± 1 as shown in Figure 5.1.

The displacements x_i and the velocities v_i are given by

$$x_i = \sum_{j=1}^8 \phi_j(\xi, \eta, \zeta) x_i^j(t) \quad (5.61)$$

and

$$v_i = \sum_{j=1}^8 \phi_j(\xi, \eta, \zeta) v_i^j(t) \quad (5.62)$$

where t is time. Equations (5.61) and (5.62) can be written as

$$\mathbf{x} = \mathbf{N} \mathbf{x}_i \quad (5.63)$$

$$\mathbf{v} = \mathbf{N} \mathbf{v}_i \quad (5.64)$$

where \mathbf{N} is the 3 x 24 interpolation matrix given by

$$\mathbf{N}(\xi, \eta, \zeta) = \begin{bmatrix} \phi_1 & 0 & 0 & \phi_2 & 0 & \dots & 0 & 0 \\ 0 & \phi_1 & 0 & 0 & \phi_2 & \dots & \phi_8 & 0 \\ 0 & 0 & \phi_1 & 0 & 0 & \dots & 0 & \phi_8 \end{bmatrix}_{3 \times 24} \quad (5.65)$$

The next step is to compute the strain rate tensor, which is also equal to the rate of deformation tensor. Recall from Section 5.4 that the rate of deformation tensor is given by

$$D_{ij} = \frac{1}{2} (L_{ij} + L_{ji}) \quad (5.24)$$

where the velocity gradient \mathbf{L} is defined as

$$L_{ij} = \frac{\partial v_i}{\partial x_j} \quad (5.25)$$

Therefore, the strain rate vector $\dot{\boldsymbol{\epsilon}}$ can be written as

$$\dot{\boldsymbol{\epsilon}} = \mathbf{B} \mathbf{N} \quad (5.66)$$

where

$$\dot{\boldsymbol{\epsilon}} = \begin{Bmatrix} \dot{\epsilon}_{11} \\ \dot{\epsilon}_{22} \\ \dot{\epsilon}_{33} \\ \dot{\epsilon}_{12} \\ \dot{\epsilon}_{23} \\ \dot{\epsilon}_{31} \end{Bmatrix} \quad (5.67)$$

and \mathbf{B} is the strain-displacement matrix, given by

$$\mathbf{B}_{6 \times 24} = \begin{bmatrix} \frac{\partial}{\partial x} & 0 & 0 \\ 0 & \frac{\partial}{\partial y} & 0 \\ 0 & 0 & \frac{\partial}{\partial z} \\ \frac{\partial}{\partial y} & \frac{\partial}{\partial x} & 0 \\ 0 & \frac{\partial}{\partial z} & \frac{\partial}{\partial y} \\ \frac{\partial}{\partial z} & 0 & \frac{\partial}{\partial x} \end{bmatrix}_{6 \times 3} \mathbf{N}_{3 \times 24}. \quad (5.68)$$

The terms in the strain-displacement matrix \mathbf{B} are of the form $\frac{\partial \phi_i}{\partial x_j}$. Using the chain rule of

differentiation, $\frac{\partial \phi_i}{\partial x_j}$ can be written as

$$\frac{\partial \phi_i}{\partial x_j} = \frac{\partial \phi_i}{\partial \xi_k} \frac{\partial \xi_k}{\partial x_j}. \quad (5.69)$$

From equation (5.60), we can compute $\frac{\partial \phi_i}{\partial \xi_j}$ using the chain rule as follows:

$$\begin{Bmatrix} \frac{\partial \phi_i}{\partial \xi} \\ \frac{\partial \phi_i}{\partial \eta} \\ \frac{\partial \phi_i}{\partial \zeta} \end{Bmatrix} = \begin{bmatrix} \frac{\partial x}{\partial \xi} & \frac{\partial y}{\partial \xi} & \frac{\partial z}{\partial \xi} \\ \frac{\partial x}{\partial \eta} & \frac{\partial y}{\partial \eta} & \frac{\partial z}{\partial \eta} \\ \frac{\partial x}{\partial \zeta} & \frac{\partial y}{\partial \zeta} & \frac{\partial z}{\partial \zeta} \end{bmatrix} \begin{Bmatrix} \frac{\partial \phi_i}{\partial x} \\ \frac{\partial \phi_i}{\partial y} \\ \frac{\partial \phi_i}{\partial z} \end{Bmatrix}. \quad (5.70)$$

Now, $\frac{\partial \phi_i}{\partial x_j}$ can be computed from

$$\begin{Bmatrix} \frac{\partial \phi_i}{\partial x} \\ \frac{\partial \phi_i}{\partial y} \\ \frac{\partial \phi_i}{\partial z} \end{Bmatrix} = \mathbf{J}^{-1} \begin{Bmatrix} \frac{\partial \phi_i}{\partial \xi} \\ \frac{\partial \phi_i}{\partial \eta} \\ \frac{\partial \phi_i}{\partial \zeta} \end{Bmatrix} \quad (5.71)$$

where the Jacobian matrix \mathbf{J} is given by

$$\mathbf{J} = \begin{bmatrix} \frac{\partial x}{\partial \xi} & \frac{\partial y}{\partial \xi} & \frac{\partial z}{\partial \xi} \\ \frac{\partial x}{\partial \eta} & \frac{\partial y}{\partial \eta} & \frac{\partial z}{\partial \eta} \\ \frac{\partial x}{\partial \zeta} & \frac{\partial y}{\partial \zeta} & \frac{\partial z}{\partial \zeta} \end{bmatrix}. \quad (5.72)$$

Recall from Chapter 3 that when all the element matrices are assembled, we compute volume integrals of the form $\int_V g dV$. This volume integral can be rewritten as

$$\int_V g dV = \int_{-1}^{+1} \int_{-1}^{+1} \int_{-1}^{+1} g |\mathbf{J}| d\xi d\eta d\zeta. \quad (5.73)$$

For an isoparametric formulation, numerical integration is an inherent part of the matrix evaluations in FEM [62]. Numerical integration based on Gaussian quadrature can be used to compute the above integral as follows:

$$\int_V g dV = \sum_{i,j,k} \alpha_i \alpha_j \alpha_k g(\xi_i, \eta_j, \zeta_k) \quad (5.74)$$

where α_i , α_j , and α_k are the weight factors.

The evaluation of the integral in (5.74) would be exact when n Gauss integration points are used if $g(\xi_i, \eta_j, \zeta_k)$ is a polynomial of degree $2n - 1$. However, for computational savings, almost all numerical codes use reduced integration with fewer than n Gauss integration points.

5.11 Hourglass Modes

When reduced integration is used for the evaluation of the numerical integrals in the previous section, an instability is introduced into the solution. This instability manifests itself as spurious zero-frequency modes. Owing to their shape in 2-D elements, such modes are called hourglass modes, keystone modes, or spurious zero-energy modes. These modes are not resisted by the internal stresses in the element. For example, consider the case of a 4-noded 2-D element, which has 8 degrees of freedom (dofs). Three of the dofs are rigid body dofs – two translations and one rotation. These rigid body dofs should not be resisted by the internal stresses. That leaves 5 dofs to be resisted by the internal stresses. However, in 2-D, there are only three stress components. Therefore, there are two zero-energy modes for a 2-D quadrilateral element, which assume the shapes shown in Figure 5.2. Dashed line in Figure 5.2 represents the undeformed shape of the element. Similarly, in 3-D there are 12 hourglass modes for an 8-node hexahedron element.

In hourglass modes there is no strain at the centroid of the element, since the lines of constant ξ_i passing through the centroid remain undistorted. Typically, the hourglass modes tend to have periods shorter than the structural periods [21]. However, certain hourglass modes have periods that are comparable to the structural response periods, and must be admissible

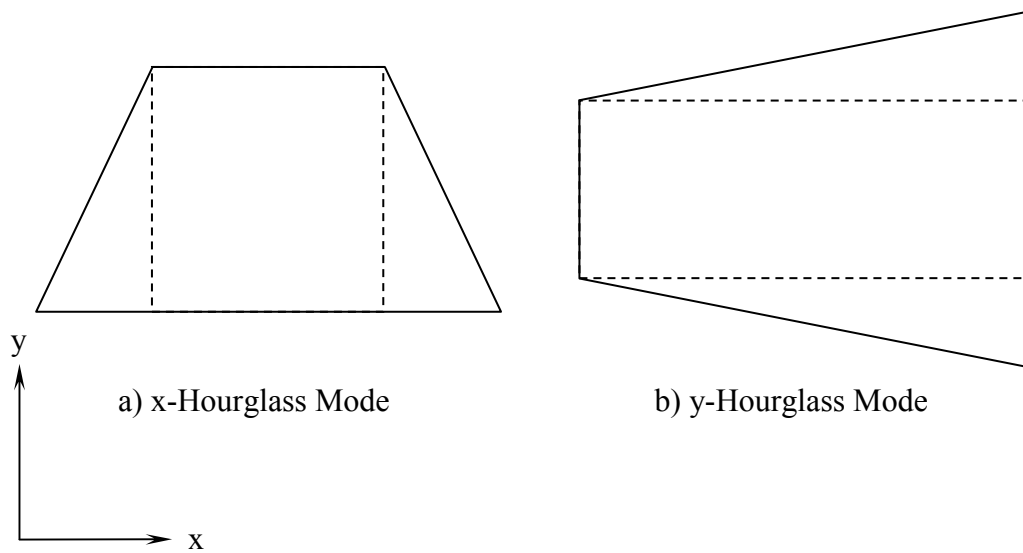


Figure 5.2. Hourglass modes for a 2-D quadrilateral element.

because these may be part of a stable kinematic component of the global deformation.

Instabilities in the form of hourglass modes can be damped out by adding artificial viscosity to the momentum equations. Benson [7] reports that the form these viscous damping terms is not critical for most problems.

Hourglass energy is not included in the energy balance because these modes are orthogonal to the structural response modes considered in the strain calculations. Therefore, a separate hourglass energy check needs to be performed to make sure that it is kept to a minimum.

CHAPTER 6

BIRD EQUATION OF STATE MODELS

Recall from Chapter 2 that the projectile impact behavior is categorized in terms of increasing impact speed as being elastic, plastic, hydrodynamic, sonic, or explosive [9]. At typical bird strike velocities, hydrodynamic behavior is considered to be the most representative of bird impact. High speed videos of bird strike tests visually confirm the fluid behavior of the bird at impact. Note that, as a simplification, the bird strike velocity is considered to be equal to the velocity of the aircraft, since the bird velocity is relatively small. A bird is described as a “soft body” material because the stresses generated during a bird strike are well beyond the strength of the bird, but are generally below the strength of the target material. Since the bird behaves like a fluid upon impact, the impact loads can be computed from an equation of state if the viscosity is neglected.

An equation of state is a thermodynamic relationship between the density or volume, internal energy or temperature, and pressure – such that the pressure P can be expressed as

$$P = P(V, E) = P(V, T) \quad (6.1)$$

where V , E , and T are volume, internal energy and temperature, respectively.

For gases, the equation of state is described by the well-known equation

$$PV = nRT \quad (6.2)$$

where R is a constant (for a small temperature range), and is specific to a given gaseous material.

For solids and fluids, however, there are no analytically derived equations of state; so they are generated as empirical formulations based on experimental results. There is no small amount of art in this process, resulting in competing equation of state formulations, which

prompted Zukas [63] to note that: “Grown men sometimes descend into childish arguments over the merits of these EOS.”

Using the appropriate equation of state is important. One of the popular equations of state for solids is the Mie-Grüneisen equation of state. Zukas [63] emphasizes that this equation of state is only for solid materials that remain in the solid state throughout the impact event; that is, no phase change is allowed. Nevertheless, an extensive literature review found that at least two researchers [2, 6] used the Mie-Grüneisen equation of state to model the bird’s hydrodynamic behavior. Their results were less accurate than desired.

Fortunately, extensive research has been carried out to describe the hydrodynamic behavior of a bird [5, 8, 10, 64]. This body of research includes a considerable amount of experimental data with real birds of various sizes (weights), which to this day is referenced by many researchers in the field of bird strike analysis, even 30 years after it was first published. In addition, this research focused on developing a substitute material to represent a bird, because the non-homogenous nature and inherent variability of real birds produces results that are always difficult to duplicate.

Wilbeck [8] developed a one-dimensional hydrodynamic theory to describe bird impact. He proposed that bird material can be treated as water, since a soft body material behaves like a fluid upon impact. To account for the entrapped air in an actual bird, Wilbeck proposed that a real bird could be represented by porous water, that is, a homogeneous mixture of water and air.

In general, at loads below the Hugoniot elastic limit (HEL), a single elastic wave propagates through the projectile material. The speed of the elastic wave is given by [63]

$$c_E = \sqrt{\frac{E(1-\nu)}{\rho_0(1-2\nu)(1-\nu)}} \quad (6.3)$$

where E is the modulus of elasticity, ν is Poisson's ratio and ρ_0 is the initial density of the material. In the elastic region, the sonic velocity is constant and the pressure-density relationship is linear.

Beyond the Hugoniot elastic limit, multiple plastic waves for each value of strain are formed which coalesce into a single steep shock wave front. Since a shock wave is a physical discontinuity, the stress (pressure), density, velocity and internal energy are discontinuous across the shock wave. Furthermore, the pressure-density relationship is no longer linear in the shocked region. The shock wave, however, cannot sustain forever due to the free surfaces on the projectile's lateral surface. After several reflections, relief waves, or rarefaction waves, are formed. Consequently, a very complicated stress state exists during the relief phase. This is followed by the establishment of steady state conditions.

In his one-dimensional hydrodynamic theory for bird impact analysis, Wilbeck [8] proposed independent equations of state for the shock phase and for the steady state phase. The shock equation of state is derived based on one-dimensional shock relations, and the steady state equation of state is derived using the one-dimensional compressible Bernoulli equation for the isentropic compression. However, few bird strike researchers seem to be aware of Wilbeck's important work on the equations of state, as no references to Wilbeck's equations of state were found during the literature review done by the author. Therefore, the derivations for Wilbeck's shock and steady state equations of state are developed and explained below with added clarity.

6.1 Shock Equation of State

The one-dimensional equations of conservation of mass and momentum across a shock can be written as

$$\rho_1 u_s = \rho_2 (u_s - u_p) \quad (6.4)$$

and

$$P_1 + \rho_1 u_s^2 = P_2 + \rho_2 (u_s - u_p)^2. \quad (6.5)$$

In the above equations, subscripts 1 and 2 refer to the states before and after the shock compression, and ρ refers to density and P refers to pressure. The parameter u_s is the shock velocity, and u_p is the velocity of the projectile. When the projectile velocity is very low, the shock velocity u_s can be approximated by the constant isentropic wave speed, which is also equal to the velocity of sound in the non-shocked material. However, at high impact velocities, the velocity of the shock is a function of the impact velocity. Most researchers assume that the velocity of shock is linearly proportional to the projectile velocity. Thus, for a linear Hugoniot equation, the shock velocity u_s is given by

$$u_s = c_0 + k u_p \quad (6.6)$$

where c_0 is the isentropic wave speed and k is a constant.

If the bird is assumed to be made of water, then equation (6.6) takes the following form:

$$u_s = c_{0,water} + k_{water} u_p \quad (6.7)$$

where $c_{0,water}$ is the velocity of sound in water, 1482.9 m/s and $k_{water} = 2.0$.

Now, equations (6.4) and (6.5) can be combined to obtain the shock pressure or the Hugoniot pressure P_H as below:

$$P_H = P_2 - P_1 = \rho_1 u_s u_p. \quad (6.8)$$

The variation of shock pressure for water with the impact velocity is shown in Figure 6.1. It can be seen that the pressure and density, along with the velocity after the shock, can be solved without much difficulty using equations (6.4) through (6.8).

However, all real birds contain a certain amount of cavities and entrapped air. Wilbeck [8] included porosity to account for the entrapped air in the birds. Thus a real bird can be represented by porous water; that is, a homogeneous mixture of water and air. When porosity is included, the linear Hugoniot given by equation (6.6) no longer holds, since the relationship between the shock velocity in the porous bird material and the impact velocity becomes non-linear. An equation of state (EOS) that defines the relationship between pressure and density becomes necessary in order to solve for all the unknowns after the shock. For non-porous water, the equation of state is based on empirical relations using experimental data. This can be written as

$$\frac{\rho_2}{\rho_1} = \left(\frac{P_2}{A} + 1 \right)^{1/B} \quad (6.9)$$

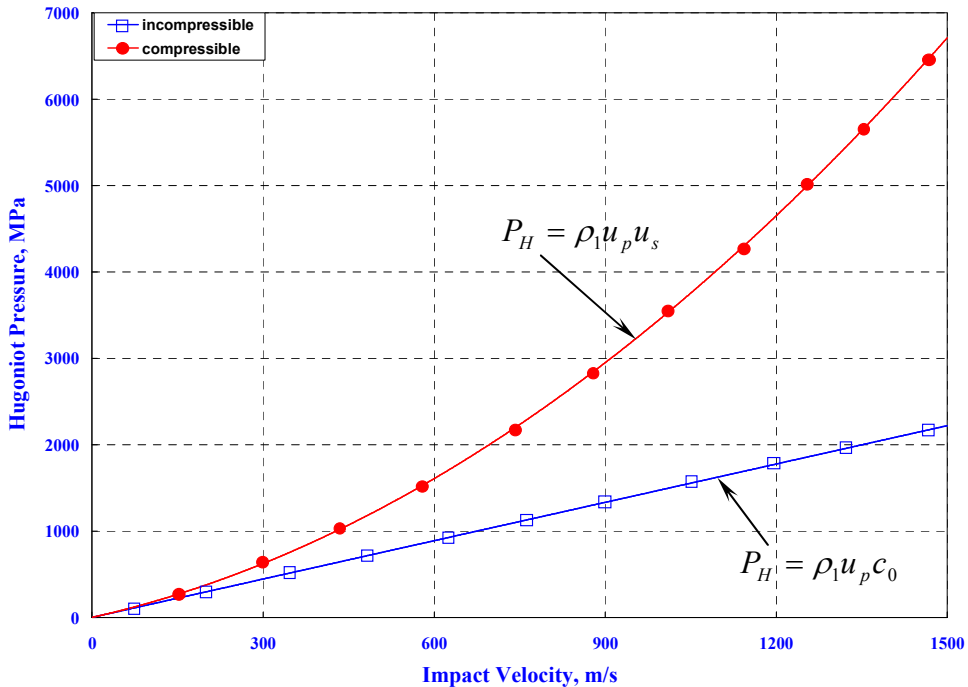


Figure 6.1. Variation of Hugoniot pressure with impact velocity for water.

where

$$A = \frac{\rho_1 c_{0,water}^2}{(4k_{water} - 1)} \quad \text{and} \quad B = (4k_{water} - 1). \quad (6.10)$$

For air, the typical pressure-density relation for a shock compression used by many researchers is given by

$$\frac{\rho_2}{\rho_1} = \frac{1 + \left(\frac{\gamma + 1}{\gamma - 1}\right) \left(\frac{P_2}{P_1}\right)}{\left(\frac{\gamma + 1}{\gamma - 1}\right) + \left(\frac{P_2}{P_1}\right)} \quad (6.11)$$

where γ is the ratio of specific heats, and is equal to 1.4 for air.

However, Deal [65] observed that equation (6.11) is only good for density ratios $\frac{\rho_2}{\rho_1}$ less than 6; and for density ratios beyond this, equation (6.11) produces results that are drastically different from the experimental results. Deal proposed a new equation of state for air undergoing shock compression:

$$P_2 = \frac{\rho_1 c_{0,air}^2 q}{(1 - k_{air} q)^2} \quad (6.12)$$

where q is defined as

$$q \equiv 1 - \frac{\rho_1}{\rho_2}. \quad (6.13)$$

In equation (6.12), $c_{0,air}$ is the velocity of sound in air, 340.9 m/s and $k_{air} = 1.03$.

Now, equation (6.12) can be rewritten as

$$\bar{P} \equiv \frac{P_2}{P_1} = \frac{\rho_1 c_{0,air}^2}{P_1} \frac{q}{(1 - k_{air} q)^2}. \quad (6.14)$$

Solving for q from the quadratic equation of (6.14), we get

$$q = q_1 \pm q_2 \quad (6.15)$$

where

$$q_1 = \left(\frac{2\bar{P}k_{air} + \frac{\rho_1 c_{0,air}^2}{P_1}}{2\bar{P}k_{air}^2} \right) \quad (6.16)$$

and

$$q_2 = \frac{\left\{ \left[2\bar{P}k_{air} + \frac{\rho_1 c_{0,air}^2}{P_1} \right]^2 - 4\bar{P}^2 k_{air}^2 \right\}^{1/2}}{2\bar{P}k_{air}^2} \quad (6.17)$$

But, from the definition of q from equation (6.13), we can see that for $\frac{\rho_1}{\rho_2}$ to be positive (note

that $\frac{\rho_1}{\rho_2}$ is always less than 1 for shock compression), q must be less than unity. This requires

equation (6.15) to take the following form:

$$q = q_1 - q_2. \quad (6.18)$$

Wilbeck [8] utilized mixture theory to combine the equations (6.9) and (6.12) to derive an equation of state for the shock compression phase of the porous material. This equation of state is given by

$$\left(\frac{\rho_1}{\rho_2} \right)_{,porous} = (1-z) \left(\frac{\rho_1}{\rho_2} \right)_{,water} + z \left(\frac{\rho_1}{\rho_2} \right)_{,air} \quad (6.19)$$

where z refers to the amount of porosity of the material.

Now, using equations (6.9) and (6.13), the above equation becomes

$$\frac{\rho_{1,porous}}{\rho_{2,porous}} = (1-z) \left[\frac{P_2}{A} + 1 \right]^{-1/B} + z(1-q). \quad (6.20)$$

The shock velocity u_s in the porous material, along with P_2 and ρ_2 after the shock, can be obtained by the simultaneous solution of equations (6.4), (6.5) and (6.20).

The effect of porosity of the bird material on shock velocity and on Hugoniot pressure is presented in Figures 6.2 and 6.3.

6.2 Steady State Equation of State

For one-dimensional compressible flow, the steady state stagnation pressure is related to the velocity of impact by the Bernoulli's equation as follows:

$$\int_{P_1}^{P_2} \frac{dP}{\rho} = \frac{u_p^2}{2}. \quad (6.21)$$

In order to solve this equation, we require a pressure-density relation in the form of an equation of state.

For non-porous water, the equations of state for both shock compression and isentropic compression are identical, as given by equation (6.9) which is repeated below:

$$\frac{\rho_2}{\rho_1} = \left(\frac{P_2}{A} + 1 \right)^{1/B}. \quad (6.9)$$

On the other hand, the equation of state for isentropic compression of air is significantly different from its shock equation of state, and is given by

$$\frac{\rho_2}{\rho_1} = \left(\frac{P_2}{P_1} \right)^{1/\gamma}. \quad (6.22)$$

The equation of state for isentropic compression of the porous bird material is obtained from the mixture theory as before, and is given by

$$\left(\frac{\rho_1}{\rho_2} \right)_{,porous} = (1-z) \left[\frac{P_2}{A} + 1 \right]^{-1/B} + z \left[\frac{P_2}{P_1} \right]^{-1/\gamma}. \quad (6.23)$$

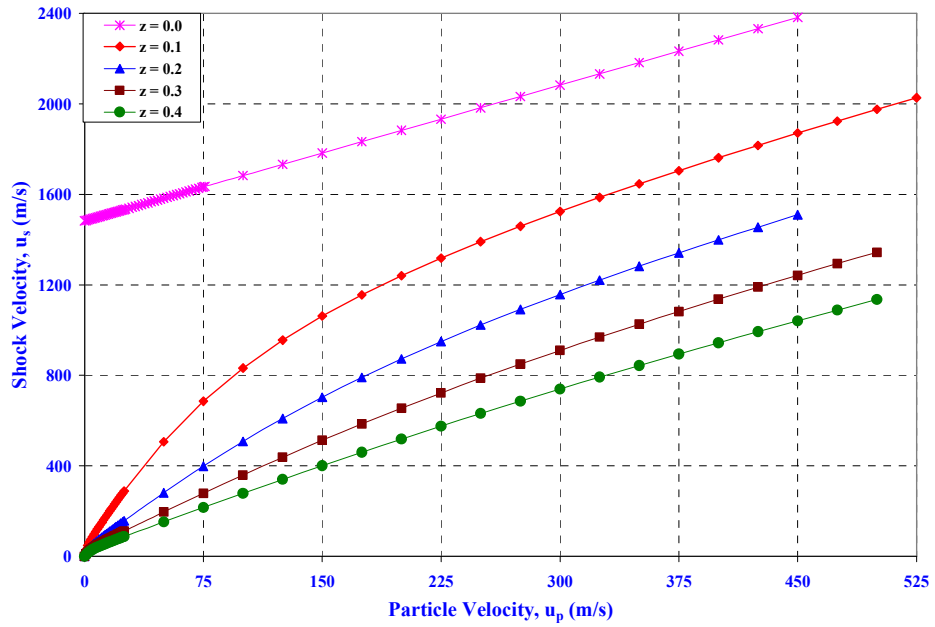


Figure 6.2. Effect of porosity on shock velocity.

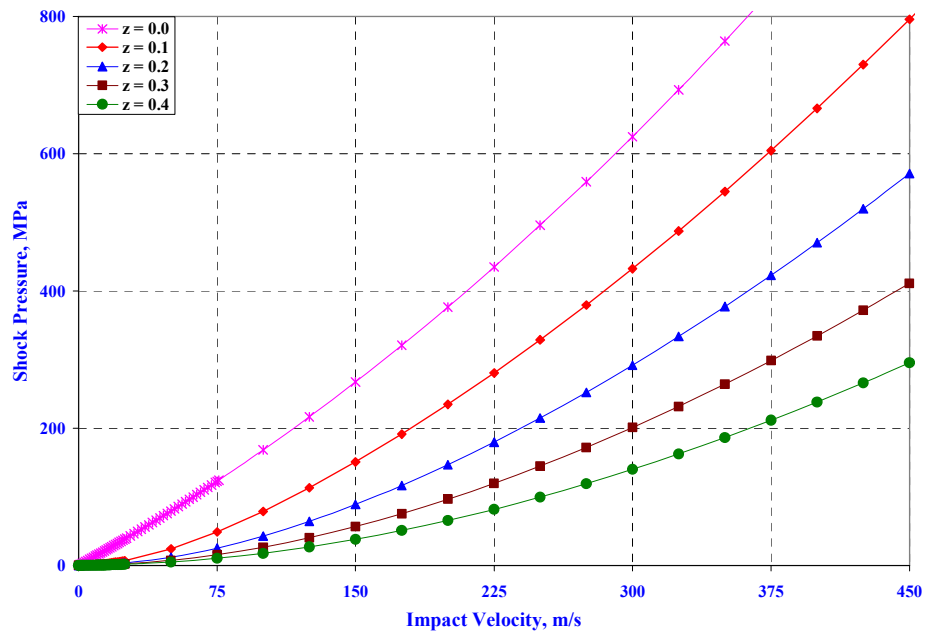


Figure 6.3. Effect of porosity on shock pressure.

The relationship between the steady state stagnation pressure and the projectile velocity is obtained from the simultaneous solution of equations (6.21) and (6.23).

The pressures computed from the shock equation of state and the steady state equation of state are presented in Figures 6.4 and 6.5.

6.3 Impact Event Equation of State

The equations of state presented thus far were derived from one-dimensional relations; and, therefore, are independent for the shock compression and isentropic compression.

However, a three-dimensional numerical simulation requires a single equation of state that accurately represents the entire impact event, including both the Hugoniot shock pressure and the steady state stagnation pressure. This single equation of state must include the discontinuity associated with the shock. In the current work, an equation of state is proposed that serves the entire impact event (referred to here as “the impact event equation of state”) by including both the shock compression and the isentropic compression phases.

The impact event equation of state (EOS) was derived by combining the shock equation of state and the steady state equation of state proposed by Wilbeck [8]. Based on experimental results [5, 8, 10, 64], it was observed that the steady state stagnation pressures are below 40 MN/m² for birds of all sizes (weights) tested. Therefore, this work used the isentropic equation of state for pressures below 40 MN/m² and the shock equation of state for pressures above 40 MN/m². The single impact event equation of state was then defined by fitting a 3rd degree polynomial for the combination of pressures generated by the shock equation of state and the isentropic equation of state.

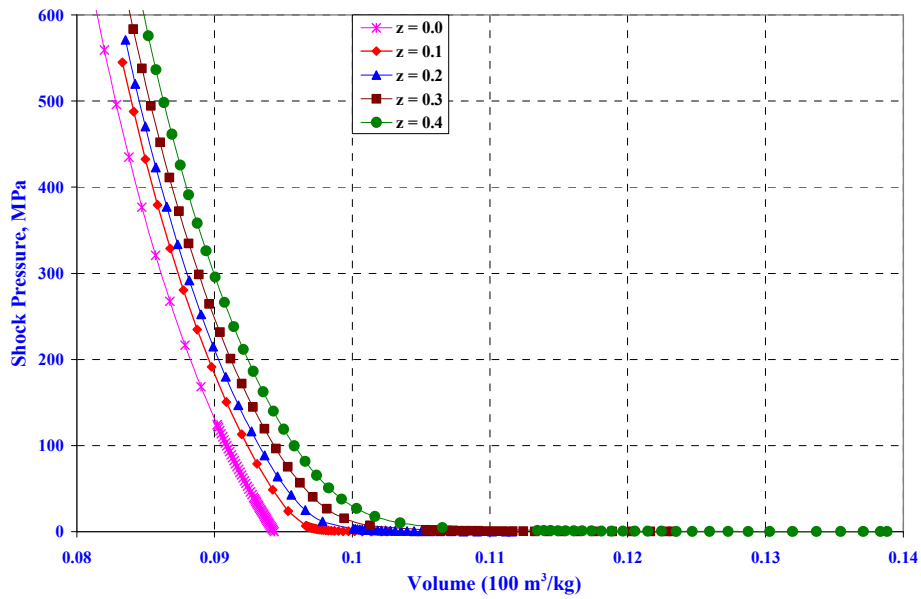


Figure 6.4. Pressure-volume relationship computed from shock equation of state.

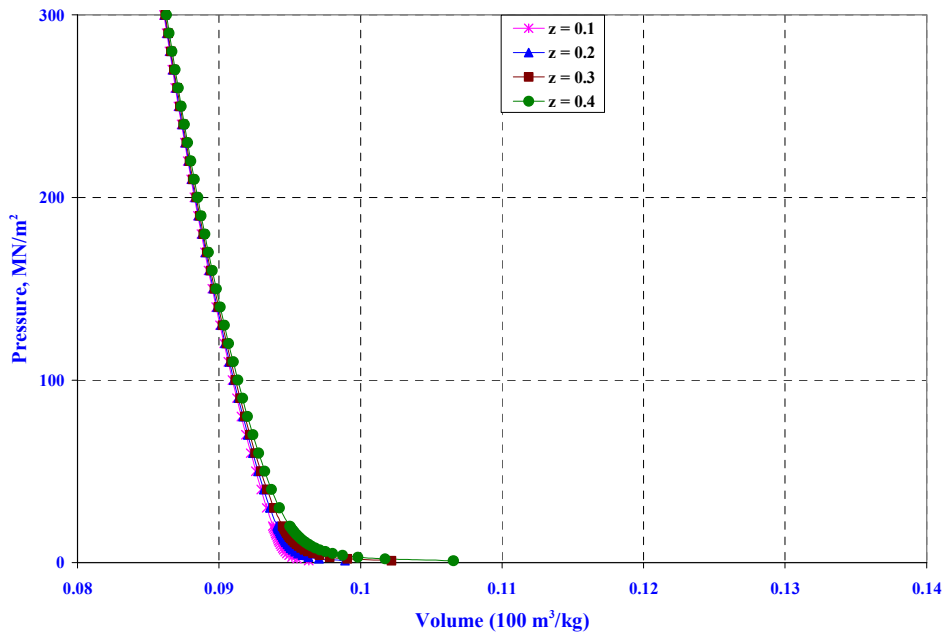


Figure 6.5. Pressure-volume relationship computed from steady state equation of state.

CHAPTER 7

HOMOGENEOUS BIRD MODELS

An important part of bird strike analysis was choosing the appropriate numerical model of the bird. Included in this modeling exercise was the selection of the shape and material of the bird. Typical bird shapes used in numerical analyses vary among the following primitive geometries: right circular cylinder, hemi-spherical cylinder, sphere and ellipsoid. Extensive literature review did not turn up any comparative study that systematically investigated the effect of the projectile shape on the impact loads generated. As a first step, this work filled this gap by providing a comparative analysis of various primitive projectile shapes on the impact loads.

It may be recalled that the bird strike event was characterized by three important phases: shock compression, shock decay, and the establishment of a steady state condition. In addition to reproducing the entire pressure-time history, a rational numerical simulation of bird strike analysis should accurately replicate the Hugoniot shock pressure as well as the steady state stagnation pressure. Since the bird is generally represented as a soft body material to model its hydrodynamic behavior, an accurate representation of the bird's equation of state is critical to predicting correct impact loads. In this research, the effect of the equation of state model of the bird material on the impact loads of a bird strike event was investigated. Chapter 6 presented the derivations of two equations of state, based on one-dimensional shock theory and one-dimensional compressible fluid theory for isentropic compression, as proposed by Wilbeck [8]. These two equations of state, representing the shock compression phase and the steady state compression phase, were investigated. Note that the shock equation of state was derived for the shock compression phase, and hence was expected to perform well in predicting the shock pressures, or the Hugoniot pressures. Likewise, the steady state equation of state was expected

to produce a good correlation with the steady state pressures measured in the experimental tests, since it was originally built for the isentropic compression phase of the impact process.

However, as explained in Chapter 6, any three-dimensional numerical simulation of a bird impact event inevitably entails an equation of state that serves the entire impact event (shock and steady state together). The impact event equation of state proposed in Chapter 6 is a viable option to model the full impact event. Therefore, in this work the results obtained using the impact event equation of state were compared to those obtained from the individual shock and steady state equations of state; and the validity of the impact event equation of state for use in bird strike analysis was investigated.

For simplicity, the target structure was initially assumed to be rigid for comparative analysis of the equation of state models. This was done so to eliminate the target flexibility as an influencing factor in the otherwise highly complex and nonlinear bird impact analysis. In addition, the impact velocity was assumed to be normal to the target. After the candidate formulations for the equation of state models were reviewed using a rigid target, the analysis was extended to briefly explore the effects of target structure flexibility to show the effect of the target structure's deflection on the corresponding impact pressures in the numerical simulation.

For bird material, many researchers have used a homogeneous mixture of 90% water and 10% air. However, the predicted impact pressures from this mixture of water and air [66] failed to accurately match the experimental results [5, 8, 10, 64]. For the same combination of 90% water and 10% air, Wilbeck's hydrodynamic theory [8] failed to predict the correct Hugoniot shock pressures, even though the prediction of steady state stagnation pressures was more precise. From the experimental results presented in [5, 8, 10, 64], it appears that increasing the porosity might produce a better match of predicted Hugoniot shock pressures with those

observed in experiments. Therefore, in this research the effect of porosity in combination with the various equations of state was investigated.

In addition, the effects of oblique impact were considered on a rigid target. Specifically, projectile directions of 45 degrees and 25 degrees were investigated.

Next, the target flexibility was introduced into the analysis, and the inherent coupling between the impact loads and the target deflection was explored.

To summarize, the work presented in this chapter

1. Determined the effect of several projectile shapes on a rigid target,
2. Investigated the validity of various equation of state models and material porosity levels for matching experimentally measured pressures for impacts on a rigid target,
3. Determined the effect of the projectile impact obliquity on the impact loads,
4. Determined the effect of target flexibility on the impact loads.

7.1 Effect of Projectile Shape on a Rigid Target

For the purpose of this investigation, the four typical projectile shapes that are generally used in bird strike analysis – right circular cylinder, hemi-spherical cylinder, sphere and ellipsoid – were considered. In each case, the total weight of the bird was assumed to be 0.55 kg. The total volume of each projectile shape was identical. The numerical models of the projectiles were built such that the nodal density of each projectile was approximately the same.

The cylindrical projectile model had a total of 22,983 Smoothed Particle Hydrodynamics (SPH) particles, and had a length-to-diameter ratio of 2. The sphere model consisted of 25,611 SPH particles. The ellipsoid (the rugby ball) projectile model was comprised of 19,825 SPH particles. This ellipsoid was actually a prolate spheroid with both of its equatorial radii being

equal and each was equal to one-half of its polar radius. The hemi-spherical cylinder (the cylinder with the hemi-spherical ends) model had a total of 22,564 SPH particles and also had a length-to-diameter ratio of 2.

The total weight of the bird was distributed equally among the SPH particles of each projectile. In each projectile shape, the SPH particles were distributed such that they were equally spaced in all directions, including in the plane of any given cross-section as well as in the direction normal to the plane of the cross-section. The numerical models of the projectile shapes are presented in Figure 7.1.

To simulate a rigid target, the target structure was modeled as a steel plate, with a thickness of 5 mm. In addition, all the degrees of freedom of the target structure were constrained. The target structure was modeled using Belytschko-Tsay shell elements [22].

Projectile deformations at different stages of the impact process are presented for various projectile shapes investigated in Figures 7.2 through 7.5. The impact velocity for all the projectiles was 200 m/s and was normal to the rigid target. In addition, all the projectiles were assumed to have a porosity z of 0.4. The bird material for all projectiles was modeled using the full impact event equation of state.

The shock pressures and the stagnation pressures computed from the various projectile shapes are presented in Figures 7.6 and 7.7, respectively, for a range of projectile velocities. These figures also display the experimental results from [8, 64] for medium size birds. The exact weights of the test specimens were not given; however, it is stated that the specimens weighed between 0.5 kg to 1 kg. In addition, these figures display the computed shock and steady state pressures from Wilbeck's [8] theory. Also, for comparative purposes the results from the

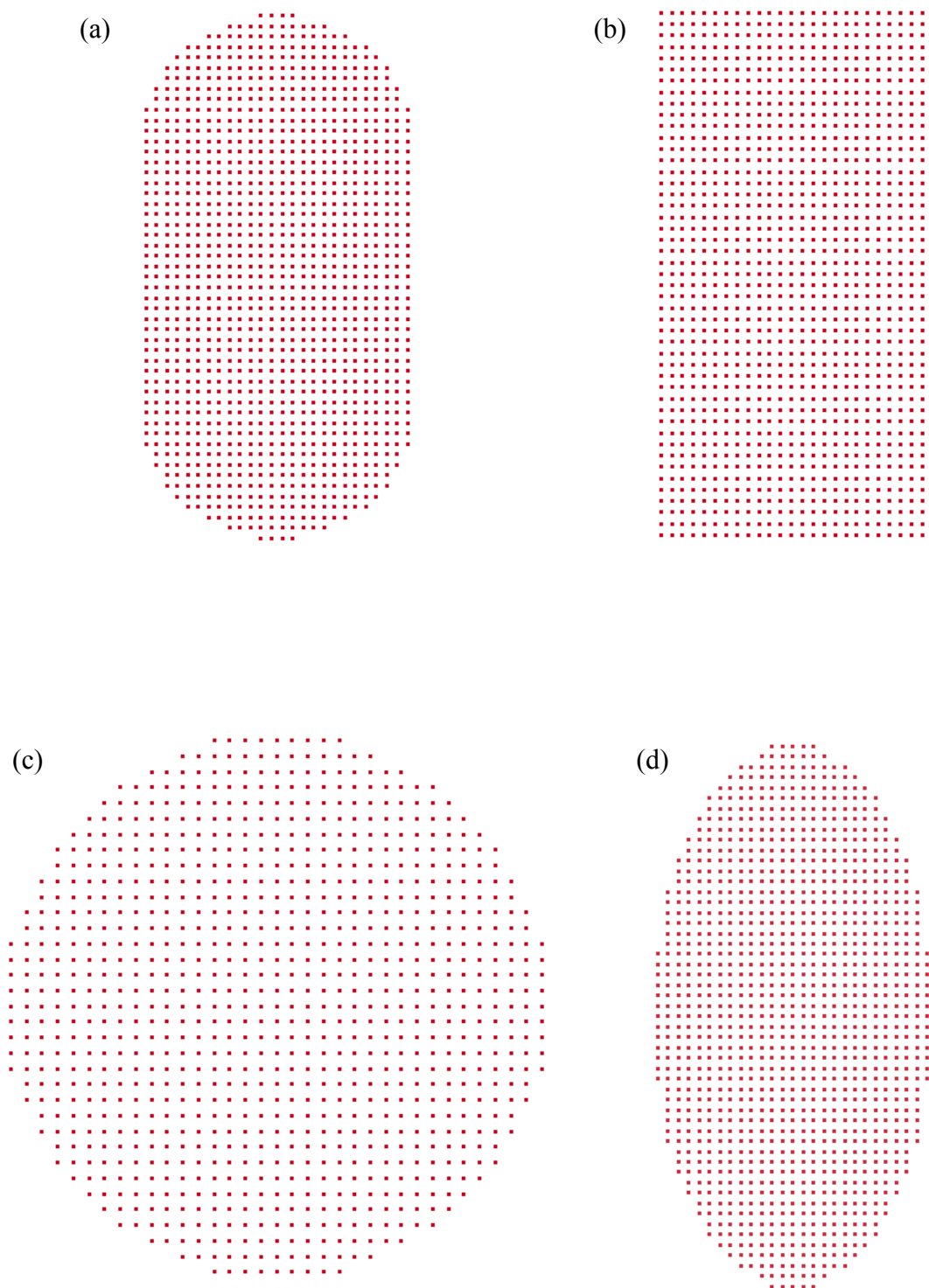


Figure 7.1. Longitudinal-sectional particle geometry for numerical models of various projectile shapes a) Hemi-spherical cylinder, b) Right circular cylinder, c) Sphere and d) Ellipsoid.

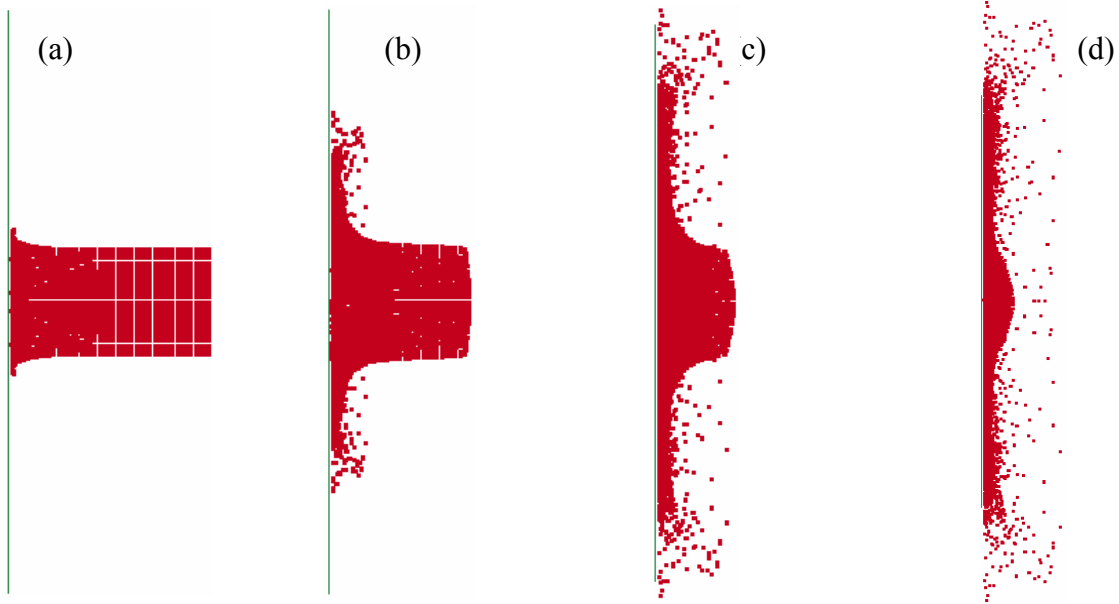


Figure 7.2. Instantaneous particle displacements for a cylindrical projectile at different times during impact with a rigid flat plate a) 0.0009 s, b) 0.0012 s, c) 0.0015 s and d) 0.0018 s.

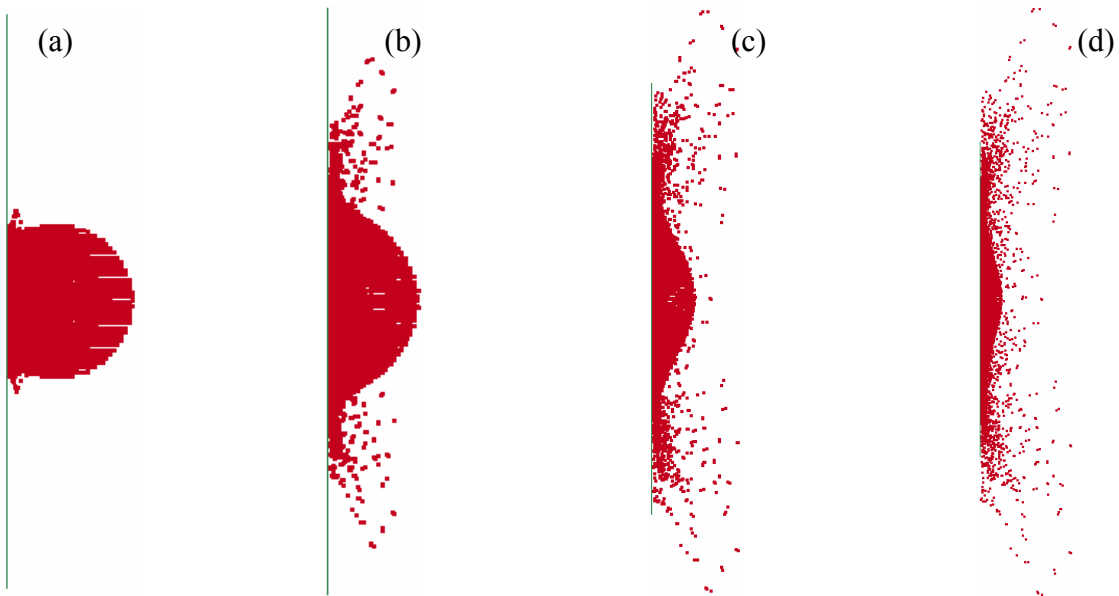


Figure 7.3. Instantaneous particle displacements for a spherical projectile at different times during impact with a rigid flat plate a) 0.0011 s, b) 0.0013 s, c) 0.0015 s and d) 0.0017 s.

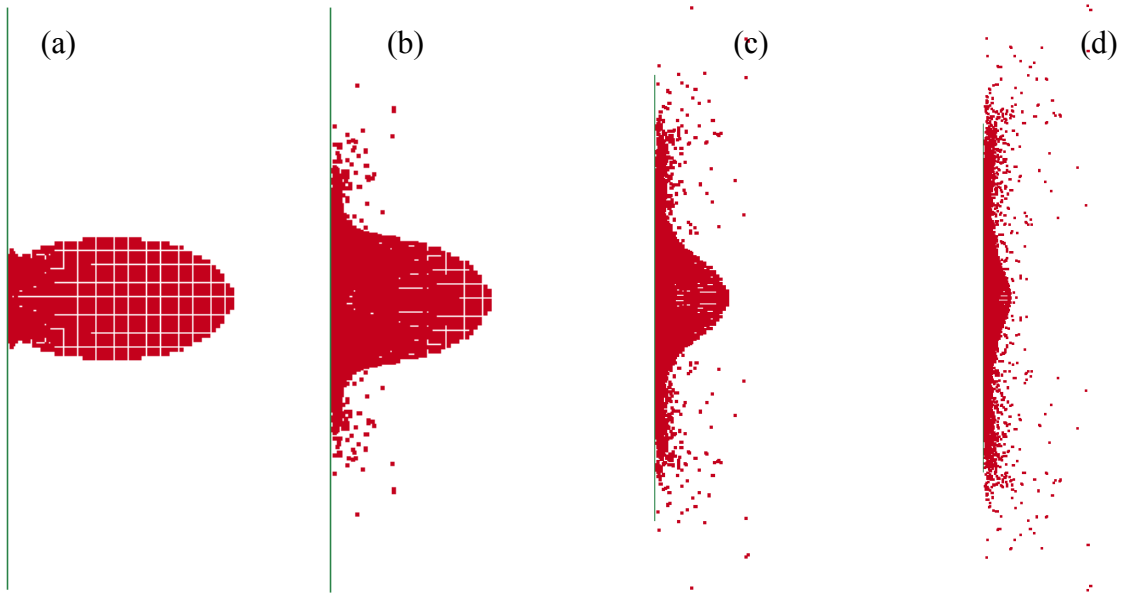


Figure 7.4. Instantaneous particle displacements for an ellipsoid projectile at different times during impact with a rigid flat plate a) 0.0006 s, b) 0.0009 s, c) 0.0012 s and d) 0.0015 s.

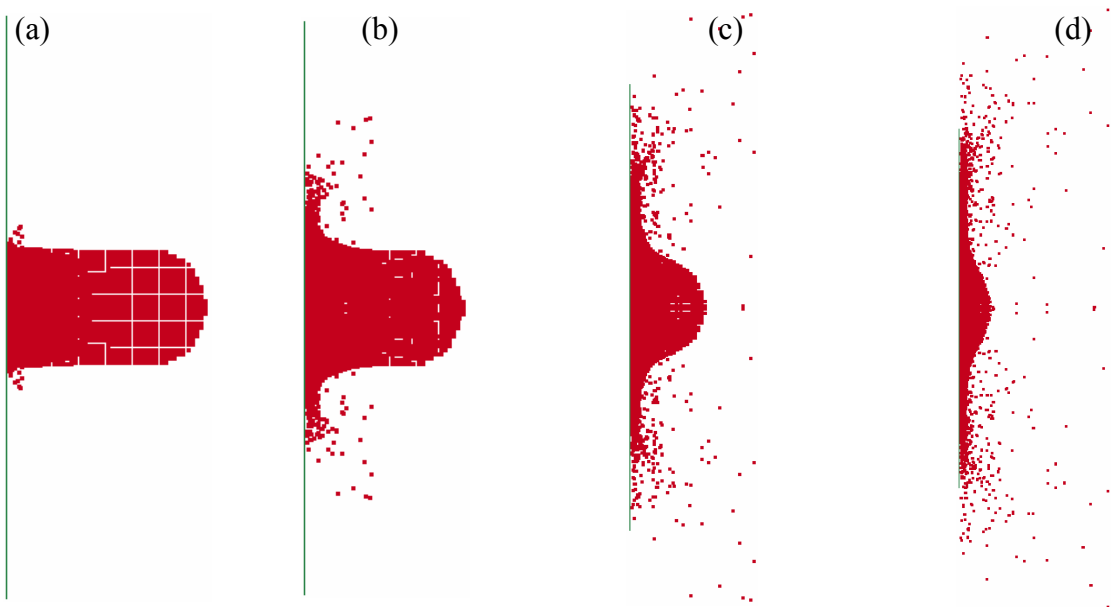


Figure 7.5. Instantaneous particle displacements of a hemi-spherical projectile at different times during impact with a rigid flat plate a) 0.00068 s, b) 0.00096 s, c) 0.00116 s and d) 0.00144 s.

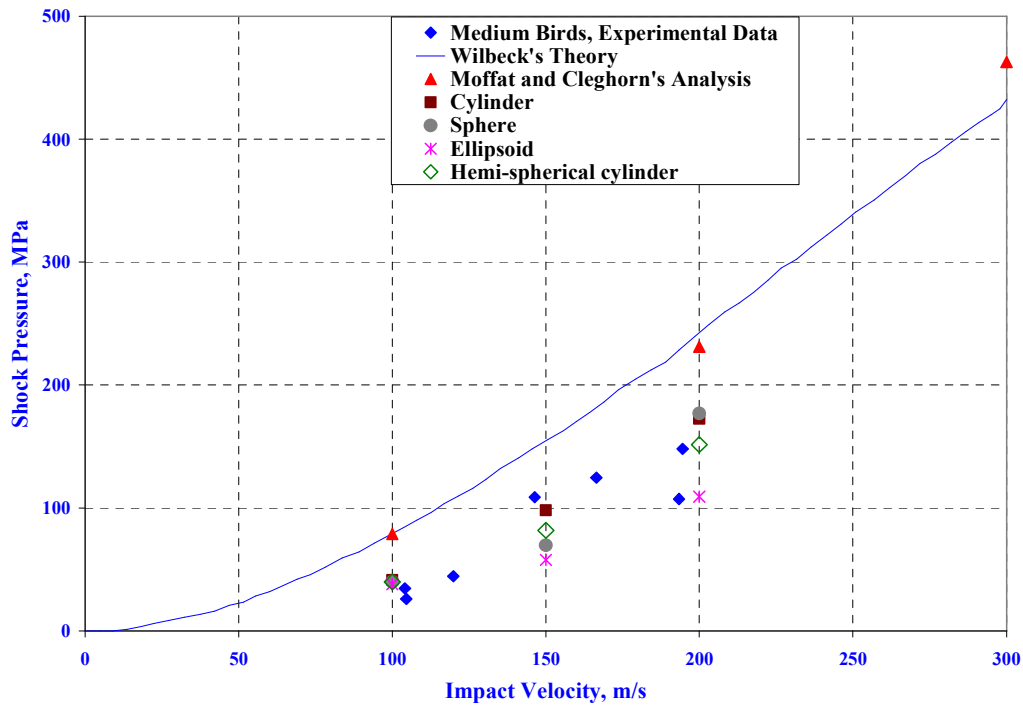


Figure 7.6. Effect of projectile shape on shock pressure for $z = 0.4$.

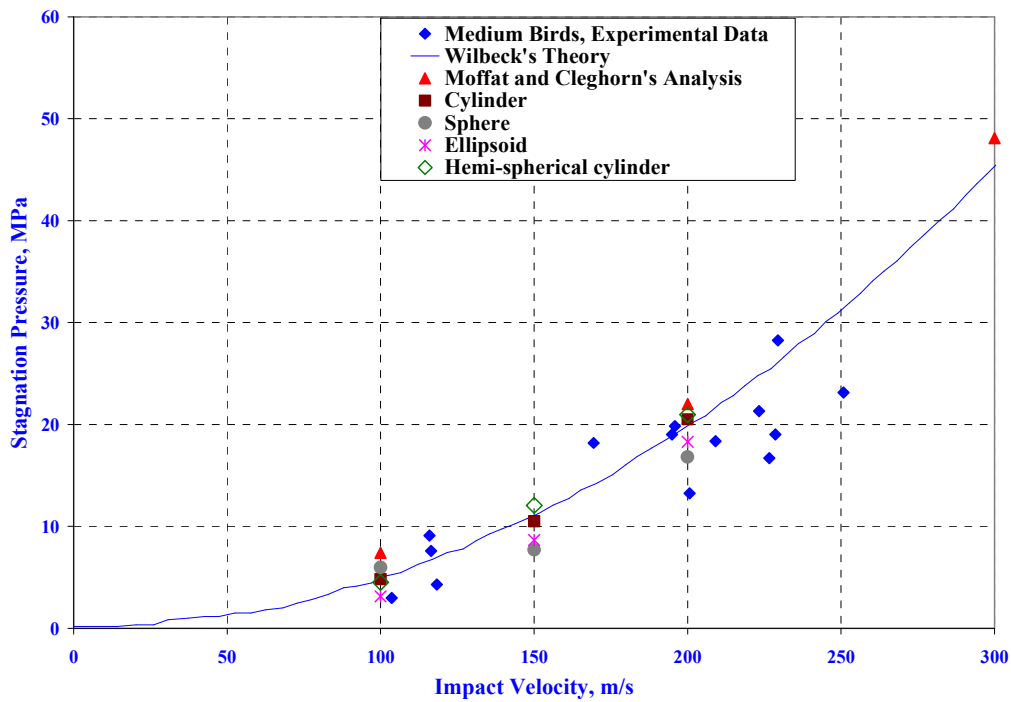


Figure 7.7. Effect of projectile shape on steady state pressure for $z = 0.4$.

numerical analysis of Moffat and Cleghorn [66] have been included in the figures.

From Figure 7.6, it can be seen that the predicted shock pressures associated with all of the projectile shapes compared well with the experimental results. In fact, all of the projectile shapes analyzed produced a better correlation with the experimental results when compared to either Moffat and Cleghorn's [66] analysis or Wilbeck's theory [8].

From Figure 7.7, it can be seen that the computed steady state pressure from the various projectile shapes match well with the experimental results, the results from Moffat and Cleghorn's [66] analysis, and those computed from Wilbeck's theory [8]. Most previous analyses were capable of predicting the steady state stagnation pressures with good accuracy. In fact, Wilbeck's one-dimensional theory provides a quick way of checking the steady state pressure before performing a full three-dimensional analysis.

From Figures 7.6 and 7.7, it can be observed that a projectile with the shape of a hemi-spherical cylinder predicts both shock and steady state pressures with good accuracy, and with reliable consistency for all bird impact speeds. Therefore, it was considered as a viable option for modeling the bird in subsequent bird impact analyses. Based on this observation, this research used the hemi-spherical cylindrical projectile for all the numerical analyses of the homogeneous bird model.

7.2 Effect of Equation of State Models and Porosity

Detailed derivations of the shock equation of state and the steady state equation of state, based on the one-dimensional hydrodynamic theory of Wilbeck [8], were presented in Chapter 6. The impact event equation of state that combined these two models to represent the entire impact event for use in three-dimensional numerical analysis was also proposed in Chapter 6. In this section, the effectiveness of these three equations of state was investigated. In addition, as

mentioned before, the effect of porosity in combination with these equations of state was studied.

For all the analyses in this section, the bird was simulated as a projectile with the shape of a hemi-spherical cylinder. The total weight of the bird was 0.55 kg, and was equally distributed among all the SPH particles. The direction of the projectile was normal to the target. The target flexibility was not considered. The rigid target was constrained in all degrees of freedom.

The bird material was assumed to be a homogenous mixture of water and air, but with varying amounts of porosity. Material porosity was introduced into the numerical model through the initial density value in conjunction with the pertinent equation of state model.

As before, the experimental results from [8, 64], along with the results obtained from Wilbeck's one-dimensional hydrodynamic theory [8], and the results from the numerical analysis of Moffat and Cleghorn [66] were used as reference points for comparisons.

The peak shock pressures predicted by the three equation of state models are presented in Figure 7.8 for varying amounts of porosity at projectile velocities of 100 m/s, 150 m/s and 200 m/s. It can be observed that all three equations of state investigated produced a generally better match with the experimental results, especially at higher speeds, when compared to Wilbeck's theory [8] or Moffat and Cleghorn's analysis [66]. In addition, increasing the amount of porosity with any of the three equation of state models tended to improve the correlation with the experimental results. In particular, 30% to 40% porosity gave better overall agreement with experimental results than lesser amounts of porosity.

Of the three equations of state models, the simulation results obtained with the use of the shock equation of state appear to be the best match with the shock pressures measured in the tests. This was expected because this equation of state was developed specifically for the shock compression phase. Note that of all the equation of state models investigated, the steady state

equation of state was the worst choice for predicting the shock pressures. The impact event equation of state produced excellent overall results, agreeing closely with the experimental results with one apparent exception that is addressed below.

Certain inconsistencies can be noticed in Figure 7.8, such as a reduction in the shock pressure in certain cases as the impact velocity was increased, which is counter-intuitive. It is emphasized here that this was not an error in the numerical method, but a numerical inaccuracy introduced by the insufficient output interval resolution. When the output interval resolution was not fine enough, it was possible to miss the peaks in the pressure, even though the computed numerical solution captures all the pressure peaks. These discrepancies can be minimized, or perhaps eliminated altogether, by specifying a sufficiently small output interval. The limitation that prevented using the highest output resolution in all cases was the substantial amount of memory required to store all the solution variables at all output states. For example, setting the output interval at 1 micro-second for a total event time of 2 milli-seconds (for impact velocity of 200 m/s), produced an output database of 1 GB size. Storing and working with such large databases, especially when studying many combinations of influencing parameters, was impractical even with high computer storage capabilities.

An alternative approach would be to set the output resolution at least equal to the resolution of current state-of-the-art pressure transducers. With this in mind, when the impact event solution for $z = 0.4$ was re-computed at the impact velocity of 200 m/s, after reducing the output interval from 1×10^{-4} s to 2×10^{-5} s, a significant improvement in the solution was attained, as shown by the open circle in Figure 7.8 (c).

The comparison of the steady state stagnation pressures is given in Figure 7.9. Once again, all three equation of state models performed very well and predicted results that were in

excellent agreement with both experimental and previous analytical results. As expected, the steady state equation of state, which was the equation of state specifically designed for the steady state phase, predicted stagnation pressures that were in very close agreement with the stagnation pressures measured in the tests. The shock equation of state did not perform very well as a predictor of stagnation pressures.

Importantly, the impact event equation of state quite accurately predicted both the shock and steady state pressures. This was expected as this equation of state was designed for the entire impact event. Thus, of all the results presented, including the results from Wilbeck's hydrodynamic theory [8] and the predicted results of Moffat and Cleghorn [66], the results obtained from the impact event equation of state produced the best match with the experimental results for the *entire* impact event.

Therefore, these preliminary analyses provided an essential foundation for the validity of the impact event equation of state. Based on these results, it was decided to use the impact event equation of state for all the subsequent analyses. Furthermore, it was established that the porosity played a significant role in accurately predicting the Hugoniot shock pressures. In particular, a porosity choice of 0.3 or 0.4 was a viable alternative for the projectile model.

7.3 Effect of Oblique Impact

In this section, the analysis was extended to include the oblique impact of the bird on a rigid target. For oblique impact, the velocity vector of the projectile was directed at an angle to the target, and the projectile itself was rotated such that its longitudinal axis coincided with the direction of the velocity vector. Impact angles of 45 degrees and 25 degrees were selected to study the effect of oblique impact. These impact angles, in combination with impact velocities of 100 m/s, 150 m/s and 200 m/s, were investigated.

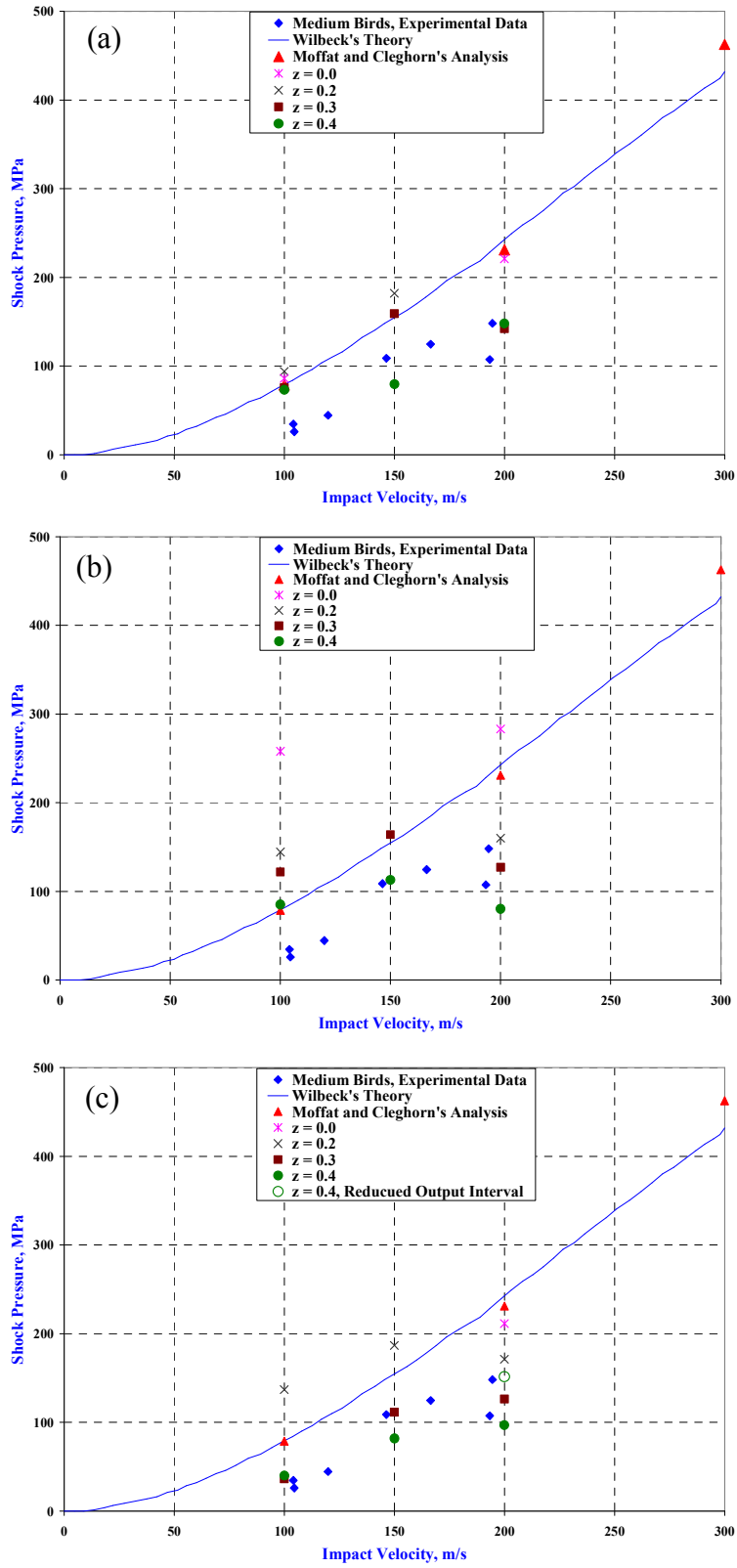


Figure 7.8. Comparison of shock pressures a) Hugoniot or Shock equation of state, b) Isentropic equation of state, c) Impact event equation of state.

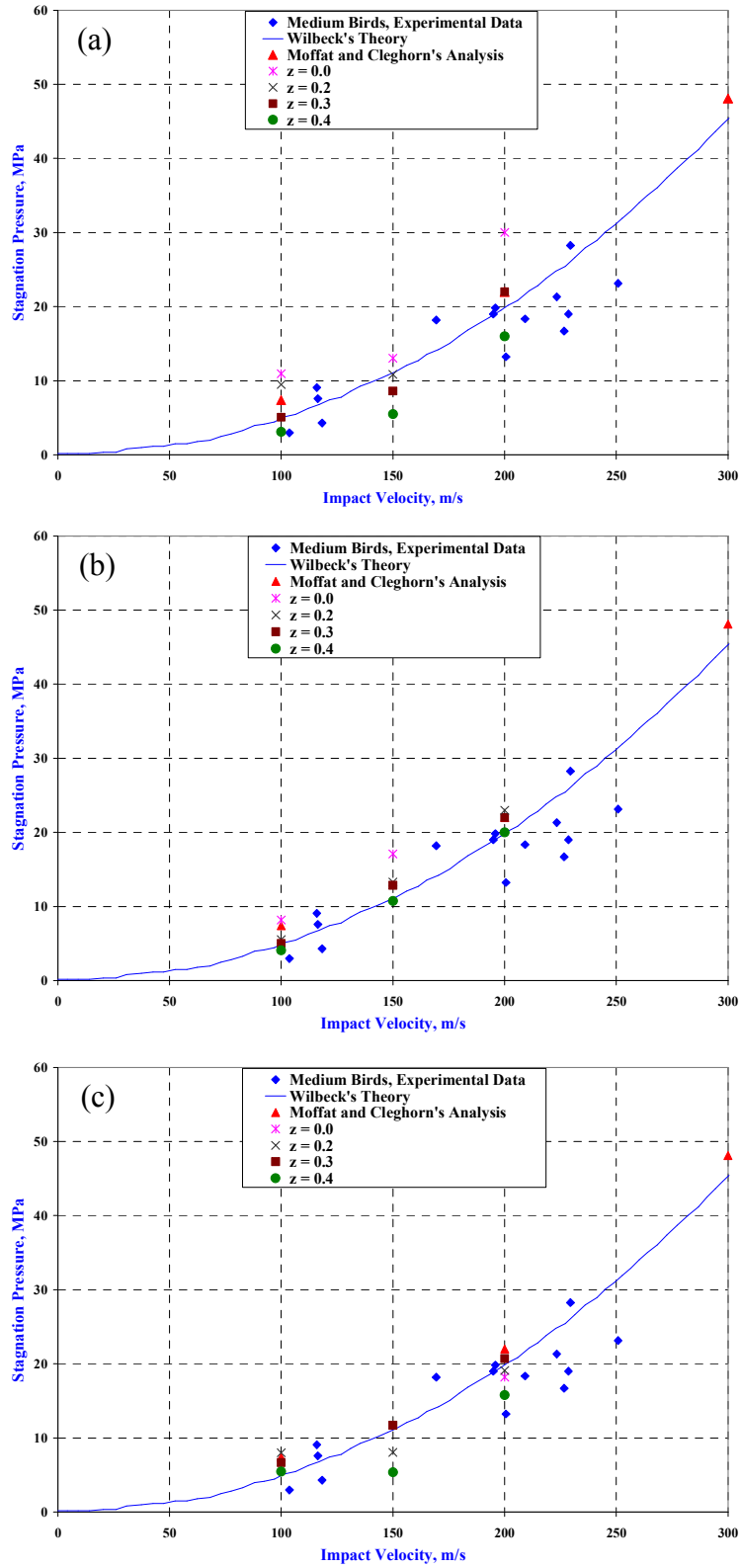


Figure 7.9. Comparison of stagnation pressures a) Hugoniot or Shock equation of state, b) Isentropic equation of state, c) Impact event equation of state.

During the shock compression phase, the normal component of the projectile velocity was expected to provide the major contribution to the momentum transfer between the projectile and the target. In fact, Wilbeck [8] noted that the Hugoniot shock pressure generated for an oblique impact was identical to that produced by a normal impact of a projectile with a velocity equal to the normal component of the oblique impact projectile. The shock pressure was expected to decrease with the impact angle, due to the reduction in the normal component of the velocity vector with decreasing impact angle.

Locating the stagnation point for oblique impact was not as straightforward as for the case of a normal impact. This was due to the fact that the stagnation point was not located at the center of the target any more, but shifted to a different location because of the impact angle. However, Wilbeck [8] noted that the stagnation pressure was independent of the angle of impact. On the other hand, the resulting pressure distribution over the surface of the target structure was found to be significantly different from the pressure distribution due to a normal impact.

As before, a hemi-spherical projectile was used for investigating the effect of oblique impact. The bird material was assumed to be 40% porous ($z = 0.4$). Projectile deformations at various times, with an impact angle of 45 degrees are presented in Figure 7.10. Figure 7.11 portrays the deformation of the projectile with an impact angle of 25 degrees at various times.

The comparison of peak shock pressures is displayed in Figure 7.12 for an impact angle of 45 degrees. This figure also contains results from experimental tests and the numerical simulation results of Moffat and Cleghorn [66]. Note that the test specimens for the experimental tests weighed in the range of 2 to 4 kg. The mass of the bird of the Moffat and Cleghorn analysis was 0.55 kg. The weight of the numerical projectile used in the current analysis was 0.55 kg.

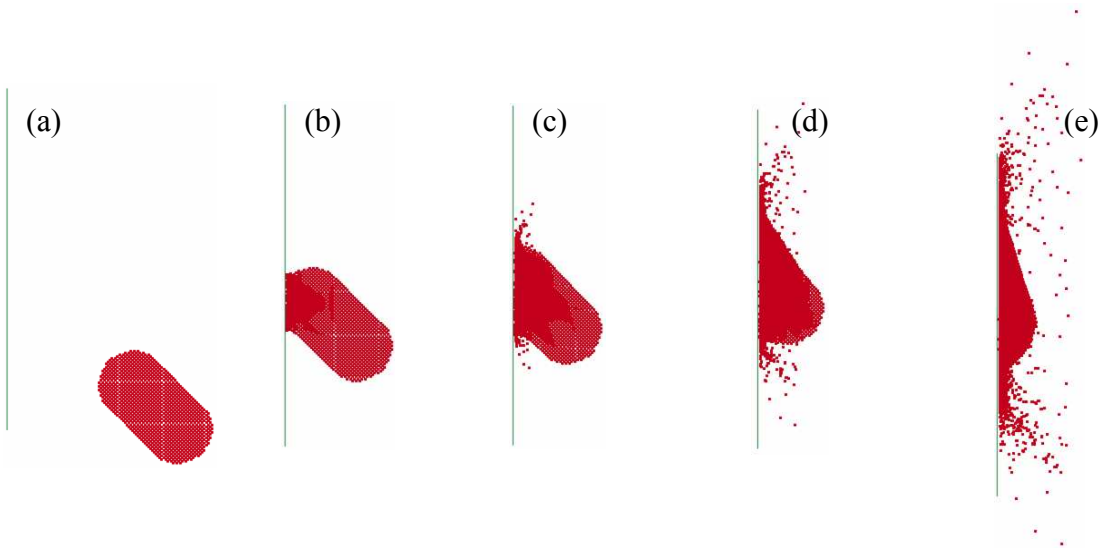


Figure 7.10. Instantaneous particle displacements for impact obliquity of 45 degrees at different times during impact with a rigid flat plate a) 0.0 s, b) 0.0008 s, c) 0.00096 s, d) 0.0012 s and e) 0.00142 s.

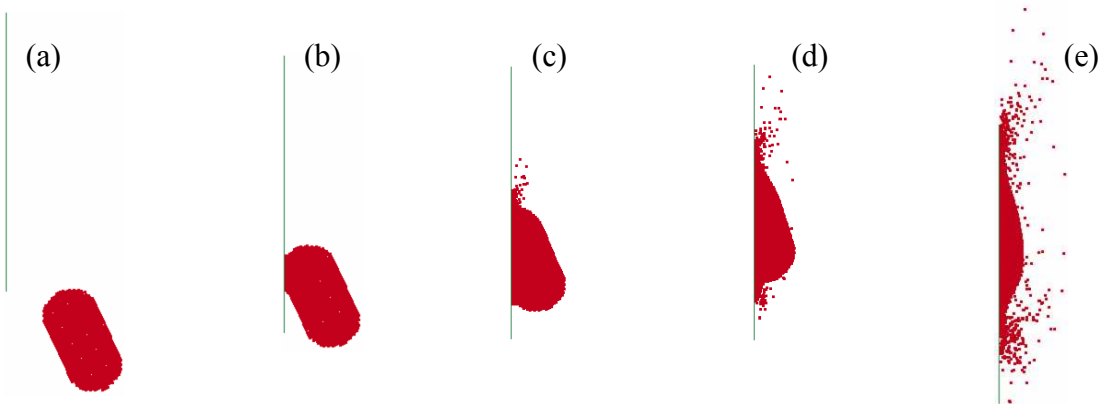


Figure 7.11. Instantaneous particle displacements for impact obliquity of 25 degrees at different times during impact with a rigid flat plate a) 0.0 s, b) 0.00068 s, c) 0.0012 s, d) 0.0013 s and e) 0.00168 s.

From Figure 7.12, it can be observed that the trend of the results from the current research agree well with the experimental results, considering the differences in assumed bird weights. In addition, it can be noticed that, even though both Willbeck's theory and Moffat and Cleghorn's analysis predicted the shock pressures accurately at low impact velocities, there appeared to be a widening gap between the experimental results and their predictions as the impact velocity increased. This observation was also true for the case of normal impact on a rigid target.

The comparison of the shock pressures for impact angle of 25 degrees is contained in Figure 7.13. This figure also contains the results from the numerical simulation results of Moffat and Cleghorn [66]. No experimental results are available for this case. As before, the results from all the analyses agree well with each other, especially at low impact velocities.

No comparison for the steady state pressures is provided for oblique impact cases, due the lack of experimental data or predicted results from any other numerical simulations. Furthermore, based on the previous steady state pressure comparisons, a good agreement is expected between the results from various sources.

7.4 Effect of Target Structure Flexibility

The current research has focused thus far on investigating the effect of bird impacts on a rigid target. As explained before, this was done to eliminate target flexibility as an influencing factor. However, all real structures are flexible to a certain extent; and the impact loads for a flexible target are coupled to the target deformation; so, target structure flexibility cannot be disregarded. Therefore, having gained useful insights into the complexities of the bird strike problem using a rigid target, the effect of target flexibility was then analyzed in order to make this research more complete.

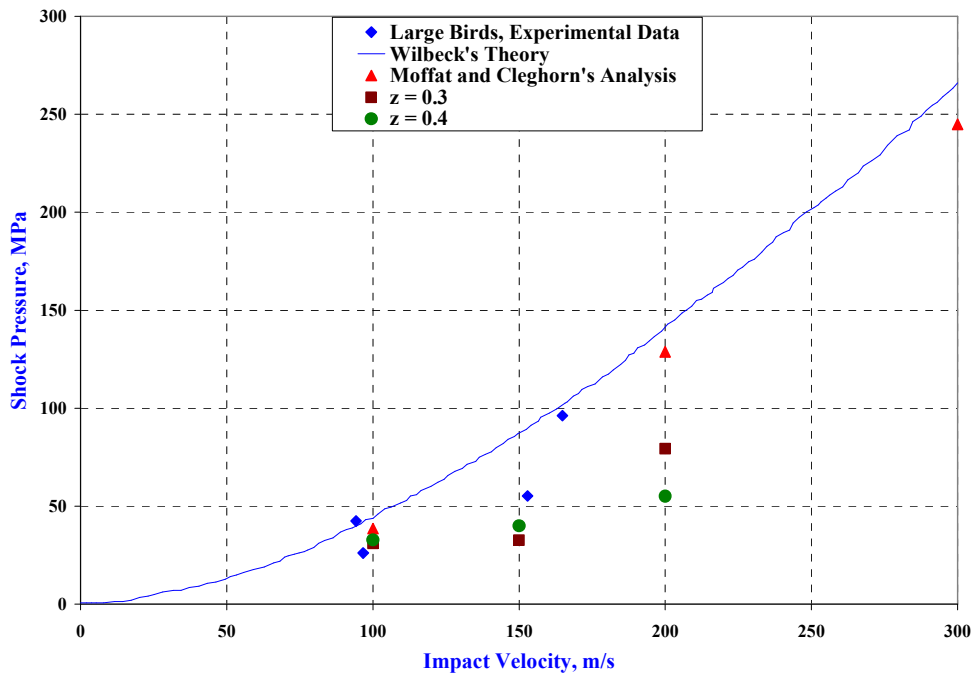


Figure 7.12. Comparison of shock pressures for impact angle of 45 degrees.

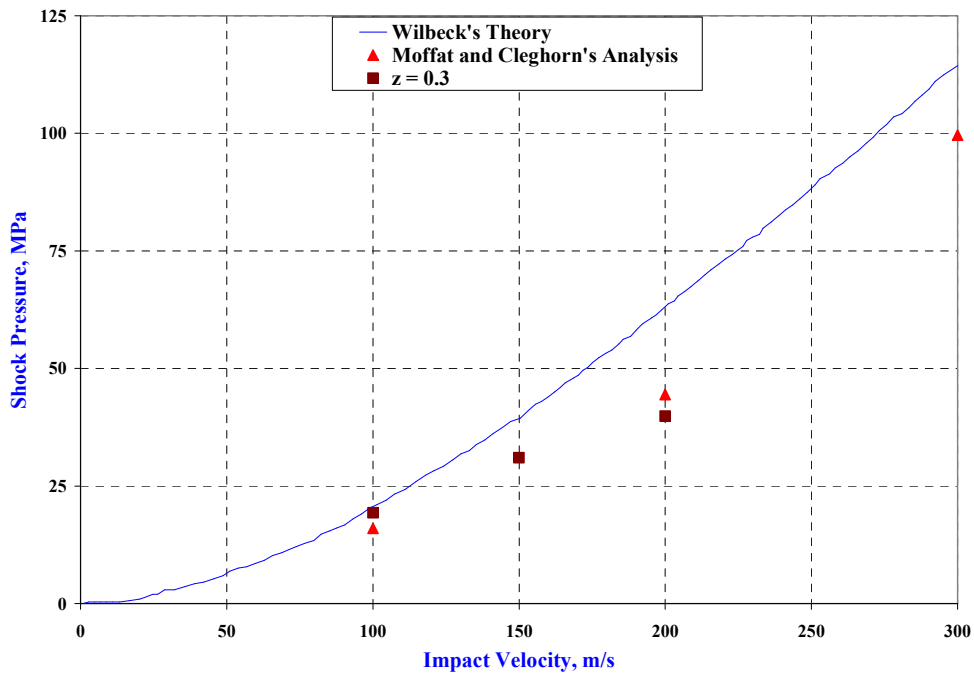


Figure 7.13. Comparison of shock pressures for impact angle of 25 degrees.

Wilbeck [8] reported that the Hugoniot shock pressures for a flexible target were lower than those obtained for a rigid target of the same material. The amount of reduction in the shock pressures depends on the target material stiffness.

For investigating the effects of target flexibility, the target was modeled as an aluminum plate. The edges of the plate were constrained in all degrees of freedom. To study the effects of target thickness, plates with thickness values of 1 mm and 5 mm were considered. The projectile was modeled as a hemi-spherical cylinder. The full impact event equation of state was used for the bird material, and a porosity of $z = 0.4$ was assumed.

The results from these investigations are presented only for qualitative treatment, since neither experimental test results nor results from other numerical analysis are available for comparison.

Snapshots of instantaneous particle displacements for the target plate of thickness 1 mm during the impact event are presented in Figure 7.14. It can be seen that the target structure failed under impact loading and a portion of the projectile particles penetrated the target.

Figure 7.15 contains the snapshots of instantaneous particle displacements for the target structure of thickness 5 mm during the impact event. As expected, increasing the thickness of the target plate improved its impact resistance. No structural failure occurred in this case, since the target structure remained intact.

Therefore, it was concluded that the current numerical method, in combination with the proposed full impact event equation of state, was capable of capturing the deformation of a flexible target during a bird strike event. In addition, the current analysis was also capable of predicting a target failure when the target structure was not strong enough to withstand the bird impact loads.

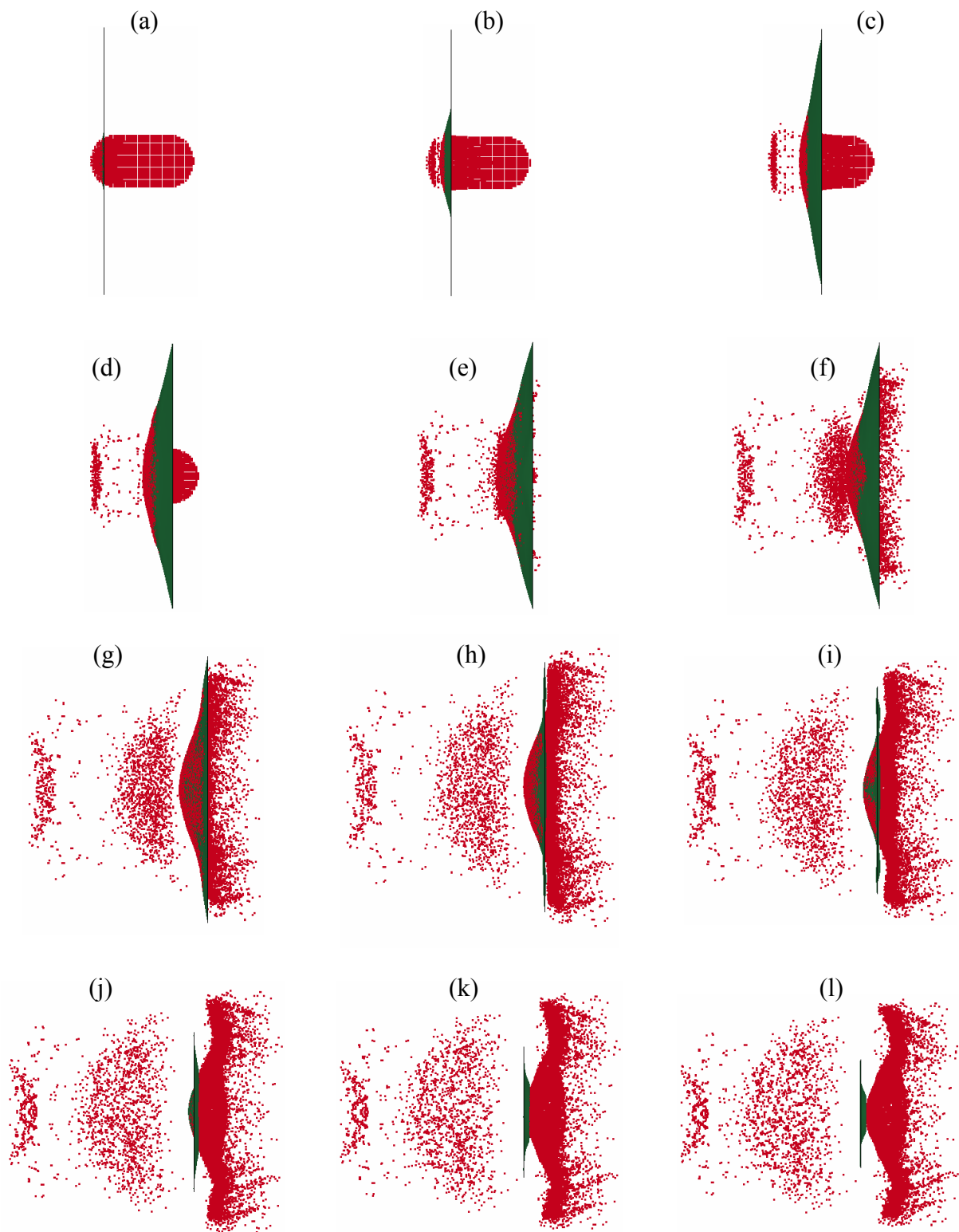


Figure 7.14. Instantaneous particle displacements for normal impact at different times during impact with a flexible flat plate of thickness 1 mm a) 0.00052 s, b) 0.0006 s, c) 0.0008 s, d) 0.001 s, e) 0.0012 s, f) 0.0014 s, g) 0.0016 s, h) 0.0018 s, i) 0.002 s, j) 0.0024 s, k) 0.0028 s and l) 0.0032 s.

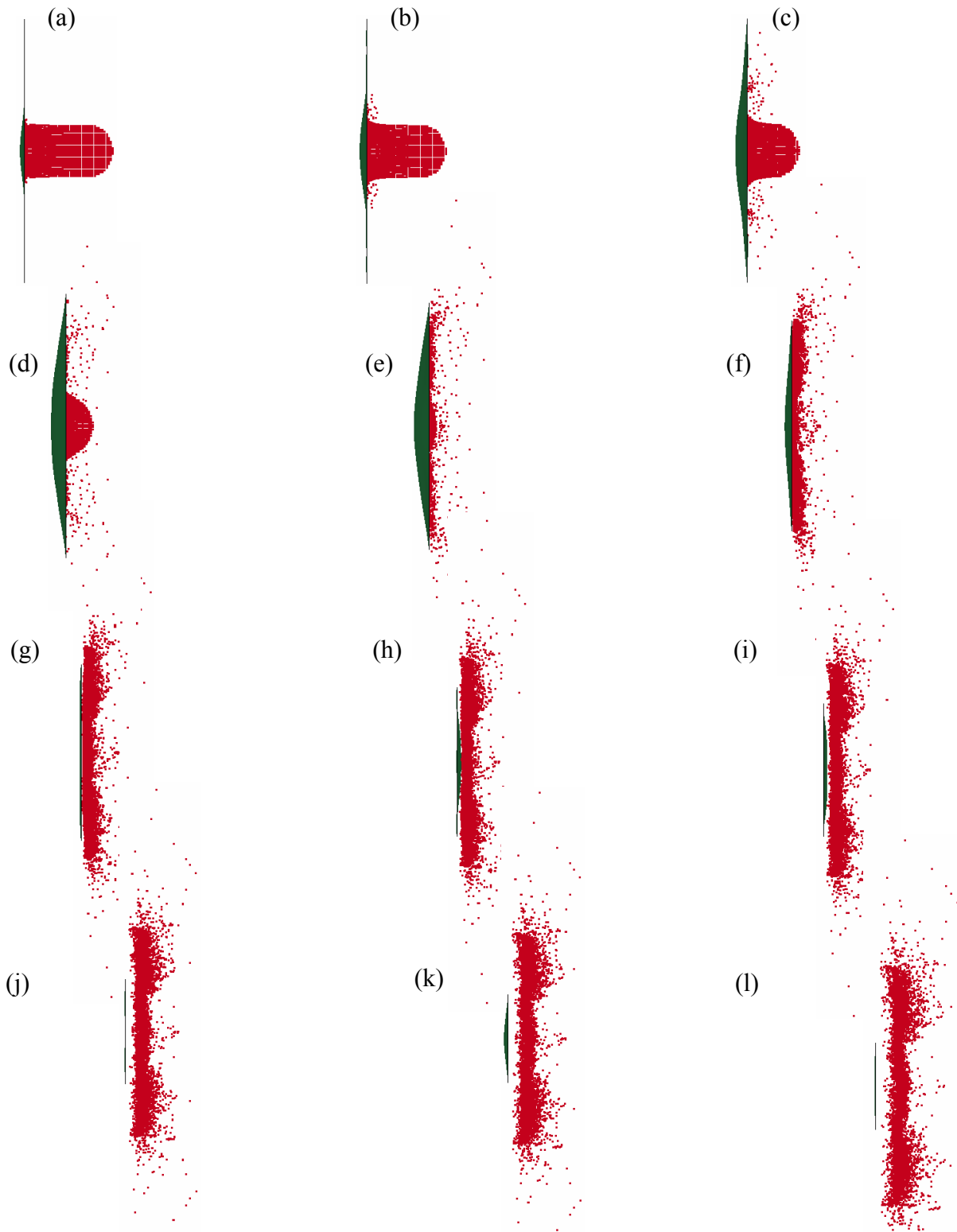


Figure 7.15. Instantaneous particle displacements for normal impact at different times during impact with a flexible flat plate of thickness 5 mm a) 0.00052 s, b) 0.0006 s, c) 0.0008 s, d) 0.001 s, e) 0.0012 s, f) 0.0014 s, g) 0.0016 s, h) 0.0018 s, i) 0.002 s, j) 0.0024 s, k) 0.0028 s and l) 0.0032 s.

7.5 Conclusion

Various projectile shapes for bird strike analysis were investigated using homogeneous material models for the bird torso. The hemi-spherical projectile proved to be the projectile shape that most closely modeled the response of actual birds during experimental tests. Equation of state models for bird material were investigated. The full impact event equation of state was validated in this research by comparing its results in numerical analyses with the results from experimental tests and other numerical analyses. Bird material porosity was found to be a significant factor in predicting precise shock pressures. In particular, porosity values of 0.3 to 0.4 were found to give the most accurate results, so they were used for subsequent analyses. The current analytical procedure was validated for both rigid and flexible target structures. In addition, the current numerical method was found to be capable of predicting correct shock pressures from an oblique impact. Finally, the current numerical method was capable of predicting the deformation of a flexible target as well as target structure failure.

CHAPTER 8

HETEROGENEOUS BIRD MODELS

Researchers typically use various primitive geometries to represent the torso of the bird in numerical simulations of bird strikes. One exception to this is the work done by McCallum and Constantinou [6], who built a complex multi-material bird model representing a Canadian goose weighing 3.6 kg. They compared the results from this multi-material bird model with the analytical results from a traditional bird torso model based on a hemi-spherical cylinder. However, they did not validate either of their numerical models by comparing them with experimental results.

McCallum and Constantinou [6] observed that for the multi-material bird model with its neck extended, the target was prestressed due to the impact of the head and neck prior to the torso. In particular, they reported that the target deformation prior to the impact of the torso was approximately 10 mm. Based on their results, McCallum and Constantinou contended that when modeling large birds, such as the Canadian goose, it is essential to model the neck, head, etc. of the bird because the initial impact of the neck and head might have important consequences on the damage initiation, which ultimately leads to failure.

Although they built a complex multi-material model, McCallum and Constantinou used the same equation of state to represent all the materials used in the multi-material bird. In fact, other than the shape difference, the only distinguishing feature of their complex model from the more traditional bird model is the slightly different densities used for various parts of the bird. However, the goal of properly representing a multi-material bird may not be accomplished by using variable densities alone. The appropriate equation of state for each material should be included.

It is also noted that the equation of state used by McCallum and Constantinou is the Grüneisen equation of state, which according to Zukas [63] is only suitable for solids with no phase change, as mentioned in Chapter 6.

Consequently, the complex multi-material model built by McCallum and Constantinou does not appear to have produced the desired results. In particular, no sharp Hugoniot peak pressure was present in their analytical pressure history plots.

In this research, the use of more rigorous multi-material bird models for predicting bird impact loads was investigated. Three types of models were selected to explore the effects of heterogeneous material models for the bird. First, a bird model was built with two discrete materials having different densities and equations of state. These two materials were randomly distributed throughout the bird torso.

It is useful to study heterogeneous bird models because real birds, like most living creatures, are not homogeneous in their composition. It turns out, however, that this first bird model, in spite of its two distinct materials, was effectively homogeneous due to the random distribution of these two materials across each cross-section of the model. Therefore, a second bird model was investigated that had a torso made of three fully separate constituents – a traditional “bird” material consisting of a homogeneous mixture of water and air, high density lumps to represent the main bone structure, and low density lumps to represent soft tissue and lungs.

Note that the previous two multi-material bird models represented only the torso of the bird like the typical bird models used in most numerical bird strike simulations. In these two models, the bird was simulated as a cylinder with hemi-spherical ends.

Finally, a third multi-material bird model was created that had a more realistic bird shape. It had the characteristic features of a real bird, such as head, neck, torso, bones, lungs and wings. This multi-material bird model was represented in the numerical simulation such that the head and neck were the same material and each of the other parts of the bird was a separate material. Each material model was distinct in that each had its own density value (different from the other materials) and an associated equation of state.

A bird with a mass of 4 kg and with an impact velocity of 150 m/s was used for all of the multi-material bird studies carried out in this research work. The reason for choosing this bird size and impact velocity was that limited experimental results are available for this particular combination from Wilbeck's [8] experimental tests.

Numerical simulations were conducted for both a rigid target and a flexible target. For each of the numerical simulations of the three types of multi-material bird models investigated in this chapter, the target structure was assumed to be rigid. In addition, target flexibility was studied with the third multi-material bird model that used the more realistic bird shape.

8.1 Randomly Distributed Multi-Material Bird

The first multi-material bird studied in this research was constructed by randomly distributing two distinct materials across each cross-section of the bird model. At each cross-section of the bird torso, 60% of the SPH particles were randomly assigned one material while the remaining SPH particles were assigned a different material. A pseudo random number generator was used to create the random distribution.

Two different sets of multi-materials were chosen for this study. The first set consisted of water with a porosity of 20% air ($z = 0.2$) in 60% of the SPH particles mixed with water with a porosity of 30% air ($z = 0.3$) in 40% of the SPH particles. The second set of multi-materials

consisted of water with a porosity of 40% air ($z = 0.4$) in 60% of the SPH particles mixed with water with a porosity of 30% air ($z = 0.3$) in 40% of the SPH particles. Note that the latter of the two multi-material birds had a composition that was very similar to the homogeneous bird material that was found to closely match the experimental results in Chapter 7.

Initial plans to use pure air mixed with either pure or porous water had to be abandoned when it was learned that the multi-material formulation within LS-Dyna currently cannot handle materials with vast density differences such as air and water.

The screenshots taken at various times during the impact for both of the multi-material birds investigated in this section are presented in Figures 8.1 and 8.2. Figure 8.3 contains the comparison of Hugoniot pressures for these multi-material birds with the experimental results. The predicted Hugoniot pressure from the first multi-material bird ($z = 0.2$ & $z = 0.3$) was much higher than the experimental results because the effective porosity of this model was less than that recommended in Chapter 7. The Hugoniot pressure from the second multi-material ($z = 0.4$ & $z = 0.3$) bird model matches well with Wilbeck's experimental results. This was expected since $z = 0.3$ to 0.4 were the recommended values for porosity of a homogeneous bird model in Chapter 7.

8.2 Multi-Material Bird with Lumps of High Density and Low Density Materials

In this section, a multi-material bird model was constructed by including lumps of higher and lower density materials within the bird torso made of a homogeneous mixture of water and air. High density lumps represent the main bone structure, and low density lumps represent the soft tissue and lungs.

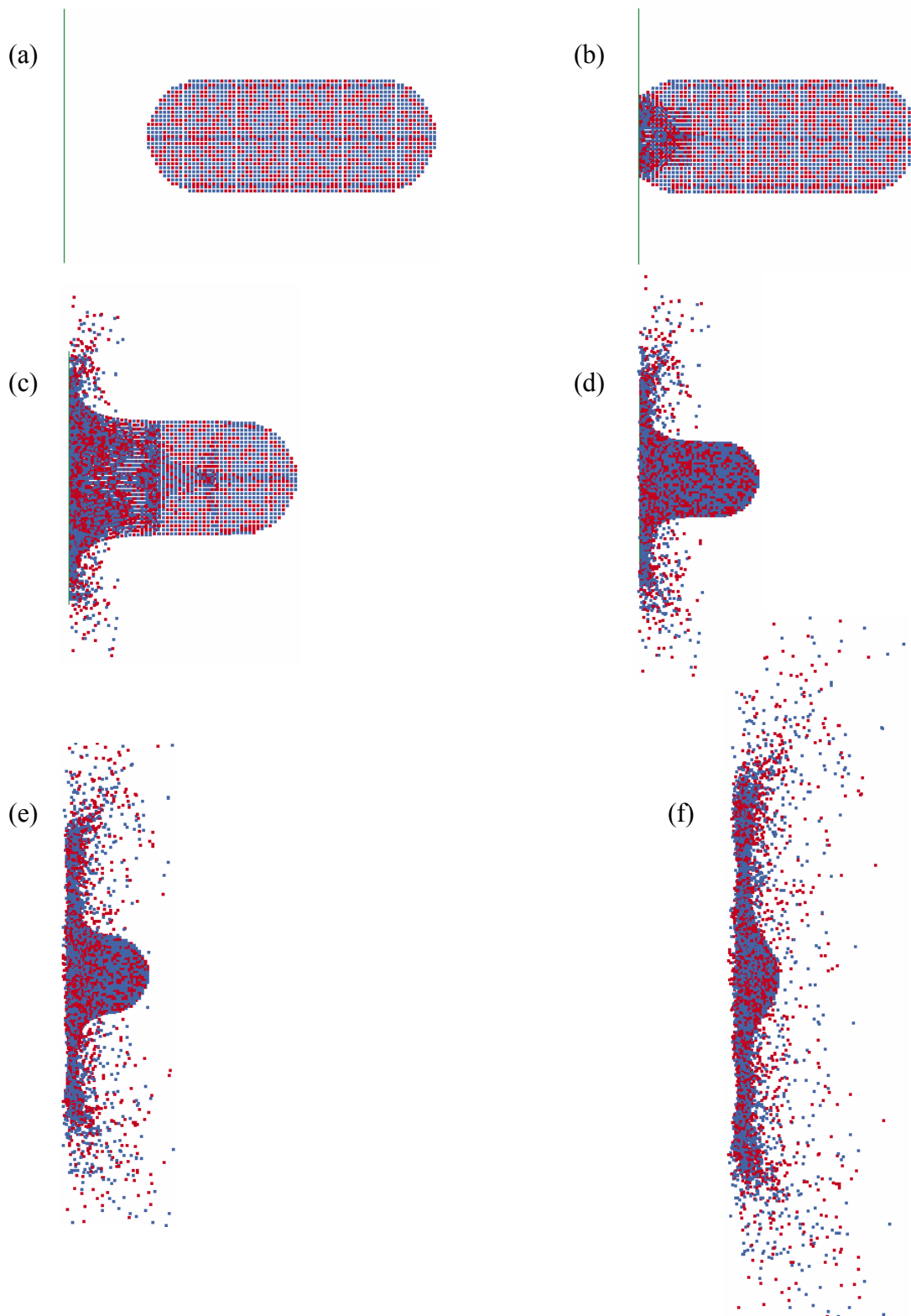


Figure 8.1. Instantaneous particle displacements for a randomly distributed, multi-material projectile ($z = 0.2$ & $z = 0.3$) at different times during impact with a rigid flat plate a) 0.0 s, b) 0.00075 s, c) 0.00116 s, d) 0.00152 s, e) 0.002 s and f) 0.00255 s.

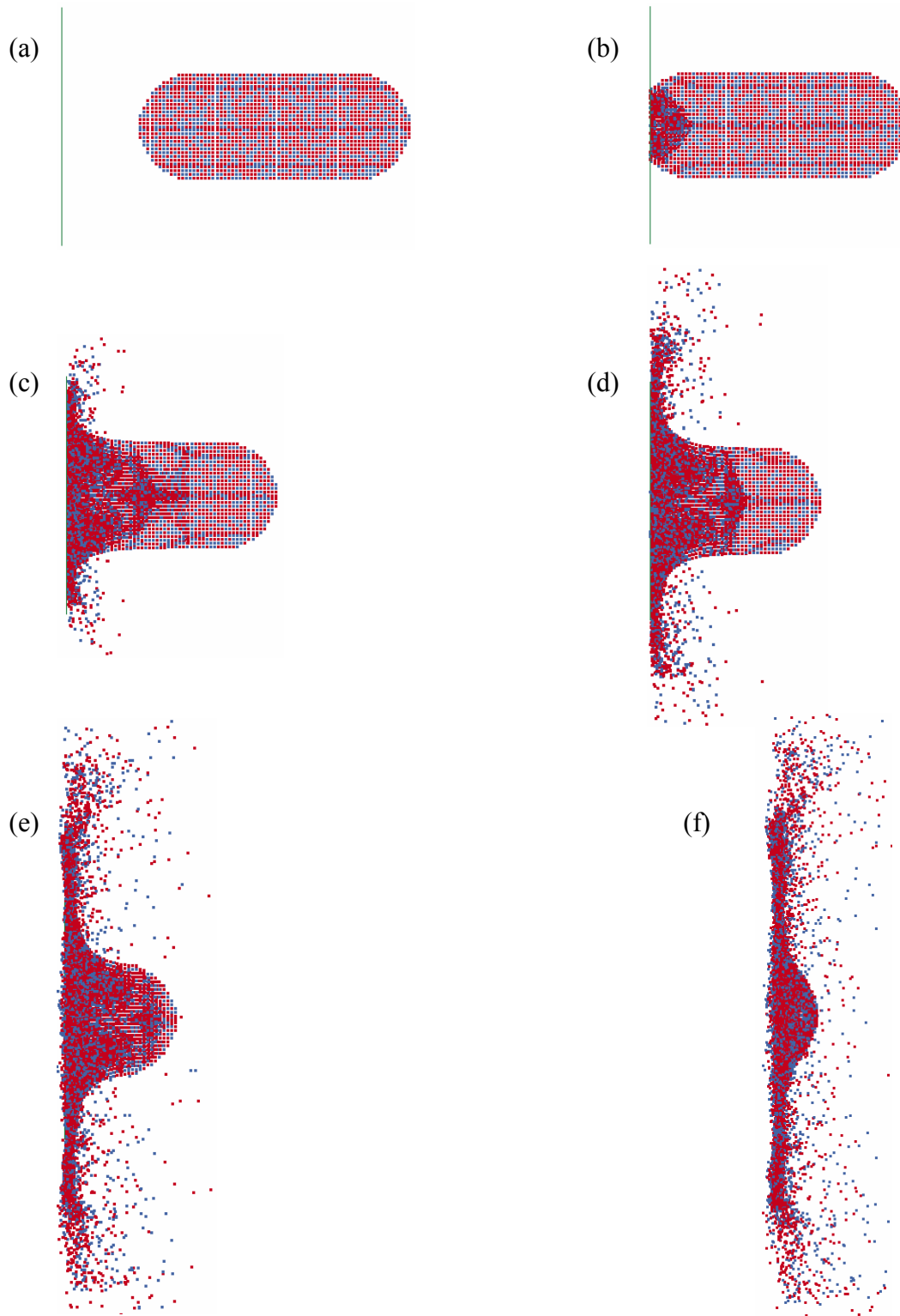


Figure 8.2. Instantaneous particle displacements for a randomly distributed multi-material projectile ($z = 0.4$ & $z = 0.3$) at different times during impact with a rigid flat plate a) 0.0 s, b) 0.00075 s, c) 0.00116 s, d) 0.00152 s, e) 0.002 s and f) 0.00255 s.

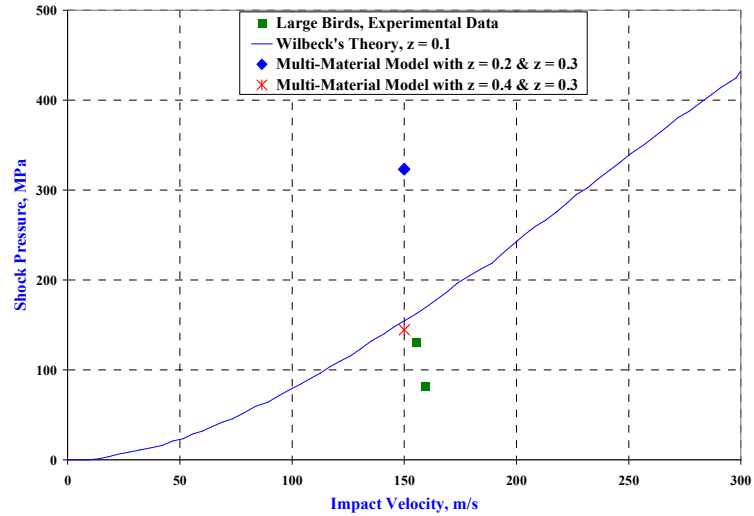


Figure 8.3. Comparison of shock pressures of multi-material birds of random distribution of two distinct materials within the bird torso with respect to Wilbeck's experimental tests and theory.

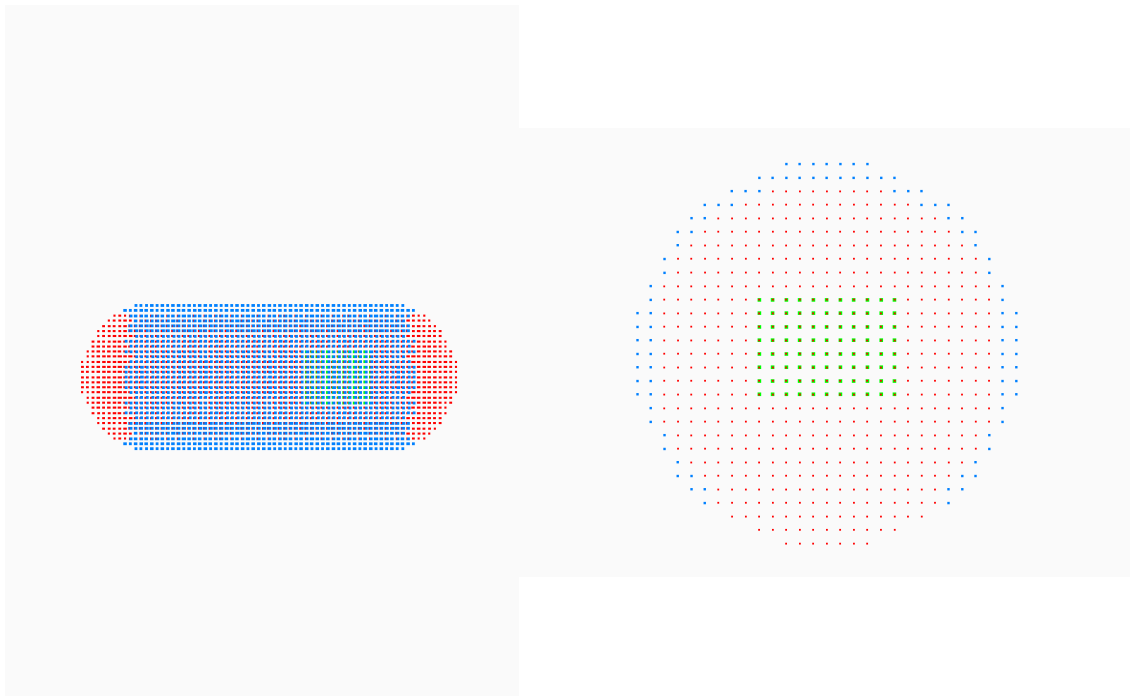


Figure 8.4. Multi-material bird model with high density lumps for bones and low density lumps for lungs.

For all the studies in this section, the bird torso had a porosity of 60% air ($z = 0.6$), and the low density lumps representing the lungs were assumed to have a porosity of 80% air ($z = 0.8$). With this combination of torso and lung materials, three different sets of materials for the high density lumps that represented the bone structure were investigated. The three materials studied for the high density lumps were – water with a porosity of 30% ($z = 0.3$), water with a porosity of 20% ($z = 0.2$) and water with a porosity of 10% ($z = 0.1$).

Figure 8.4 contains a depiction of the bird model showing the high density regions (in blue) at the outer boundary of the torso (similar to ribs) and low density regions (in green) at the center of the cross-section of the torso (similar to lungs and the surrounding soft tissue). The rest of the bird model (in red) was assigned the torso material properties.

Figure 8.5 contains the screenshots of instantaneous particle deformations for a typical bird model used in this simulation. Figure 8.6 presents the comparison of Hugoniot pressures obtained from the lumped density multi-material numerical simulations with Wilbeck's experimental results and theory. As can be seen, the numerical simulations correlate very well with the experimental tests.

It should be noted here that in all the cases investigated in this section, the peak Hugoniot shock pressure originated when the high density bone material impacted the target. Therefore, the predicted Hugoniot shock pressure was found to increase with increase in density of the bone structure material, as expected.

8.3 Multi-Material Bird with a Realistic Bird Shape

In this section, a geometrically simple bird model was built that had a shape very similar to a real bird. Head, neck and wings were included in the bird model in addition to the bird torso (including high density bones as well as low density lungs) studied up to this point. This model

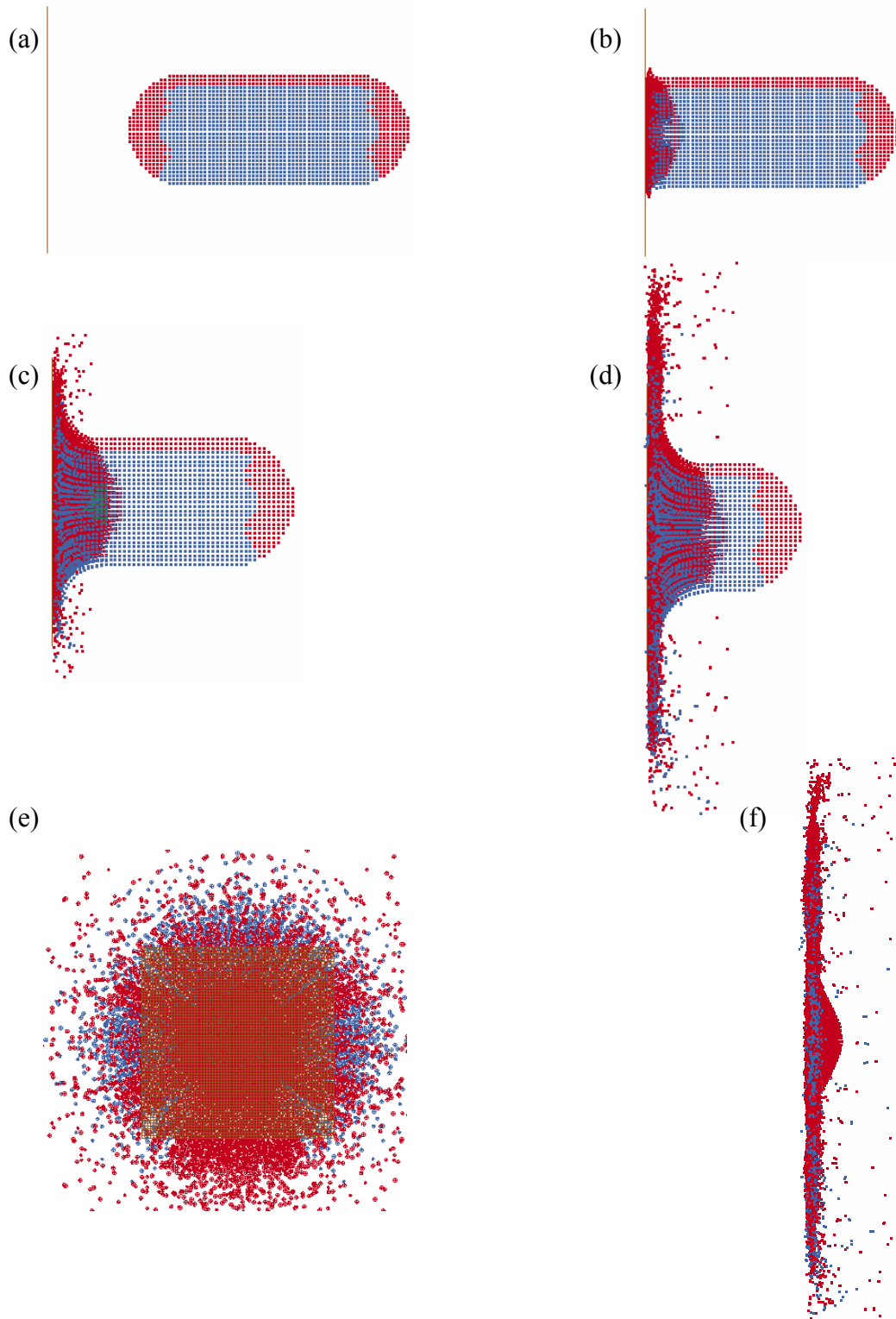


Figure 8.5. Instantaneous particle displacements for a multi-material projectile with high density and low density lumps at different times during impact with a rigid flat plate a) 0.0 s, b) 0.0009 s, c) 0.00126 s, d) 0.00186 s, e) 0.00186 s (cross-sectional view) and f) 0.00271 s.

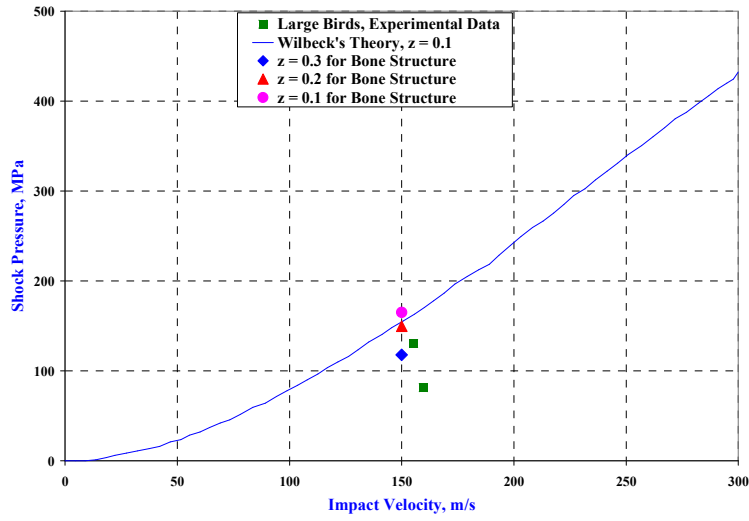


Figure 8.6. Comparison of shock pressures for multi-material birds with high density lumps for bone structure and low density lumps for soft tissue and lungs ($z = 0.8$) within the bird torso ($z = 0.6$).

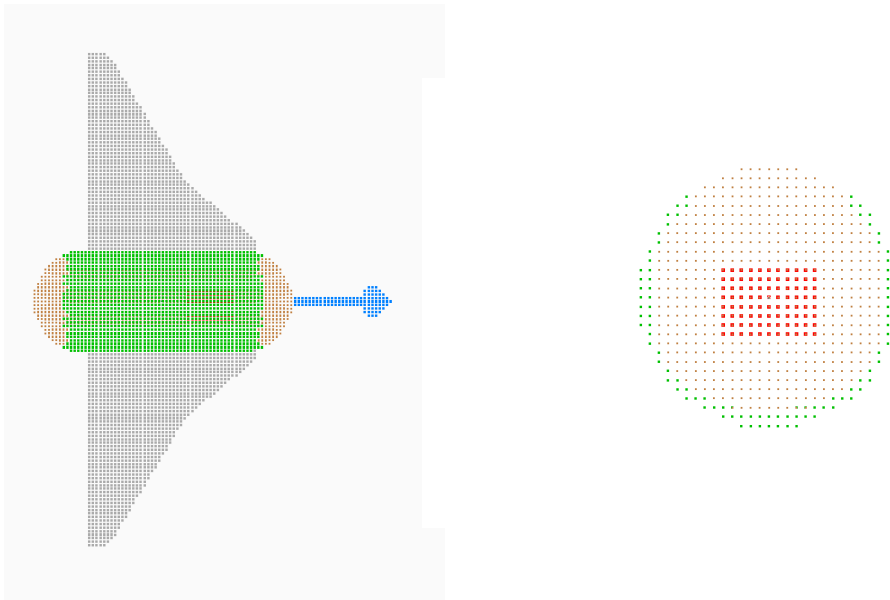


Figure 8.7. Multi-material bird model with a realistic bird shape.

consisted of 5 different materials – one material for head and neck, a high density material for bone structure, a low density material for lungs and the surrounding soft tissue, another low density material for wings and a different material for the torso.

Note that neither the physical dimensions nor the material properties were the exact replica of any specific bird. Instead, they were representative of birds in general. There were two reasons for this – the first was, for the very limited experimental results available for large birds, the associated details such as the exact physical dimensions and material properties were unknown. The second reason was that the purpose of this research work was to qualitatively demonstrate the capabilities of a multi-material bird model for predicting bird impact loads, given the scarcity of experimental results for large birds.

In this section, the effect of independently increasing the density of the materials used for the bone structure, head and neck, and the torso of the bird were investigated, while keeping the density of the low density materials (lungs and wings) constant.

Figure 8.7 contains an illustration of the typical multi-material bird model used in all of the numerical simulations of this section. The material used for the head and neck is shown in blue, the torso material is shown in brown, the material for bone structure can be seen in green, the material for wings is depicted in grey, and the low density lung material is shown in red.

Note that in some views, material nodes block the view of other materials that are behind them.

The study of multi-material birds with realistic bird shapes was subdivided into four categories to study the effects of material density and target flexibility. First, the effect of increasing the density of the head and neck material alone was investigated. Next, the effect of increasing the density of the material used to represent the bone structure was studied. This was

followed by the study of the effect of increasing the density of the torso. For all these investigations, a rigid target was considered.

Finally, target flexibility was included as a factor in the analysis, and the effect of increasing the density of the head and neck material on target deformation was explored.

Figures 8.8 and 8.9 depict the screenshots at various times during the bird deformation and segmentation as it impacts a rigid target. The gap in these figures between the target and the projectile represents the thickness of the target.

8.3.1 Effect of Increasing the Density of Head and Neck Material

The effects of variations in material density (porosity) of the head and neck are shown in Figures 8.10 through 8.12. These figures contain the time history of maximum pressures generated as various parts of the multi-material bird impact the target structure. The material used for the head and neck had a porosity of 30% ($z = 0.3$) in Figure 8.10, 10% ($z = 0.1$) in Figure 8.11, and no porosity ($z = 0.0$) in Figure 8.12. Note that in all of these three simulations the torso material had a porosity of 60% air ($z = 0.6$), the bone material had a porosity of 20% air ($z = 0.2$), the lung material had a porosity of 80% air ($z = 0.8$), and the material porosity for the wings was 70% air ($z = 0.7$). These figures provide some insight into the impact behavior of a real bird. The peak impact pressure for each part of the bird was captured through these pressure history plots.

As expected, the maximum pressure resulting from the head impact increased with an increase in the density (reduction in porosity) of head and neck material. In addition, it can be seen from the figures that the highest impact pressures resulting from the torso impact and the bone structure impact remained approximately the same, since the densities of these materials were held constant in all these simulations.

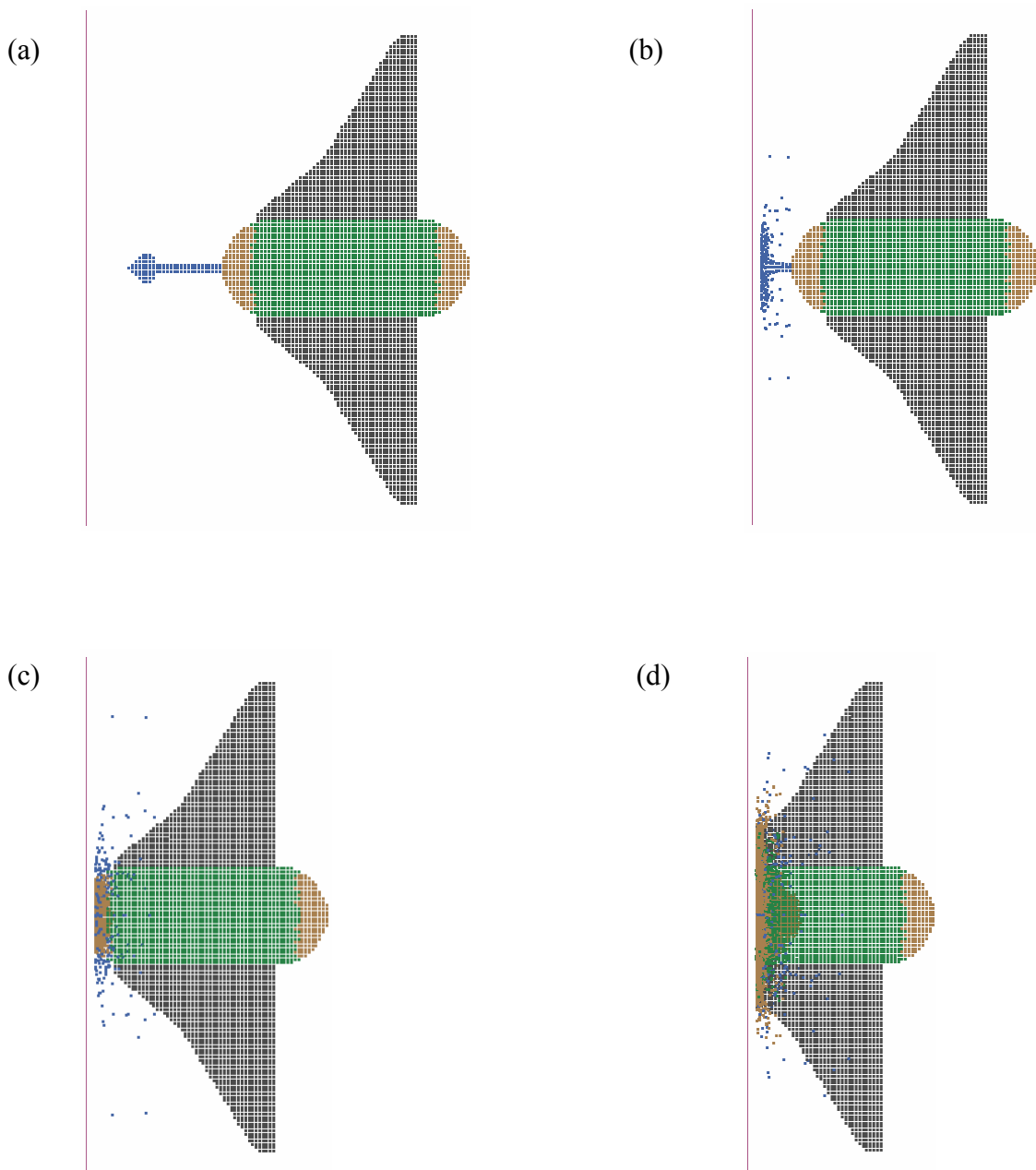


Figure 8.8. Instantaneous particle displacements for a multi-material projectile at different times during impact with a rigid flat plate a) 0.0 s, b) 0.0009 s, c) 0.00133 s and d) 0.00182 s.

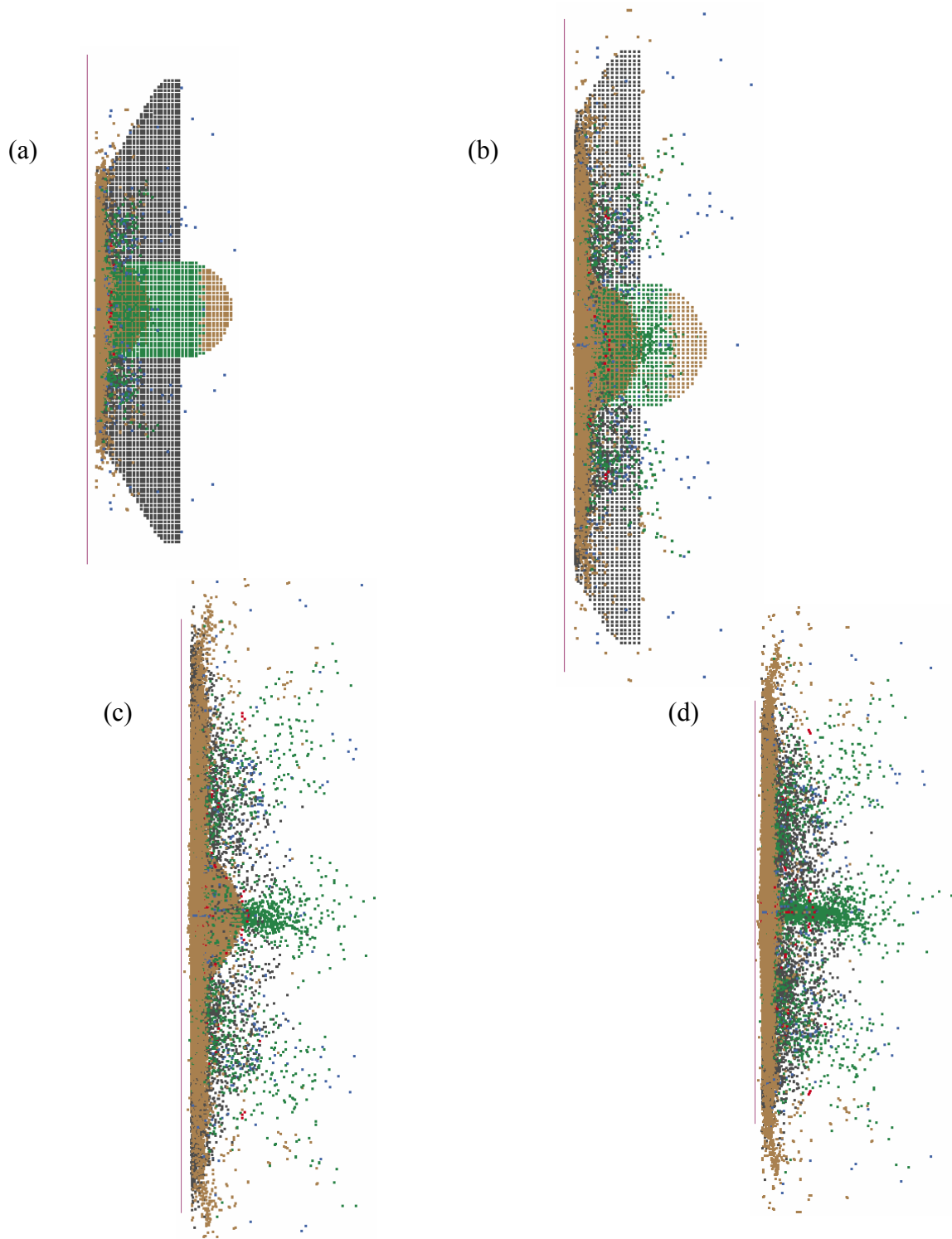


Figure 8.9. Instantaneous particle displacements for a multi-material projectile at different times during impact with a rigid flat plate (continued from Figure 8.8) a) 0.0022 s, b) 0.0025 s, c) 0.0031 s and d) 0.0035 s.

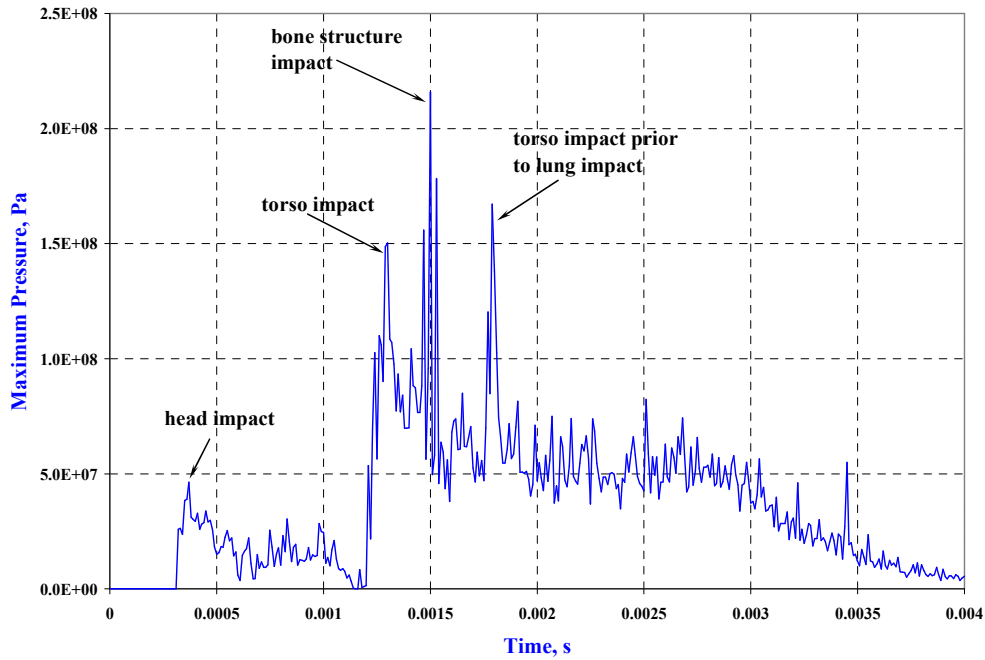


Figure 8.10. Time history of maximum pressure for the multi-material bird with 30% porosity ($z = 0.3$) for the head and neck material.

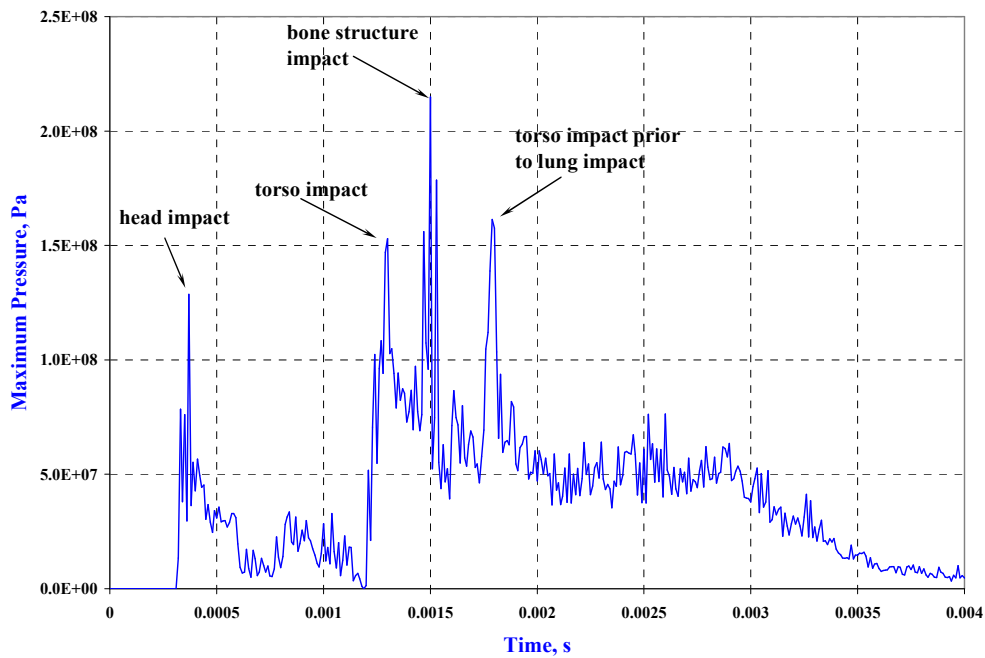


Figure 8.11. Time history of maximum pressure for the multi-material bird with 10% porosity ($z = 0.1$) for the head and neck material.

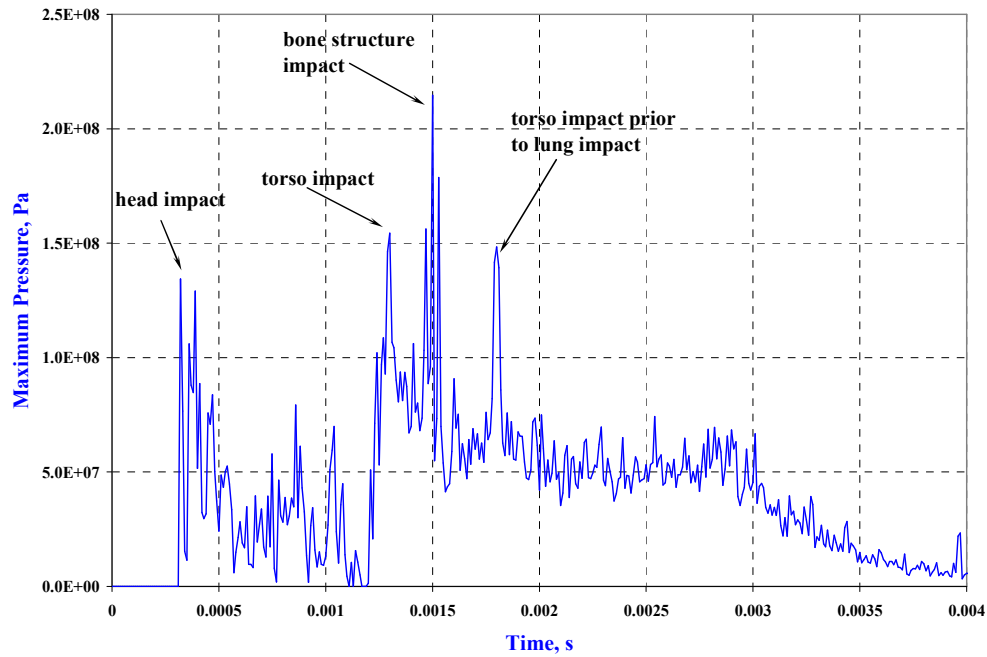


Figure 8.12. Time history of maximum pressure for the multi-material bird with no porosity ($z = 0.0$) for the head and neck material.

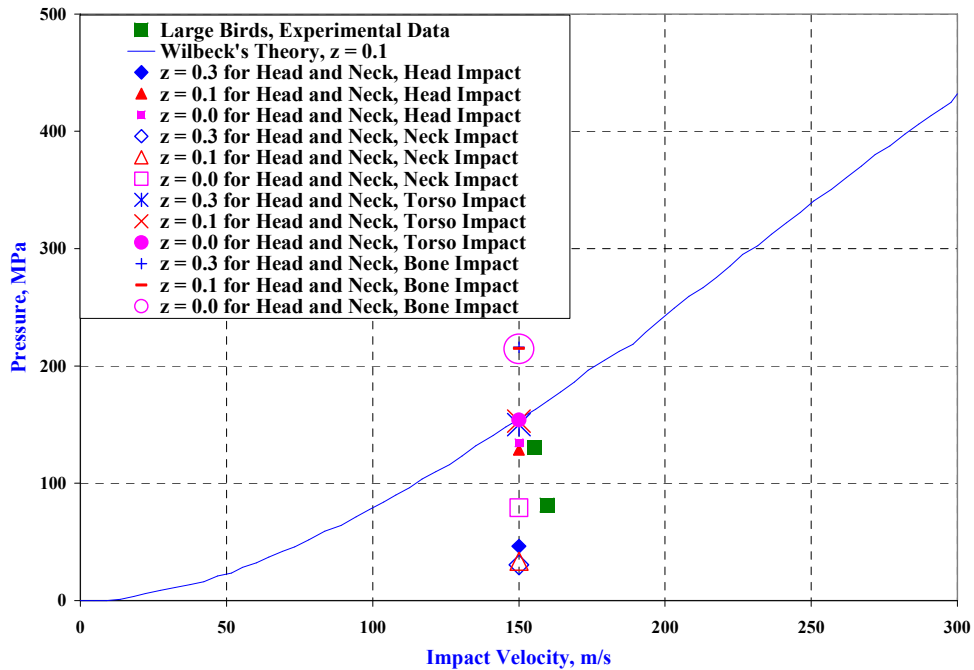


Figure 8.13. Comparison of maximum pressures generated from the impact of various parts of the three multi-material bird models.

Figure 8.13 summarizes the effects of increasing the material density (reducing the porosity) of the head and neck. The main peaks shown in Figures 8.10 thru 8.12 are summarized, and experimental results for the impact of a 4 kg bird at an impact velocity of 150 m/s on a rigid target are also included in this figure.

8.3.2 Effect of Increasing the Density of Bone Structure Material

During the investigation of the effect of increasing the material density of the bone structure, three different materials were considered – material with a porosity of 20% ($z = 0.2$), material with 10% porosity ($z = 0.1$) and a material with no porosity ($z = 0.0$). For all of these simulations, the torso of the bird was assumed have a porosity of 60% ($z = 0.6$), a 30% porosity ($z = 0.3$) was assigned to the head and neck material, the material used for lungs was assigned a porosity of 80% ($z = 0.8$), and the material for the wings was assumed to have a porosity of 70% ($z = 0.7$).

The time history plots of maximum pressures generated for models with various bone densities are presented in Figures 8.10 (which is repeated here for convenience), 8.14 and 8.15. Figure 8.16 contains the comparison of the maximum pressures generated for these three cases along with Wilbeck's experimental test results. As expected, the maximum pressure resulting from the bone structure impact increases with an increase in its density (reduction in porosity). In addition, it can be seen from these figures that the highest impact pressures resulting from the head impact and the torso impact remains approximately the same since the densities of these materials were held constant in all these simulations.

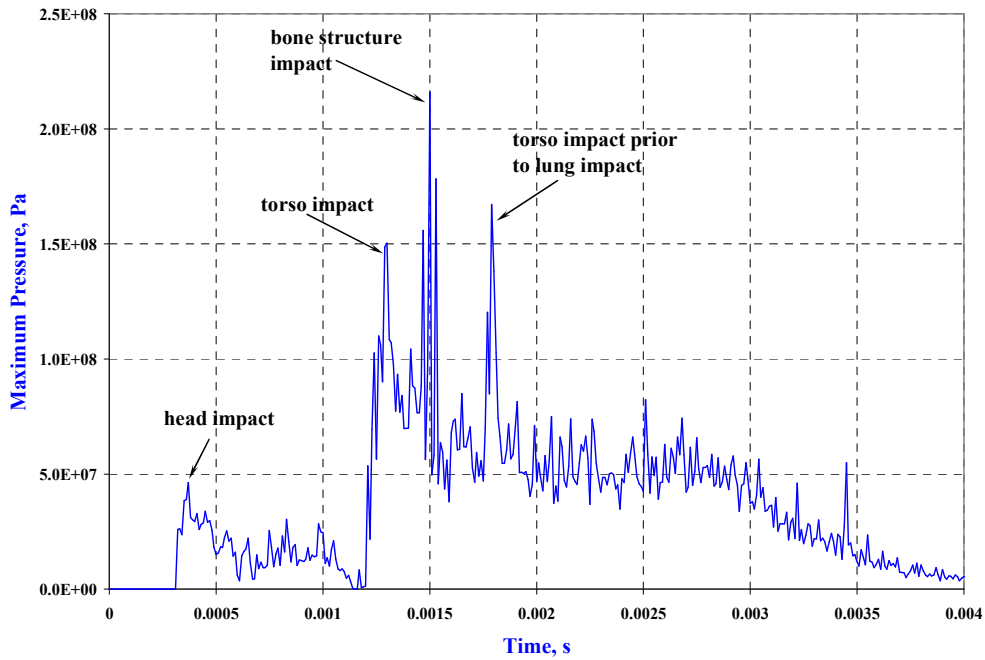


Figure 8.10. Time history of maximum pressure for the multi-material bird with 20% porosity ($z = 0.2$) for the bone material.

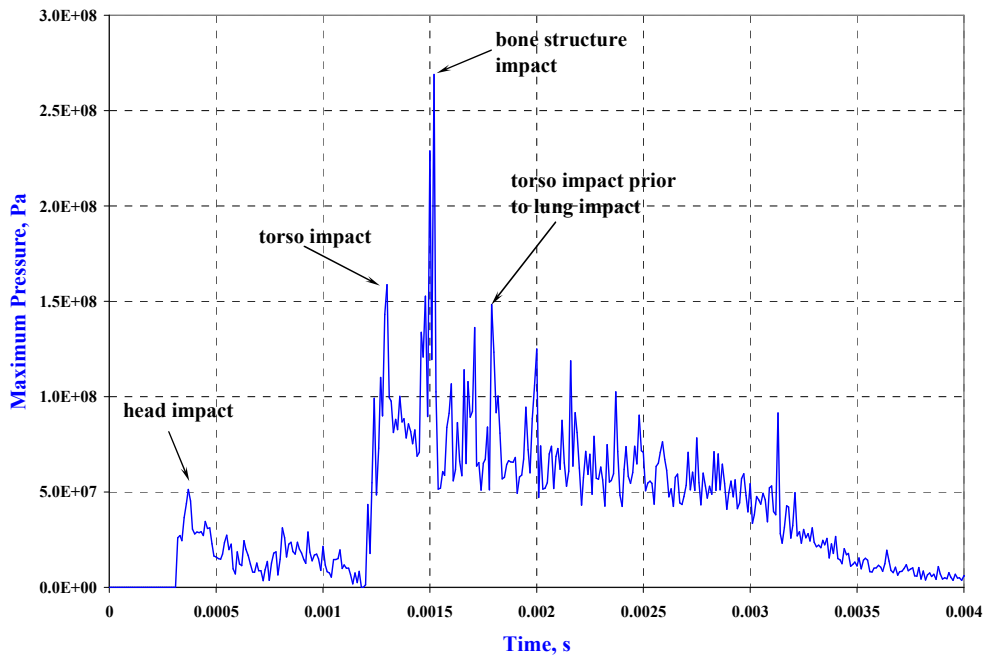


Figure 8.14. Time history of maximum pressure for the multi-material bird with 10% porosity ($z = 0.1$) for the bone material.

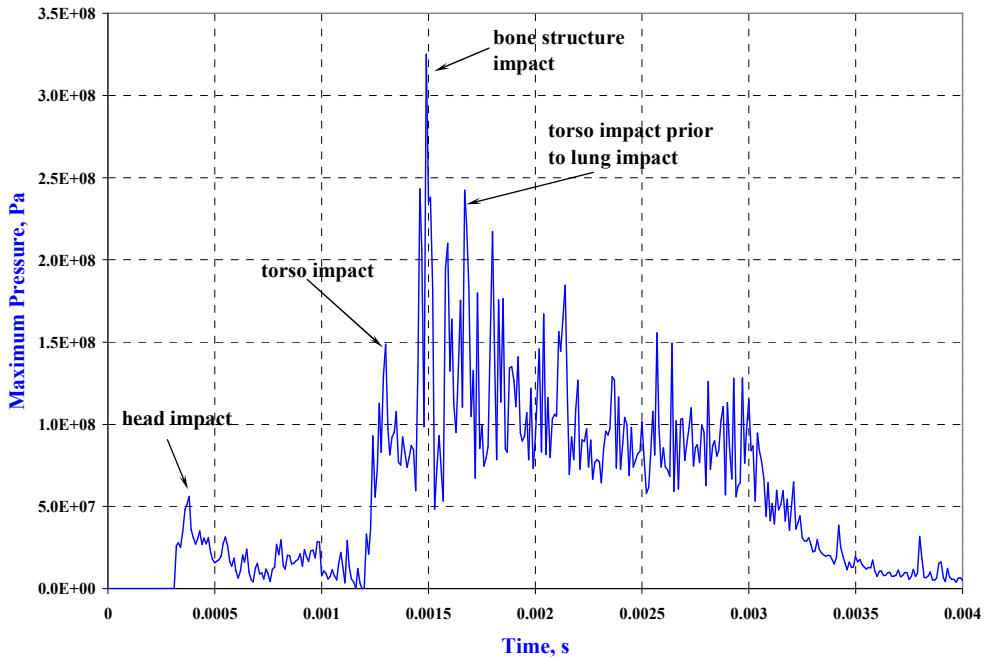


Figure 8.15. Time history of maximum pressure for the multi-material bird with no porosity ($z = 0.0$) for the bone material.

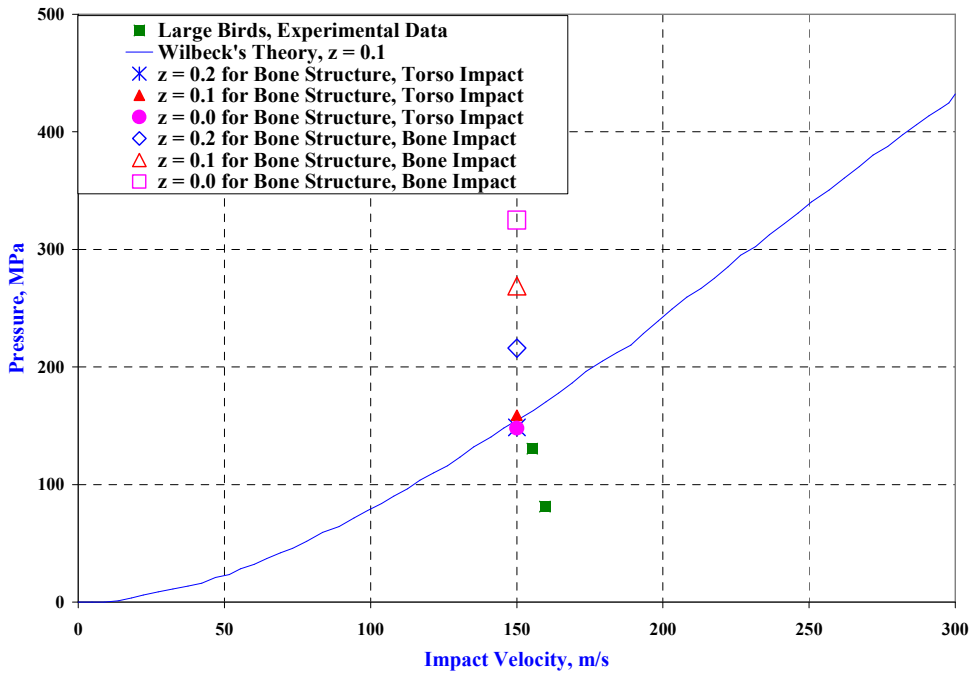


Figure 8.16. Effect of an increase of the density in the bone material on the maximum pressures generated from the impact of various parts for the three multi-material bird models.

8.3.3 *Effect of Increasing the Density of Torso Material*

In Chapter 7, the effect of material porosity on impact pressures was thoroughly investigated for a homogeneous bird material model. In this section, the effect of increasing the bird torso density (reducing porosity) was studied for a multi-material bird.

Three different materials for the bird torso were considered – material with a porosity of 60% ($z = 0.6$), material with 50% porosity ($z = 0.5$), and a material with 40% porosity ($z = 0.4$). Note that higher porosity values than those recommended ($z = 0.3$ to 0.4) in Chapter 7 for a homogeneous torso, were chosen to offset the higher density (lower porosity) materials, such as head, neck, and bone structure used in the multi-material bird. For all of these simulations, a 30% porosity ($z = 0.3$) was assigned to the head and neck material, 20% ($z = 0.2$) to the bone structure, 80% ($z = 0.8$) for the lungs, and 70% ($z = 0.7$) for the wings.

The time history plots of the maximum pressures generated for these models with various torso densities are presented in Figures 8.10 (which is repeated here for convenience), 8.17 and 8.18. Figure 8.19 contains a comparison of the maximum pressures generated for these three cases along with the experimental test results. Recall that in Chapter 7, it was concluded that a homogeneous bird model with a porosity of 30% or 40% ($z = 0.3$ or 0.4) predicts the impact pressures with reasonable accuracy. However, a multi-material bird model with high density lumps might require a torso material that has slightly higher porosity to reproduce the same results as a homogeneous bird model.

One discrepancy was noticed in the figures presented in sub-section 8.3.3. The pressures resulting from the head impact varied between Figures 8.10, 8.17 and 8.18, even though the density of the head material was held constant for these three cases. It should be noted here that mass assigned to each SPH particles of the head for these three cases was not constant even

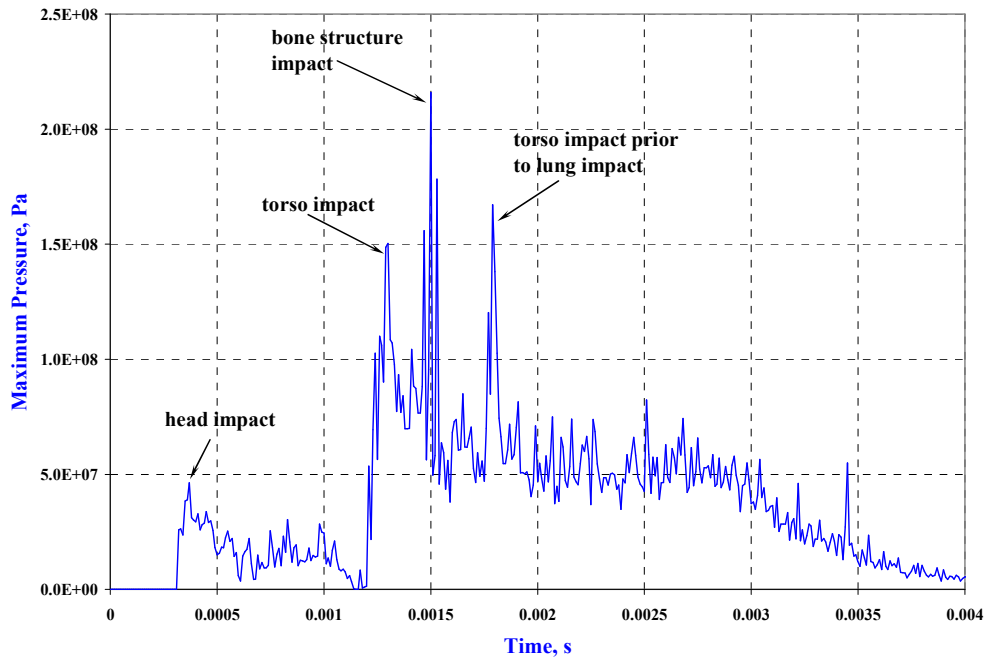


Figure 8.10. Time history of maximum pressure for the multi-material bird with 60% porosity ($z = 0.6$) for the torso material.

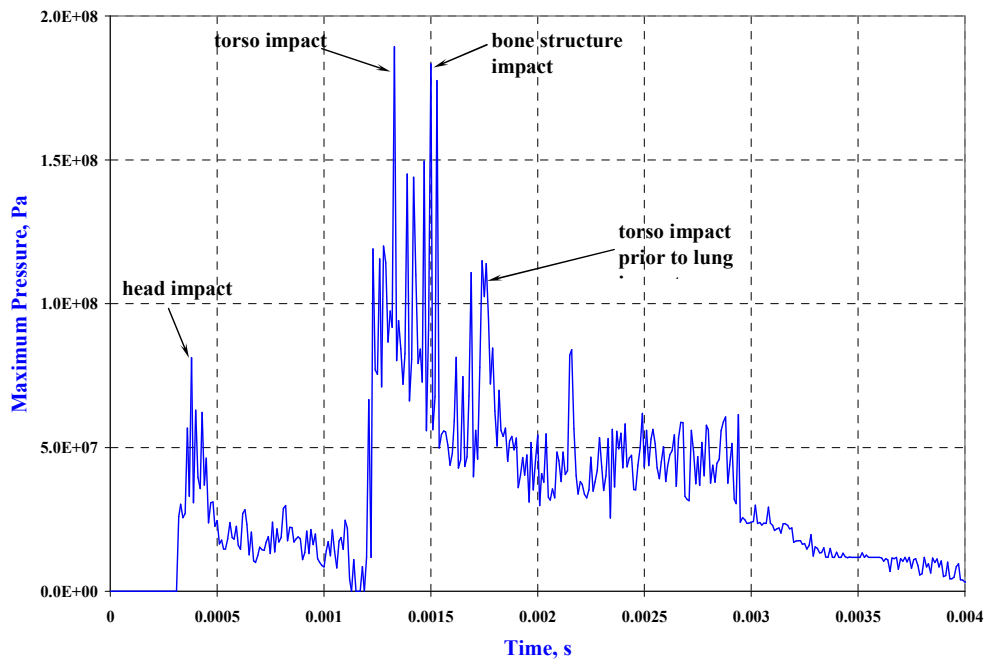


Figure 8.17. Time history of maximum pressure for the multi-material bird with 50% porosity ($z = 0.5$) for the torso material.

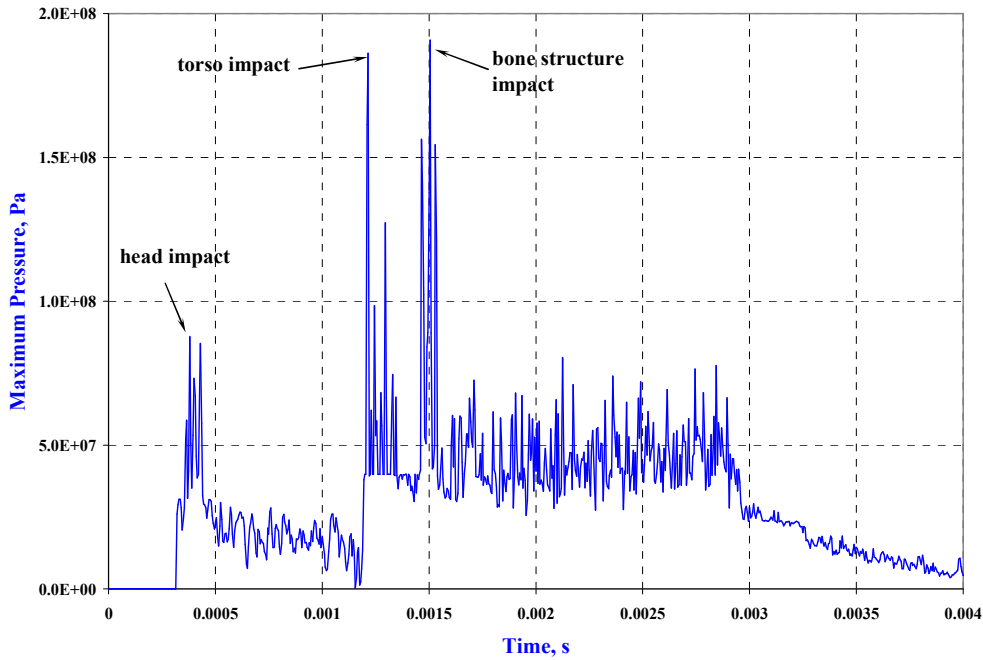


Figure 8.18. Time history of maximum pressure for the multi-material bird with 40% porosity ($z = 0.4$) for the torso material.

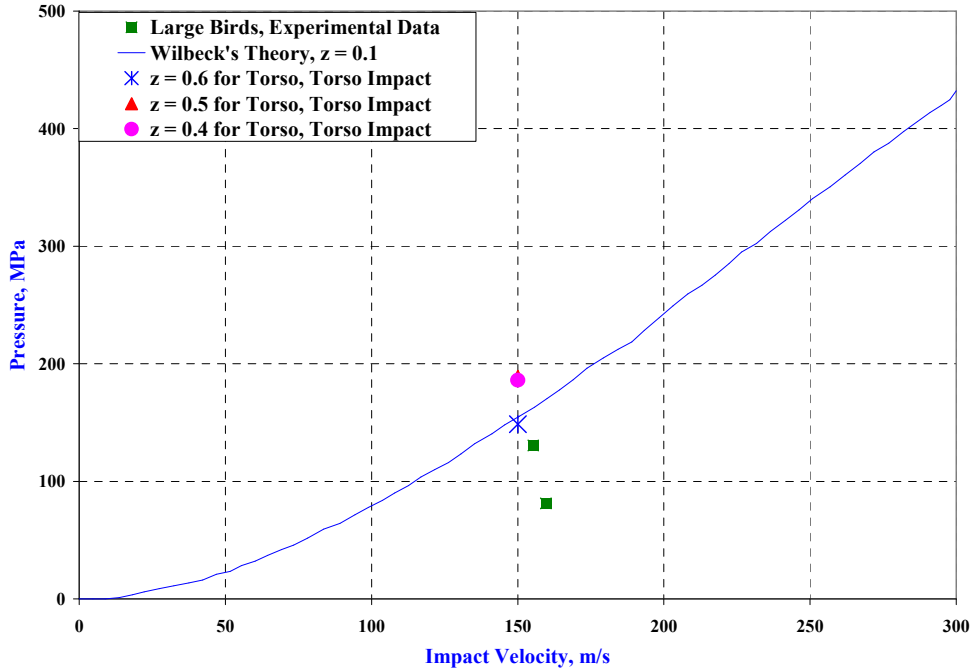


Figure 8.19. Effect of an increase in the density of the torso material on the maximum pressures generated from the impact of the bird torso for the three multi-material bird models investigated.

when the density was held constant. This was done to ensure that the higher density torso materials had a proportionately higher mass, while maintaining the same overall mass of the bird. This can adversely affect the local impact pressures resulting from the head impact. However, similar results did not occur while varying the densities of the head and neck material or the bone structure material (sub-sections 8.3.1 and 8.3.2), because these parts represent a relatively small portion of the total mass of the bird.

It is emphasized that the time history plots of maximum pressures presented in Section 8.3 are the “maximum” pressures generated at any point in the bird model at a given instant during the impact event. Contiguous points in the plots rarely belong to the same SPH particle. The maximum pressure peaks should not be confused with the steady state pressures that the bird experiences as the impact event enters the steady state phase.

8.3.4 Effect of Increasing the Density of Head and Neck Material on the Deformation of the Target

In this section, the effect of increasing the density of the head and neck material on target deformation was explored. This is of particular interest because McCallum and Constantinou [6], reported that the impact of a long, extended neck may have important consequences on damage initiation. Based on their investigations, they reported that an aluminum target with a thickness of 10 mm had a deflection of 10 mm as a result of the neck impact.

In this research, the effect of including the head and neck impact of a large bird on a flexible, 10 mm thick aluminum target was also studied. Two different materials, one with porosity of 30% air ($z = 0.3$) and the other with no porosity ($z = 0.0$), were used for the head and neck. In both cases, the bird torso had 60% porosity ($z = 0.6$), bone material had 20% porosity ($z = 0.2$), lungs had 80% porosity ($z = 0.8$), and the wings had 70% porosity ($z = 0.7$).

Figures 8.20 and 8.21 depict the instantaneous target deformations at various times for the 30% porous ($z = 0.3$) head and neck material in the bird model. Figures 8.22 and 8.23 present the instantaneous target deformations at various times for the non-porous ($z = 0.0$) head and neck material. From these figures, it can be seen that the deformation patterns of the targets were very similar for both cases.

Figure 8.24 contains a comparison of target deformation resulting from these two different bird models. It can be seen that in both cases, the head and neck impact resulted in some target deformation. As expected, the deformation resulting from the bird model with non-porous ($z = 0.0$) head and neck model was greater. However, in neither case did the target deformation exceed 3 mm from the head and neck impact, which is much smaller than the 10 mm deformation computed by McCallum and Constantinou with their analytical simulations [6]. It should be noted here that the mass of the bird used by McCallum and Constantinou was 3.6 kg and had a velocity of 180 m/s. As mentioned before, the current work used a 4 kg bird at 150 m/s in order to compare results with Wilbeck's [8] experimental results. McCallum and Constantinou did not validate their analytical model with experimental results. In addition, the exact dimensions of their bird model were not reported.

The multi-material bird model used in the current research was expected to produce lower target deflection than that predicted by McCallum and Constantinou [6]. This is because the maximum pressures predicted by the various multi-material models used in the current research were lower than those predicted by McCallum and Constantinou. As noted earlier in this chapter, they used the same equation of state to represent all the materials in their multi-material bird, and the equation of state they used was, according to Zukas [63], only suitable for solids. It should be noted here that the multi-material models used in this research were

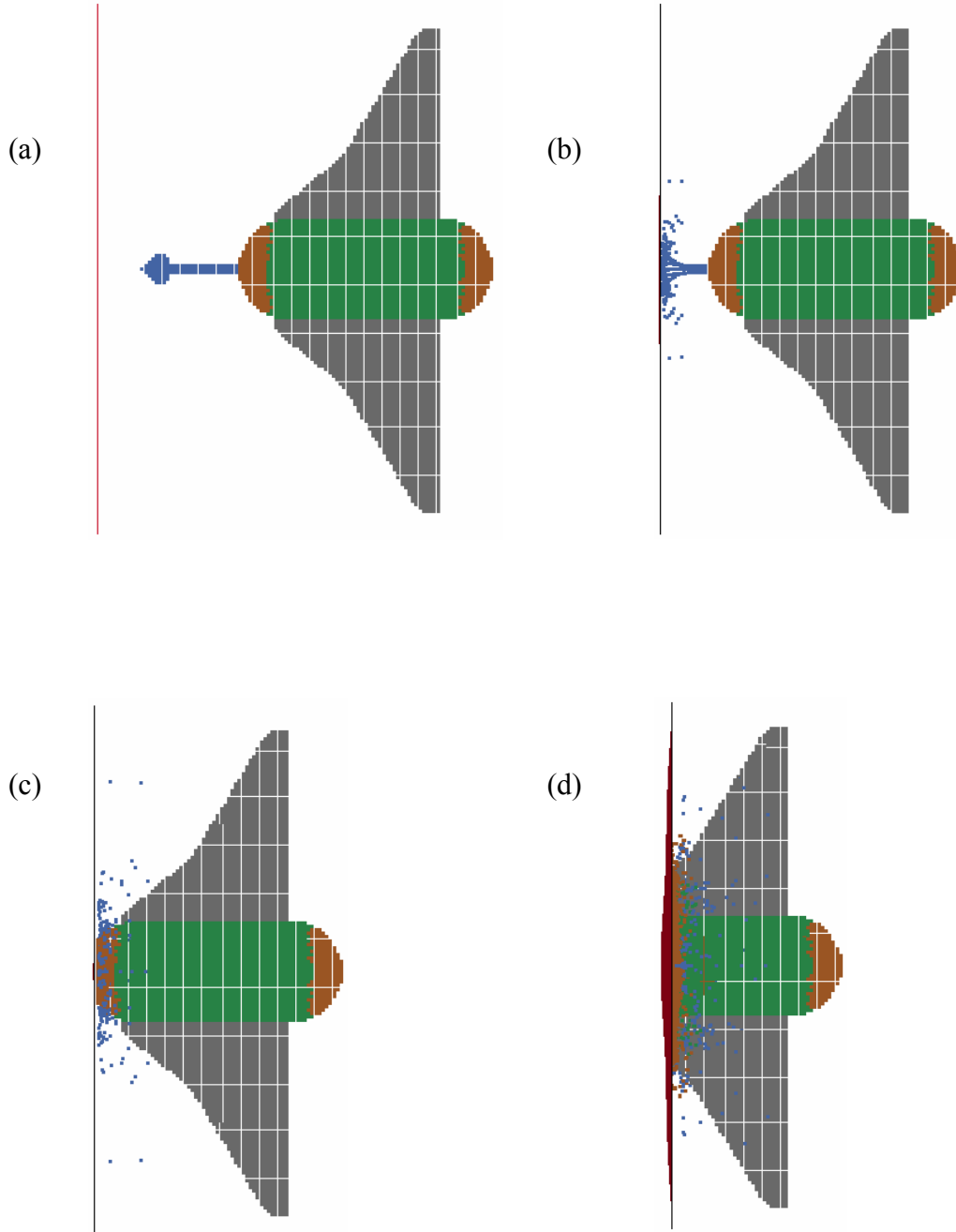


Figure 8.20. Instantaneous particle displacements for a multi-material projectile with $z = 0.3$ for the head and neck, at different times during impact with a flexible flat plate a) 0.0 s, b) 0.0008 s, c) 0.0013 s and d) 0.002 s.

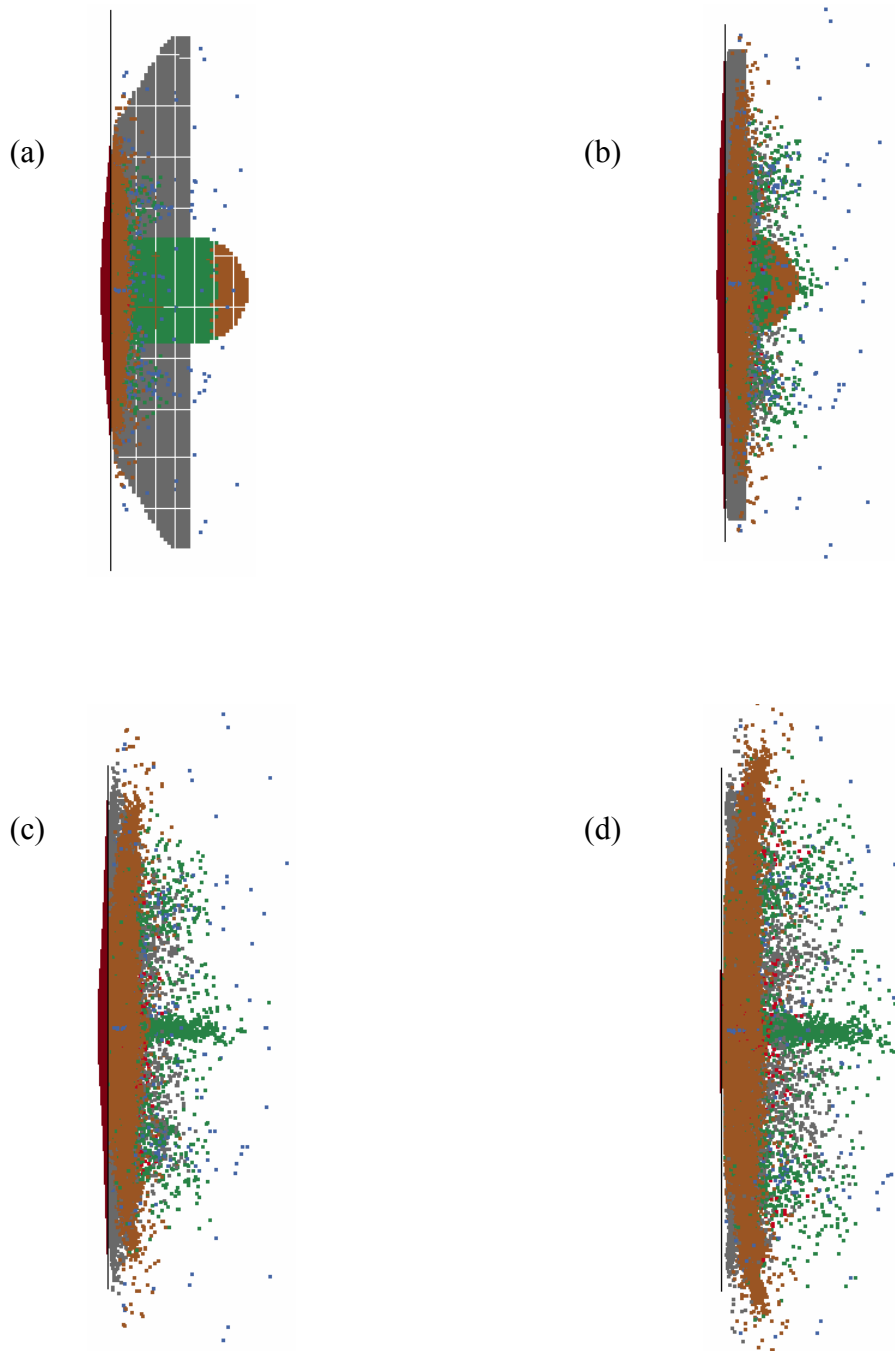


Figure 8.21. Instantaneous particle displacements for a multi-material projectile with $z = 0.3$ for the head and neck, at different times during impact with a flexible flat plate (continued from Figure 8.20) a) 0.024 s, b) 0.00287 s, c) 0.0032 s and d) 0.0037 s.

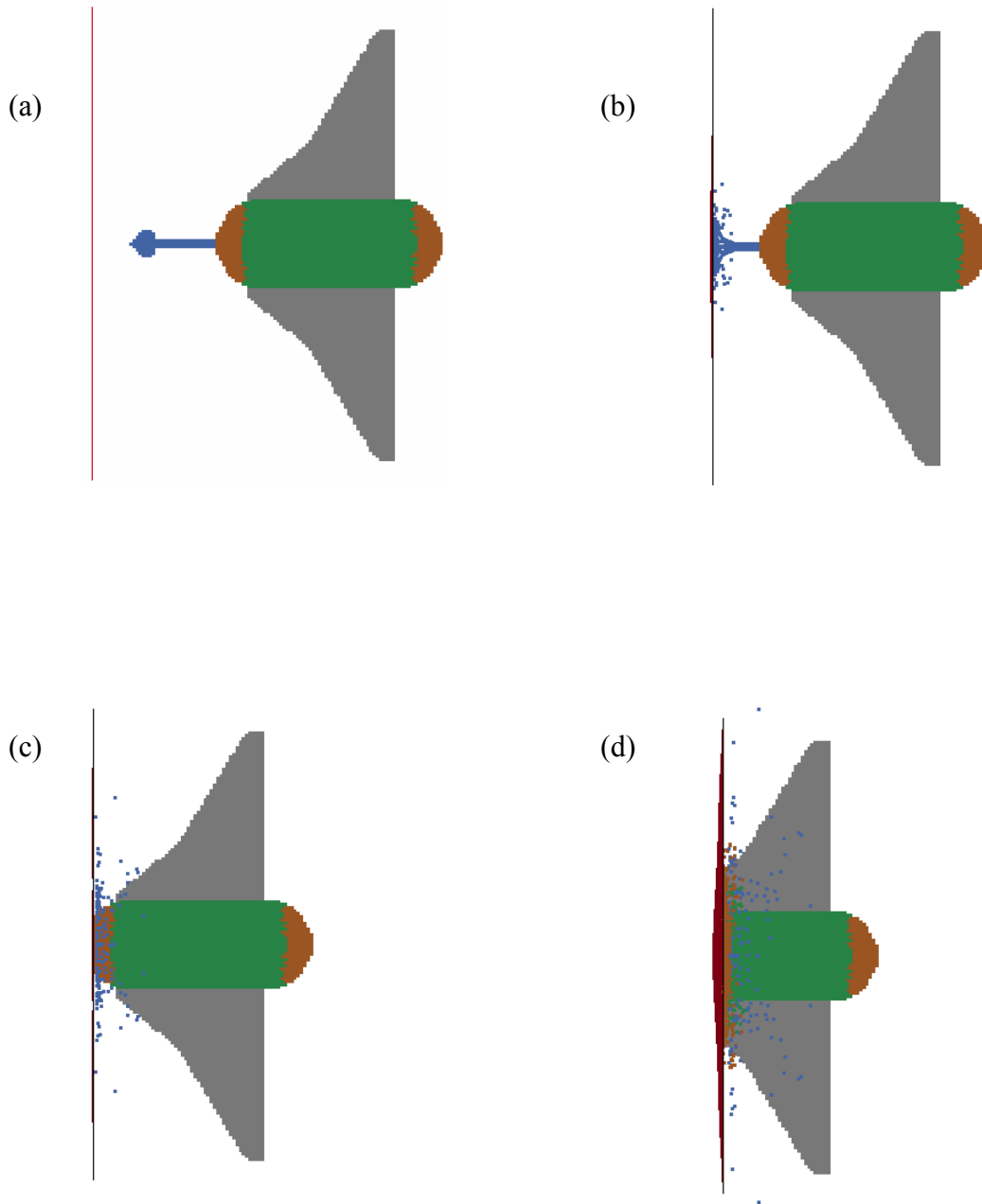


Figure 8.22. Instantaneous particle displacements for a multi-material projectile with $z = 0.0$ for the head and neck, at different times during impact with a flexible flat plate a) 0.0 s, b) 0.00078 s, c) 0.00134 s and d) 0.00199 s.

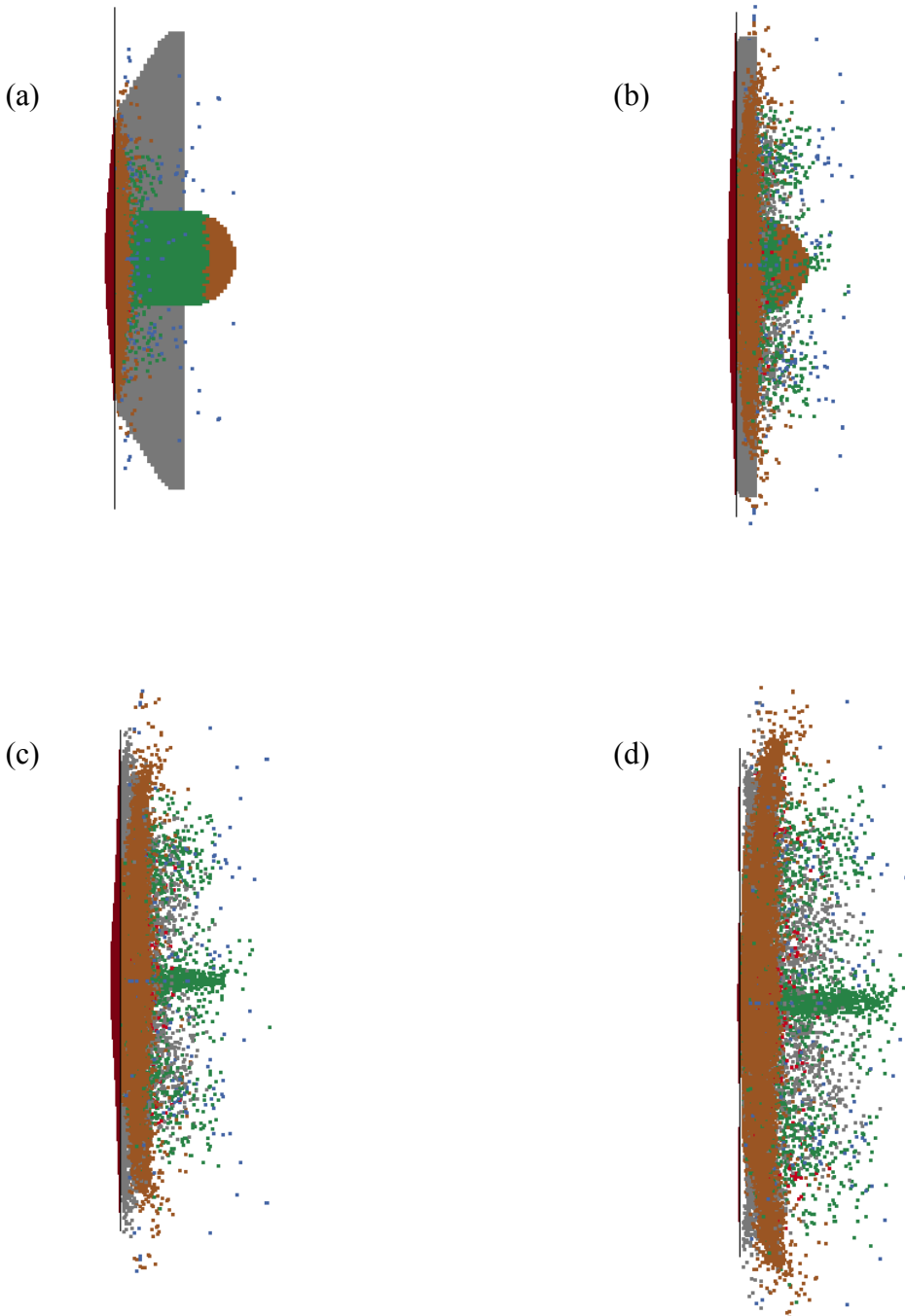


Figure 8.23. Instantaneous particle displacements for a multi-material projectile with $z = 0.0$ for the head and neck, at different times during impact with a flexible flat plate (continued from Figure 8.22) a) 0.0024 s, b) 0.00287 s, c) 0.0032 s and d) 0.00371 s.

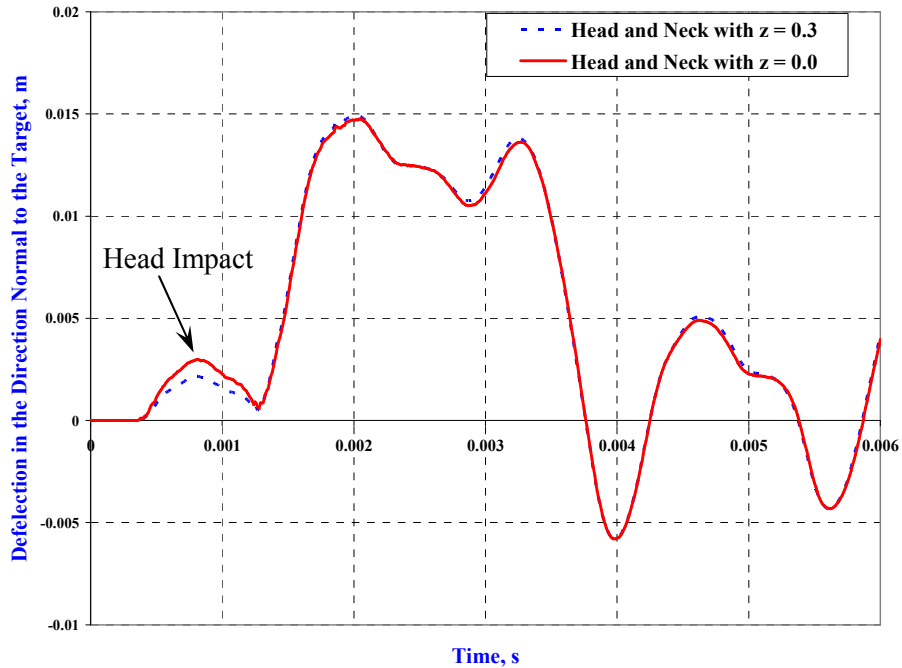


Figure 8.24. Effect of an increase in the density of head and neck material on target deflection for the multi-material bird.

validated by comparing them with the experimental results. Therefore, the target deformations provided by this method are considered to be more accurate.

8.4 Conclusion

Various multi-material projectiles for bird strike analyses were investigated. The multi-material bird strike analyses carried out in this research were more rigorous than any previously published work. Each material in the current multi-material bird model, in addition to having a distinct density, was accompanied by an accurate equation of state. Three different types of multi-material projectiles were investigated:

1. A hemi-spherical bird model with two distinct materials randomly distributed throughout the torso.

2. A hemi-spherical bird model with the traditional homogeneous mixture for the torso, a high density lump to represent the bone structure, and a low density lump to represent the soft tissue and lungs.
3. A realistic bird model that included the characteristic features of real birds such as head, neck, wings, bone structure (ribs), lungs and torso.

Of these three types of multi-material bird models, the model with a realistic bird shape simulated a real bird's impact behavior very well. Clear insights were provided by this bird model on the effect of each part of the bird on the overall impact load spectrum. In addition, the multi-material bird model with realistic shape demonstrated its ability to predict the damage initiated by the head impact on a flexible target.

One of the goals of this work was to find an analytical approach that could eventually reduce or even eliminate the need for elaborate and complex bird strike testing. This led to the analysis of increasingly complex bird models in order to determine the relative importance of the various shape and density parameters. While the current models were successfully calibrated to available bird strike test data, there is a scarcity of experimental data to verify many of the details that have been analyzed, especially the head-on impact of a goose with neck and wings outstretched.

Since a bird impact may occur at any angle and attitude, this work developed a useful, heterogeneous bird model with a realistic shape that provided more impact loading details than primitive, homogeneous bird models. Indeed, the pre-stressing and deflections resulting from the initial impact of a head (or possibly feet and legs of aquatic birds) should be further studied, using various target models and materials. For these studies, the full bird model with component densities presented in this chapter is recommended.

CHAPTER 9

CONCLUSIONS AND SUGGESTIONS FOR FUTURE WORK

A bird strike event, with a duration of only a few milli-seconds, is a very complex interaction between the target structure and the highly nonlinear impact loads generated during the impact event. A strong coupling exists between the impact loads and the target structure deformation. Both the target structure and the projectile undergo severe deformations. Therefore, a rational numerical analysis should include both material and geometric nonlinearities. Since the bird behaves as a “soft body” during impact, an accurate description of its equation of state is essential for predicting correct impact loads.

In this research, the equations of state derived independently for the shock and steady state phases by Wilbeck [8] from one-dimensional analysis were applied to the fully three-dimensional analysis. However, in three-dimensional numerical analysis, an equation of state that describes the entire impact event was necessary. Therefore, this work derived and validated such an equation of state, called the “impact event equation of state,” by combining the shock and steady state equations of state.

The impact event equation of state was used to investigate both homogeneous and heterogeneous bird models. For the homogeneous bird model, the effect of porosity on impact loads was thoroughly investigated. For the heterogeneous bird model, the effects of high density and low density regions within the bird torso were investigated. This was followed by the creation of a simple multi-material bird model having a more realistic bird shape and features, such as a head, neck, bones, and wings. The effect of density variations of the model components on impact loads was investigated. Also, a flexible target was introduced to study the pre-loading effect of the head and neck of a large bird on damage initiation.

9.1 Conclusions

The following conclusions were drawn from the current research work:

1. A variety of simple projectile shapes for the bird torso in bird strike analyses were investigated. Of these simple torso models, the hemi-spherical projectile shape most closely modeled the response of actual birds in experimental tests.
2. Equation of state models that describe the projectile behavior during impact were investigated. The impact event equation of state was proposed and validated by comparing its results in numerical analyses with the results from experimental tests and other numerical analyses.
3. Bird material porosity was found to be a significant factor in predicting precise Hugoniot shock pressures. In particular, porosity values of 0.3 to 0.4 were validated and recommended for a standard bird torso using homogeneous bird models.
4. The current numerical method was found to be capable of predicting correct shock pressures resulting from both a normal impact and an oblique impact.
5. The current analytical procedure was validated for both rigid and flexible target structures.
6. The current numerical method was capable of predicting the deformation of a flexible target as well as target structure failure when the target structure was not strong enough to withstand the impact loads generated during a bird impact event.
7. A variety of multi-material bird analytical models, ranging from simple to more complex shapes were built and studied.

8. The accuracy of a homogeneous bird model was improved by the inclusion of high density lumps to represent the main bone structure and low density lumps to represent the lungs and soft tissue.
9. A multi-material bird model with a more realistic shape provides a more detailed description of the impact load spectrum, and thereby furnishes precise information on the contribution of each part of the bird to the impact load spectrum.
10. Using the current multi-material bird model with a realistic bird shape in numerical bird strike simulations of large birds should be especially useful because there is currently no experimental method for testing a bird in its actual flight attitude.

9.2 Suggestions for Future Work

Most researchers in the field of bird strike analysis refer to experimental tests carried out by Wilbeck [8] to validate their numerical simulations. However, these tests were conducted more than 30 years ago. In spite of the carefully controlled and monitored test conditions of that work, the accuracy and volume of the data was limited by the capabilities of the data acquisition systems available at that time. Current, state-of-the-art, high speed data acquisition technology affords important improvements in the quality of measured test data. Accordingly, a new bird testing program is strongly recommended.

Such a test program should be designed to capture the details of each test condition with modern precision. Details such as the bird orientation, the position of various parts of the bird during the impact event, and impact pressures generated by the impact of each part should be documented in any new testing program.

It is difficult to control the bird orientation as it impacts a target. Nevertheless, if the precise details of the experimental test condition are known, the bird orientation could then be replicated with greater ease in a numerical analysis; so full validation of the numerical method could be achievable. Therefore, an improved and expanded bird strike testing program is an essential step towards the goal of replacing bird strike certification testing with numerical analyses.

At the same time, numerical bird strike analysis methods also require improvements. One such improvement is the ability to use materials with larger differences in density to better represent the various parts of a numerical bird. As mentioned before, current methods do not allow a broad range of densities.

Another required improvement is a reduction in the database sizes. Depending on the fineness of the time step required for accuracy, a database can be several GB in size for an impact event of only 4 milli-seconds. Even though current computer storage capabilities are adequate, the file transfer time for such large databases is quite high, even for the fastest available hardware. Since a full bird strike study can involve the simulation and analysis of hundreds of impact conditions, the work would be greatly accelerated by having smaller output databases.

LIST OF REFERENCES

LIST OF REFERENCES

- [1] Allan, J. R., and Orosz, A. P., "The Costs of Birdstrikes to Commercial Aviation", Bird Strike Committee Proceedings, Bird Strike Committee-USA/Canada, Third Joint Annual Meeting, Calgary, AB, 2001.
- [2] Anghileri, M., Castelletti, L-M L, and Mazza, V., "Bird Strike: Approaches to the Analysis of Impacts with Penetration", Impact Loading of Light Structures, WIT Transactions on Engineering Sciences, Vol 49, 2005. (International Conference on Impact Loading of Lightweight Structures, May 2004.)
- [3] Frischbier, J., Kraus, A., "Multiple Stage Turbofan Bird Ingestion Analysis with ALE and SPH Methods", AIAA Paper No. 2005-1016, 2005.
- [4] Rueda, F., Beltrán, F., Maderuelo, C., and Climent, H., "Birdstrike Analysis of the Wing Slats of EF-2000," Structures under Shock and Impact VII, 2002 WIT Press.
- [5] Wilbeck, J. S., and Rand, J. L. "The Development of Substitute Bird Model", ASME Journal of Engineering for Power, 1981, Vol.103, pp 725-730.
- [6] McCallum, S. C. and Constantinou, C. "The Influence of Bird-Shape in Bird-Strike Analysis", 5th European LS-DYNA Users Conference, Birmingham, UK, May 2005.
- [7] Benson, D., "Computational Methods in Lagrangian and Eulerian Hydrocodes", Computer Methods in Applied Mechanics and Engineering, 1992, No. 99, pp235-394.
- [8] Wilbeck, J. S., "Impact Behavior of Low Strength Projectiles", Ph. D. Dissertation, Texas A&M University, May 1977.
- [9] Teichman, H. C. and Tadros, R. N., "Analytical and Experimental Simulation of Fan Blade Behavior and Damage under Bird Impact", Transactions of ASME Journal of Engineering for Gas Turbine and Power, Vol. 113, October 1991, pp. 582-594.
- [10] Wilbeck, J. S., and Barber, J. P., "Bird Impact Loading," The Shock and Vibration Bulletin, Vol. 48, Part 2, Sept. 1978, pp. 115-122.
- [11] Tudor, A. J., "Bird Ingestion Research at Rolls-Royce," Symposium on the mechanical reliability of Turbo-Machinery Blading, Derby and District College of Technology, Apr. 1968.
- [12] Peterson, R. L., and Barber, J. P., "Bird Impact Forces in Aircraft Windshield Design," Report# AFFDL-TR-75-150, March, 1976.
- [13] Baughn, T. N., and Graham, L. W., "Simulation of Birdstrike Impact on Aircraft Canopy Material," Journal of Aircraft, Vol. 25, No. 7, pp 659-664, July 1988.

- [14] Underwood, G. W., "Aircraft Structural Design Considerations in Relation to Bird Impact Damage," Technical Information Service, AIAA Paper A70-10687.
- [15] Niering, E., 1990, "Simulation of Bird Strikes on Turbine Engines", Journal of Engineering for Gas Turbines and Power, Vol. 112, pp. 573-578.
- [16] Vasko, T. J., "Fan Blade Bird-Strike Analysis and Design", 6 International LS-DYNA Users Conference Simulation 2000.
- [17] Hörmann, M., Stelzmann, U., McCarthy, M. A., and Xiao, J. R., "Horizontal Tailplane Subjected to Impact Loading", 8th International LS-DYNA Users Conference.
- [18] Storange, A. F. Nimmer, R. P., and Ravenhall, R., "Analytical and Experimental Investigation of Bird Impact on Fan and Compressor Blading," AIAA Journal of Aircraft, 1983, Vol.21, No. 7, Paper No 83-0954, pp 520-527.
- [19] Bathe, K. J. and Wilson, E. L., "NONSAP—A Nonlinear Structural Analysis Program," Nuclear Engineering and Design, 1974, Vol.29, pp 266-293.
- [20] Anghileri, M., Castelletti, L-M., Invernizzi, F., and Mascheroni, M., "Birdstrike onto the Composite Intake of a Turbofan Engine," 5th European LS-DYNA Users Conference, May 2005.
- [21] Hallquist, J. O., Release Note for Version 970, Livermore Software Technology Corporation, August 2004.
- [22] Hallquist, J. O., Theoretical Manual, Livermore Software Technology Corporation, March, 2006.
- [23] PAM SYSTEM International, "PAM-CRASH/PAM-SAFE Solver Notes Manual", Version 2000.
- [24] Jain, R., Ramachandra, K., "Bird Impact Analysis of Pre-Stressed Fan Blades Using Explicit Finite Element Code," Proceedings of the International Gas Turbine Congress Tokyo, 2003.
- [25] MSC-DYTRAN, 1992, Users Manual, The MacNeal-Schwendler Corporation, Colorado Boulevard, Los Angeles, CA 90041-1777, USA.
- [26] Anghileri, M., and Bisagni, C., "New Model of Bird Strike against Aircraft Turbofan Inlet," KRASH Conference.
- [27] Boroughs, R. R., "High Speed Bird Impact Analysis of the Learjet 45 Windshield Using Dyna 3D," AIAA Paper No. 1998-1705, 1998.

- [28] Martin, N. F., “A Fluid Soft-Body Projectile Model for Impact Damage Analysis”, Master’s Thesis, University of Delaware, June 1982.
- [29] Martin, N. F., “Nonlinear Finite Element Analysis to Predict Fan-Blade Damage Due to Soft-Body Impact”, *Journal of Propulsion*, Vol. 6, No. 4, pp. 445-450, July-August 1990.
- [30] Belytschko, T., Liu, W. K., and Moran, B., “Nonlinear Finite Elements for Continua and Structure”, John Wiley & Sons Ltd., 2000.
- [31] Brockman, R. A., and Held, T. W., “Explicit Finite Element Method for Transparency Impact Analysis”, University of Dayton Research Institute, Dayton, Ohio, June 1991.
- [32] Zukas, J. A., Nicholas, T., Swift, H. F., Greszczuk, L. B., and Curran, D. R. “Impact Dynamics”, John Wiley & Sons, Inc., 1982.
- [33] Goudreau, G. L. and Hallquist, J. O., “Recent Developments in Large-Scale Finite Element Lagrangian Hydrocode Technology”, *Computer Methods in Applied Mechanics and Engineering*, 1982, Volume 33, pp 725-757.
- [34] Buyuk, M., Can, C-D. S., and Bedewi, N.E., “Moving Beyond the Finite Elements, a Comparison between the Finite Element Methods and Meshless Methods for a Ballistic Impact Simulation”, 8th International LS-DYNA Users Conference, 2004, May 2-4, Dearborn, MI.
- [35] Langrand, B., Bayart, A-S., Chauveau, Y., and Deletombe, E. “Assessment of Multi-Physics FE Methods for Bird Strike Modelling -Application to A Metallic Riveted Airframe”, *International Journal of Crash*, 2002, Vol.7, No. 4, pp 415-428.
- [36] Birnbaum, N.K., Francis, N.J., and Gerber, B.I., “Coupled Techniques for the Simulation of Fluid-Structure and Impact Problems”, *Computer Assisted Mechanics and Engineering Sciences (CAMES)*, 1999, Vol.6, No. 3/4, pp 295-311.
- [37] Donea, J., Huerta, A., Ponthot, J.-Ph., and Rodr´ıguez-Ferran, A., “Arbitrary Lagrangian–Eulerian Methods”, Chapter 14, *Encyclopedia of Computational Mechanics*, Edited by Stein, E., Borst, R., and Hughes, T. J. R., Volume 1: Fundamentals, pp 1-21, John Wiley & Sons, Ltd., 2004.
- [38] Liu, W. K., Belytschko, T., and Chang, H., “An Arbitrary Lagrangian-Eulerian Finite Element Method for Path-Dependent Materials”, *Computer Methods in Applied Mechanics and Engineering*, 1986, Vol.58, pp 227-245.
- [39] Aquelet, N., Souli, M., Gabrys, J., and Olovson, L., “A New ALE Formulation for Sloshing Analysis”, *Structural Engineering and Mechanics*, 2003, Vol. 16, No. 4, pp 423–440.

- [40] Donea, J., Giuliani, S., and Halleux, J. P., “An Arbitrary Lagrangian-Eulerian Finite Element Method for Transient Dynamic Fluid-Structure Interactions”, *Computer Methods in Applied Mechanics and Engineering*, 1982, Vol.33, pp 689-723.
- [41] Benson, D. J., “An Efficient, Accurate, Simple ALE Method for Nonlinear Finite Element Programs”, *Computer Methods in Applied Mechanics and Engineering*, 1989, Vol.72, pp 305-350.
- [42] Monaghan, J. J., “Particle Methods for Hydrodynamics”, *Computer Physics Reports*, October 1985, Vol. 3, Issue 2, pp71-124.
- [43] Monaghan, J. J., “An Introduction to SPH”, *Computer Physics Communications*, 1988, Vol. 48, pp89-96.
- [44] Monaghan, J. J., “Smoothed Particle Hydrodynamics”, *Annual Review of Astronomy and Astrophysics*, 1992, Vol. 30, pp543-574.
- [45] Randles, P. W., and Libersky, L. D., “Smoothed Particle Hydrodynamics: Some Recent Improvements and Applications”, *Computer Methods in Applied Mechanics and Engineering*, 1996, No. 139, pp375-408.
- [46] Lacombe, J. L., “Smooth Particle Hydrodynamics (SPH): A New Feature in LS-DYNA ”, 6th International LS-DYNA Users Conference Simulation 2000, April 9-11, 2000, Dearborn, Michigan, pp7-29-7-33.
- [47] Johnson, A. F, and Holzapfel, M., “Modelling Soft Body Impact on Composite Structures”, *Composite Structures*, 2003, No. 61, pp103-113.
- [48] Johnson, G. R., Stryk, R. A., and Biessel, S. R., “SPH for High Velocity Impact Computations”, *Computer Methods in Applied Mechanics and Engineering*, 1996, No. 139, pp347-373.
- [49] Iannucci, L., “Bird-Strike Impact Modelling”, *Proc. of the Foreign Object Impact and Energy Absorbing Structure*, IMechE 1998, S531/002/98, pp. 11-29.
- [50] Airoidi, A., and Tagliapietra, D., “Bird Impact Simulation against a Hybrid Composite and Metallic Vertical Stabilizer”, 42nd AIAA/ASME/ASCE/AHS/ASC Structures, Structural Dynamics, and Materials Conference and Exhibit, Seattle, WA, 16-19 April 2001, 2001-1390.
- [51] Ubels, L. C., Johnson, A. F., Gallard, J. P., and Sunaric, M., “Design and Testing of a Composite Bird Strike Resistant Leading Edge”, National Aerospace Laboratory, NLR-TP-2003-054.
- [52] McCarthy, M. A., Xiao, J. R., Petrinic, N., Kamoulakos, A., and Melito, V., “Modelling Bird Impacts on an Aircraft Wing - Part1: Material Modelling of the Fibre Metal

- Laminate Leading Edge Material with Continuum Damage Mechanics”, *International Journal of Crash*, 2005, Vol. 10, No. 1, pp 41-49.
- [53] McCarthy, M. A., Xiao, J. R., McCarthy, C. T., Kamoulakos, A., Ramos, J., Gallard, J. P., and Melito, V., “Modelling Bird Impacts on an Aircraft Wing – Part2: Modelling the Impact with an SPH Bird Model”, *International Journal of Crash*, 2005, Vol. 10, No. 1, pp 51-59.
- [54] McCarthy, M. A., Xiao, J. R., Petrinic, N., Kamoulakos, A., and Melito, V., “Modelling of Bird Strike on an Aircraft Wing Leading Edge made from Fibre Metal Laminates - Part1: Material Modelling”, *Applied Composite Materials*, 2004, No. 11, pp 295-315.
- [55] McCarthy, M. A., Xiao, J. R., McCarthy, C. T., Kamoulakos, A., Ramos, J., Gallard, J. P., and Melito, V., “Modelling of Bird Strike on an Aircraft Wing Leading Edge made from Fibre Metal Laminates – Part2: Modelling of Impact with SPH Bird Model”, *Applied Composite Materials*, 2004, No. 11, pp 317-340.
- [56] Goyal, V. K., Huertas, C. A., Borrero, J. R., and Leutwiler, T. R., “Robust Bird-Strike Modeling Based on ALE Formulation Using LS-DYNA ”, 47th AIAA/ASME/ASCE/AHS/ASC Structures, Structural Dynamics, and Materials Conference, 1 - 4 May 2006, Newport, Rhode Island, AIAA 2006-1759.
- [57] Goyal, V. K., Huertas, C. A., Leutwiler, T. R., and Borrero, J. R., “Robust Bird-Strike Modeling Based on SPH Formulation Using LS-DYNA ”, 47th AIAA/ASME/ASCE/AHS/ASC Structures, Structural Dynamics, and Materials Conference, 1 - 4 May 2006, Newport, Rhode Island, AIAA 2006-1878.
- [58] Furtado, R. D., “Finite Element Analysis of Bird Strike on Aircraft Structures”, Master’s Thesis, Spring 2000, Wichita State University.
- [59] Huertas, C. A., “Robust Bird-Strike Modeling Using LS-DYNA,” Master’s Thesis, 2006, University of Puerto Rico.
- [60] VonNeumann, J., and Richtmyer, R. D., “A Method for the Numerical Calculation of Hydrodynamic Shocks”, *Journal of Applied Physics*, March 1950, Volume 21, Issue 3, pp. 232-237.
- [61] Belytschko, T., “An Overview of Semi-discretization and Time Integration Procedures”, *Computational Methods for Transient Analysis*, edited by Belytschko, T., and Hughes, T. J. R., 1983, Elsevier Science Publishers, No.1, pp. 1-65.
- [62] Bathe, K-J., “Finite Element Procedures,” Prentice Hall, 1996.
- [63] Zukas, J. A., “Introduction to Hydrocodes”, Elsevier, 2004.

- [64] Barber, J. P., Taylor, H. R., and Wilbeck, J. S., "Bird Impact Forces and Pressures on Rigid and Compliant Targets," Report# AFFDL-TR-77-60, University of Dayton Research Institute, Air Force Flight dynamics Laboratory, May 1978.
- [65] Deal, W. E., "Shock Hugoniot of Air," Journal of Applied Physics, Vol. 28, Issue. 7, July 1957, p.782-784.
- [66] Moffat, T. J. and Cleghorn, W. L., "Prediction of Bird Impact Pressures and Damage Using MSC/DYTRAN", Proc. of ASME TURBOEXPO, June 4-7, 2001.